ABSTRACT

SONG, XIAO. Investigating the Role and Structure of Free Radicals in Lignin Biosynthesis. (Under the direction of Prof. Tatyana Smirnova).

Lignin is the second most abundant biopolymer on earth after cellulose that contributes to the overall viability and sustainability of the plant kingdom. Understanding molecular details of the lignin formation and cross-linking is of fundamental importance to production of biomass streams. Although the processes of monolignols oxidative dehydrogenation, polymerization and cross-linking to cell walls are proposed to occur through a free radical mechanism, the specific details remain elusive.

In order to understand molecular mechanisms of these reactions, we investigated formation of radicals during enzyme-catalyzed (HRP or Laccase) oxidative dehydrogenation of twelve monolignols. To characterize short-lived radicals formed during the enzymatic reaction we employed EPR spectroscopy in combination with spin-trapping technique and deduced the structures and spatial conformations of radicals. We also utilized continuous-flow EPR in combination with enzyme surface immobilization to detect the formation of transient monolignol radicals and thus patterned their isotropic hyperfine parameters that allow for the mapping of unpaired electron distribution. Polymerized radicals formed as a result of the coupling of enzyme-generated monolignol radicals. The effective g-factors and ΔH_{P-P} of EPR spectra of polymerized radicals could be used as a reference to identify the polymeric radicals obtained from monolignols by different methods and paramagnetic species in natural lignin.

We further generated a monolignol radical using consecutive enzymatic deglucosidation and oxidative dehydrogenation of a monolignol glucoside. This approach

could be used to probe the isotropic hyperfine interactions of radical structures of monolignols with limited solubility in water by continuous-flow EPR method, especially for monolignol hydroxycinnamate conjugate compounds whose isotropic hyperfine component have not been studied yet.

Furthermore, we investigated the anisotropic hyperfine tensors of photogenerated monolignol radicals by 2D HYSCORE spectroscopy at 77K. Four unique unpaired electron spin-proton interactions were characterized, in which the protons identified having large isotropic hyperfine and small anisotropic hyperfine correspond to β-methylene protons of π-radical. The formation of methylene group is highly likely to occur at Cα as a result of reduction of double bond at side chain upon illumination. Secondary reactions could occur during UV illumination of monolignols and result in radical species structurally different from monolignol radicals enzymatically generated. HYSCORE was demonstrated to be able to provide information on hyperfine tensors of the radicals embedded in lignin matrix either upon lignin formation or as a result of lignin decomposition. HYSCORE investigation of model monolignols-based radicals can provide a set of "fingerprints" from particular radicals to be used to analyze and identify lignin-based radical centers.

Investigating the Role and Structure of Free Radicals in Lignin Biosynthesis

by
Xiao Song

A dissertation submitted to the Graduate Faculty of
North Carolina State University
in partial fulfillment of the
requirements for the degree of
Doctor of Philosophy

Chemistry

Raleigh, North Carolina

2016

APPROVED BY:

_____	_____
Dr. Tatyana Smirnova Committee Chair	Dr. Reza Ghiladi
_____	_____
Dr. Walter Weare	Dr. Gufeng Wang

DEDICATION

To my family

BIOGRAPHY

Xiao Song was born on July 19th, 1987 in the mountain city in Southwest China, Chongqing. She is the only child of parents Ming Song and Jin Cheng. Her mother tried to foster her interest in arts so she attended piano, dance, calligraphy and drawing courses, but none of them she found herself was good at. With no talent in arts, she changed her direction to Science and left home for college study in Chemistry in Shenyang, a big city in Northeast China, and spent her four-year undergraduate and two-year graduate life in there. Influenced and encouraged by her uncle who excellently finished his Ph.D. in Chemistry in the U.S. and now a department head of a leading global paints and coatings company, she made up her mind to come to the U.S. to pursue a higher degree in Chemistry. In August 2011, she was accepted to Graduate School of North Carolina State University in Raleigh and Joined Prof. Smirnova's research group where she studied magnetic resonance techniques such as EPR and NMR. Her research was focused on understanding the role and structure of free radicals in lignin biosynthesis.

ACKNOWLEDGMENTS

The following people are acknowledged for their contribution:

Prof. Tatyana Smirnova, Advisor

Prof. Reza Ghiladi, Prof. Walter Weare, Prof. Gufeng Wang, Prof. Keith Weninger

for being a part of the advisory committee

Prof. Maxim Voynov for the many discussions and help during research

Dr. Sergey Milikisiyants for the assistance in HYSCORE experiment

Family- Parents, husband and uncle

Friends- for support and strength

Everyone in Smirnova/Smirnov group

TABLE OF CONTENTS

LIST OF TABLES

LIST OF FIGURES

CHAPTER 1

A General Introduction to Lignin, Lignin Biosynthesis and Magnetic Resonance Spectroscopy

1.1 Importance of lignin in cell wall and for human utilization of biomass

Lignin is the second most abundant biological material on the planet, exceeded only by cellulose and hemicellulose, accounting for approximately 30% of organic carbon in the biosphere[1]. As an integral part of the secondary cell wall, lignin is water insoluble and stable, it is covalently linked to hemicellulose and cross-linked to other cell wall components (i.e. proteins and cellulose) and provides several important functions to cell wall of plants. Lignin plays an important role in cell's endurance and development including preserving the structural integrity and strengthening the rigidity of cell wall and modulating the compression resistance to impact, compression and bending[2]. The cross-linking between lignin and hydrophilic polysaccharides is essential for efficient transportation of water, nutrition and metabolites within the cell wall. Lignin also serves in protecting plants against the invasion of pests, pathogen and other environmental stresses. As a natural and renewable material, obtainable at an affordable cost, and great physical and chemical properties, the interest in lignin is renewed for use in many high value-added product including chemicals, carbon fiber and biopolymer engineering materials[3]. Lignin acts as the "glue" that connects cellulose and hemi-cellulose (Figure 1.1), which on the other hand hinders the degradation of cell wall polysaccharides into simple sugars[4]. Therefore, a better characterization of lignin

heterogeneous chemical composition with specific attention to reactive and free radical species would benefit the removal and de-polymerization of lignin for new and efficient energy.

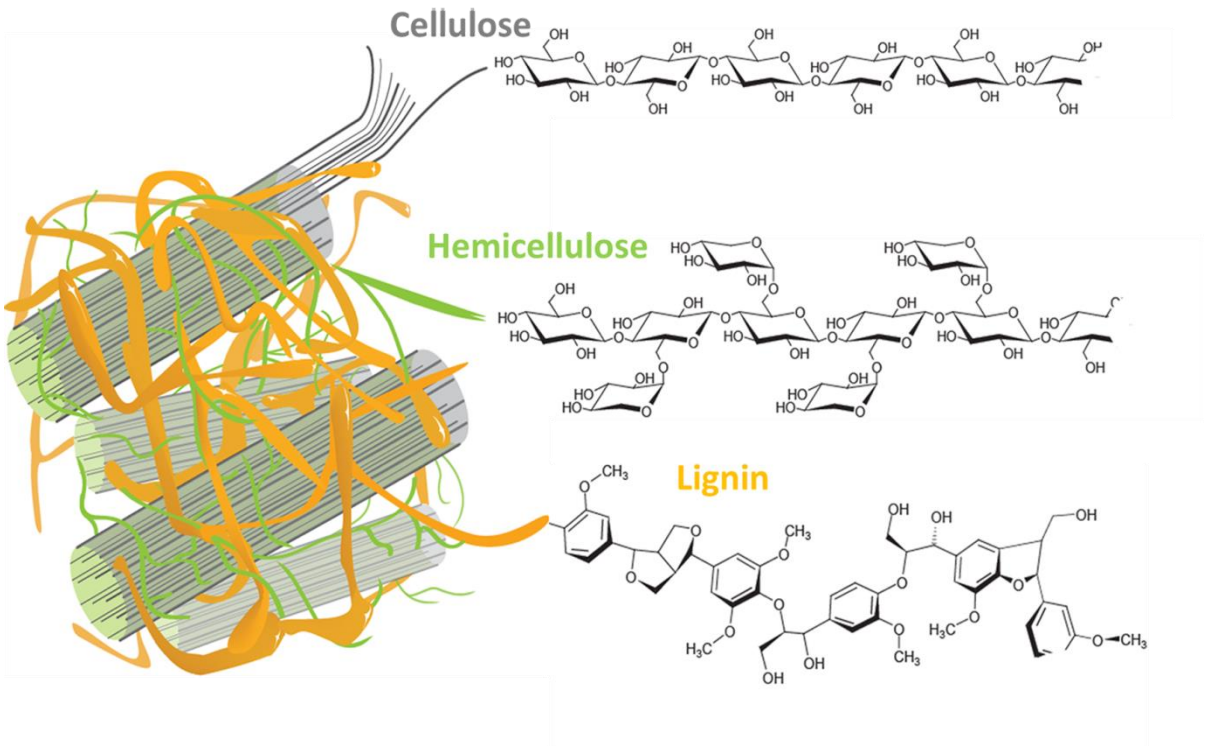

Figure 2.1: *Composition of the plant cell wall*[5].

1.2 Lignin biosynthesis

Varies in the stages of cell-tissue-specific development, the lignification generally initiates during the formation of the secondary cell wall, which is considered to occur in three main stages: 1) biosynthesis of monolignols in the cytosol, 2) transport of monolignols to the cell wall, and 3) oxidative dehydrogenation and polymerization of monolignols to form heterogeneous macromolecules[6]. The biosynthesis of monolignols is initiated in the general phenylpropanoid pathway[7] starting with phenylalanine. The successive hydroxylation reaction of aromatic ring and followed phenolic–*O*–methoxylation and conversion of side

chain carboxyl catalyzed by a series of enzymes (phenylalanine ammonia lyase (PAL), cinnamate 4-hydroxylase (C4H), etc.) complete the production of monolignols. As monolignols are synthesized, they are transported to cell wall for subsequent oxidation and polymerization. Although much less is known regarding the transportation, translocation across cell membrane and deposition of monolignols compared to the progress in elucidating monolignols biosynthesis pathways and molecular regulation of the biosynthetic process, several hypotheses were suggested[6a, 7] including exocytosis, passive diffusion and active transport through ATP-binding cassette (ABC). It also has been demonstrated that monolignols connecting with 4-*O*-β-D-glucoside can be transported to cell wall or to vacuole in an ATP-dependent process by specific ABC transporter[8]. In case for the use under pathogen or other attack, monolignols are released from glucosides by hydrolysis of the glucosidic bonds by the function of *β*-glucosidase and subsequently incorporated into lignin. Monolignols are also converted into lignan in cytosol through the coupling of 8 and 8' C-atoms of two monolignols, and after further glycosylation, lignan glucosides are used as the storage or transport form of monolignols as a defense mechanism against insect predators[9]. After transport and deposition of monolignols to the cell wall, lignin formation begins and proceeds through oxidative dehydrogenation and polymerization from monolignols. During this process, monolignols undergo enzyme (peroxidases, laccases, polyphenol oxidases, etc.) catalyzed oxidation or dehydrogenation into monolignol radicals which are then form various linkages either between radicals, to existing lignin units or to cell walls (Figure 1.2).

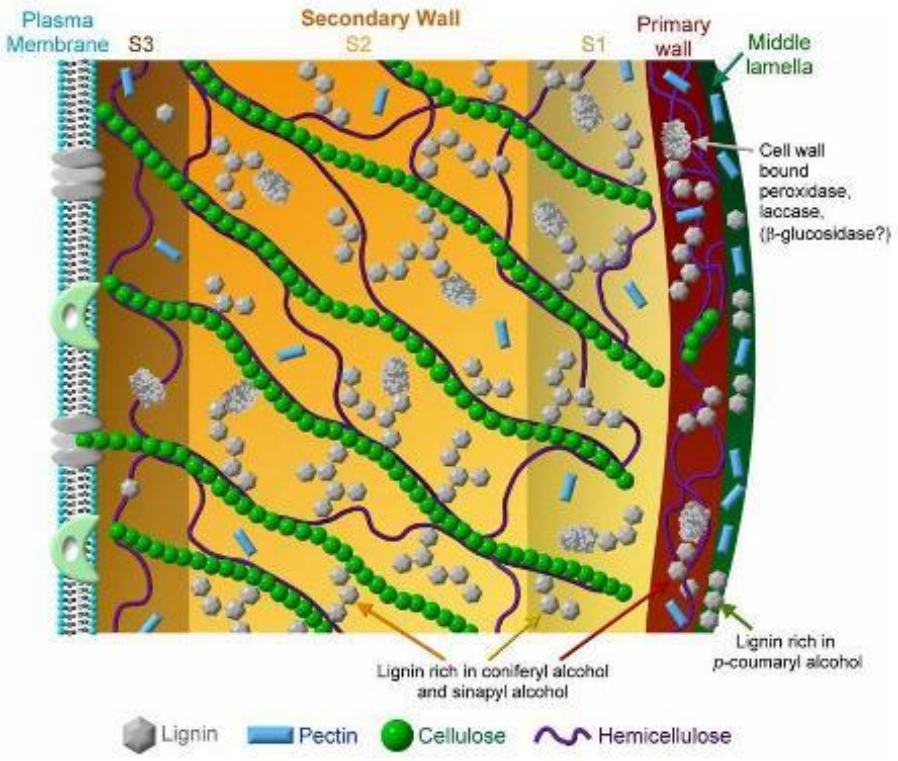

Figure 1.2: *The relative contributions of the three major monolignols to the lignin in the various layers and the cell wall-bound enzymes might participate in the various steps of lignification*[10].

1.3 Components of lignin

Lignin is defined as an amorphous, polymeric material arising from dehydrogenative polymerization of three phenylpropanoid monomers so called monolignols, *p*-coumaryl, coniferyl and sinapyl alcohols, differing in the degree of methoxylation. When integrated into lignin matrix, three monolignols produce *p*-hydroxyphenyl (H), guaiacyl (G) and suringyl (S) phenylpropanoid units, respectively (Figure 1.3). Lignin composition varies for different plants, tissues and developing period. In typical softwood the structural elements of lignin are derived principally from coniferyl alcohol, while typical hardwood lignin is comprised of coniferyl alcohol and sinapyl alcohol-derived units in varying ratios. Grass

lignin, is mainly formed by coniferyl and sinayl alcohol units, but also contains more significant amount of *p*-coumaryl alcohol[11]. Other functional groups, such as methoxyl and carbonyl groups, can be attached to the basic phenylpropanoid skeleton and have a great impact on the structure and properties of lignin. Besides three classical monolignols, the products from incomplete monolignol biosynthesis, such as hydroxycinnamic acids[6a], hydroxycinnamaldehydes[12], as well as the enzymatic derivatives of monolignols, such as coniferyl and sinapyl *p*-coumarates[13], and coniferyl and sinapyl acetates[14], are all lignin precursor candidates that need for study. Since the formation of a three-dimensional polymer of lignin lacks the regular and ordered repeating units found in other natural polymers such as cellulose and proteins, lignin is viewed as a physically and chemically heterogeneous material whose structure is represented by a composition of a large variety of phenylpropanoid monomers.

The presence of both ether- and ester-linked hydroxycinnamic acids in cell walls of wheat straw and rice have been reported in 1986[15]. Iiyama et al suggested that ether-linked hydroxycinnamic acid, especially ferulic acid, forms the bridges between lignin and polysaccharides in cell walls of wheat internodes[16]. Ferulic acid is proposed to esterify to polysaccharides during the formation of primary cell wall, the resultant ferulate is linked to the benzyl position of a lignin side chain through a nucleophilic addition reaction to quinonemethide intermediates of lignin during lignification[17].

Hydroxycinnamates, from hydroxylation of hydroxycinnamic acids, are found not only participate in lignin formation but also cross-link lignin with polysaccharides, as esters, to alter the structural integrity of the cell wall[18]. For example, ferulate in grass appears to function as nucleation site for lignin polymerization and a cross-linking agent in both

primary and secondary wall tissues[18c, 19]. Its dehydrogenation polymers (DHPs) are found to present the same kind of chemical combinatorial radical coupling as occur in lignin formed by solely classical monolignols[18c].

Acetylation has been reported to occur in the lignin of a limited number of hard woods and nonwoody plants[20], in particular in Kenaf bast fiber lignin was found to have over 50% lignin acetylation almost from sidechains' primary aliphatic alcohol. Fachuang et al suggested a mechanism to determine the occurrence of acetylation prior to the polymerization steps of lignification [14]. For convenience, all types of phenylpropanoid compounds used in this work are called as "monolignols".

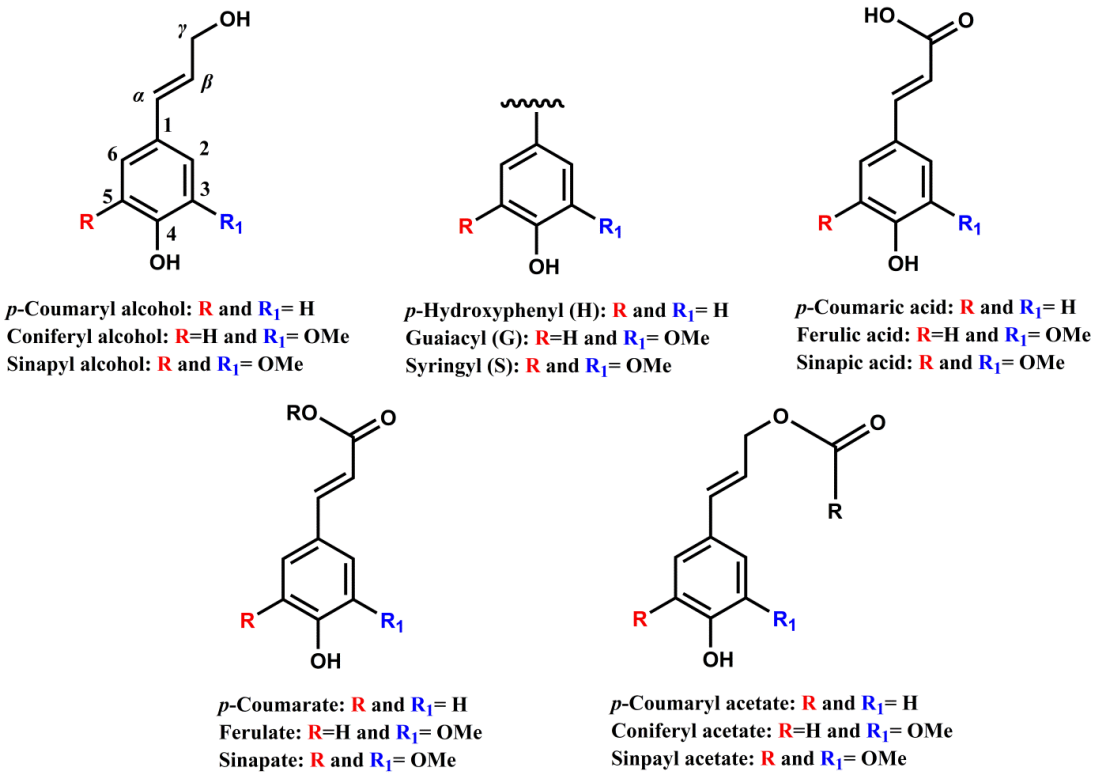

p-Coumaryl alcohol: R and R_1= H
Coniferyl alcohol: R=H and R_1= OMe
Sinapyl alcohol: R and R_1= OMe

p-Hydroxyphenyl (H): R and R_1= H
Guaiacyl (G): R=H and R_1= OMe
Syringyl (S): R and R_1= OMe

p-Coumaric acid: R and R_1= H
Ferulic acid: R=H and R_1= OMe
Sinapic acid: R and R_1= OMe

p-Coumarate: R and R_1= H
Ferulate: R=H and R_1= OMe
Sinapate: R and R_1= OMe

p-Coumaryl acetate: R and R_1= H
Coniferyl acetate: R=H and R_1= OMe
Sinpayl acetate: R and R_1= OMe

Figure 1.3: *The chemical structures of three classical monolignols (Top left). The three building blocks of lignin (Top middle). The chemical structures of three hydroxycinnamic acids (Top right). The chemical structures of three hydroxycinnamates (bottom left). The chemical structures of three hydroxycinnamyl acetates (bottom right).*

1.4 Enzyme-catalyzed oxidative dehydrogenation of monolignols

The monolignols are known to be oxidative-dehydrogenated through one-electron oxidation by different classes of proteins, such as peroxidase and laccase (Figure 1.4). The details of oxidation by these two enzymes are given in here.

As the most widely studied of all peroxidases, Horseradish Peroxidase (HRP) is found to be able to catalyze the oxidation of a wide variety of organic molecules such as phenols and aromatic amines using hydrogen peroxide (H_2O_2) as electron acceptor[21]. The oxidation by HRP/H_2O_2 system involves a three-step redox cycle, in which HRP is oxidized by H_2O_2 and then reduced back to its native state involving the formation of two intermediates, Compound I and Compound II. The active catalytic site of HRP is heme. The heme prosthetic group ferriprotoporphyrin IX consists of Fe (III) ion chelated by a porphyrin. It can directly react with H_2O_2 through a two-electron oxidation to give an active green species known as Compound I containing one oxyferryl (Fe(IV)=O) center and one π-cation radical on porphyrin ring. Compound I abstracts one proton and one electron from the oxidation of a monolignol, the electron reduces the π-cation radical on porphyrin ring and the proton is accepted by the imidazole side chain of distal His42. As a result, the monolignol molecule is oxidized into a free radical and Compound I is reduced to Compound II. Compound II still possesses one oxidizing equivalent compared to its native state and it acquires one proton and one electron from the second monolignol molecule so the native state of HRP is regenerated and the second monolignol radical is formed[22].

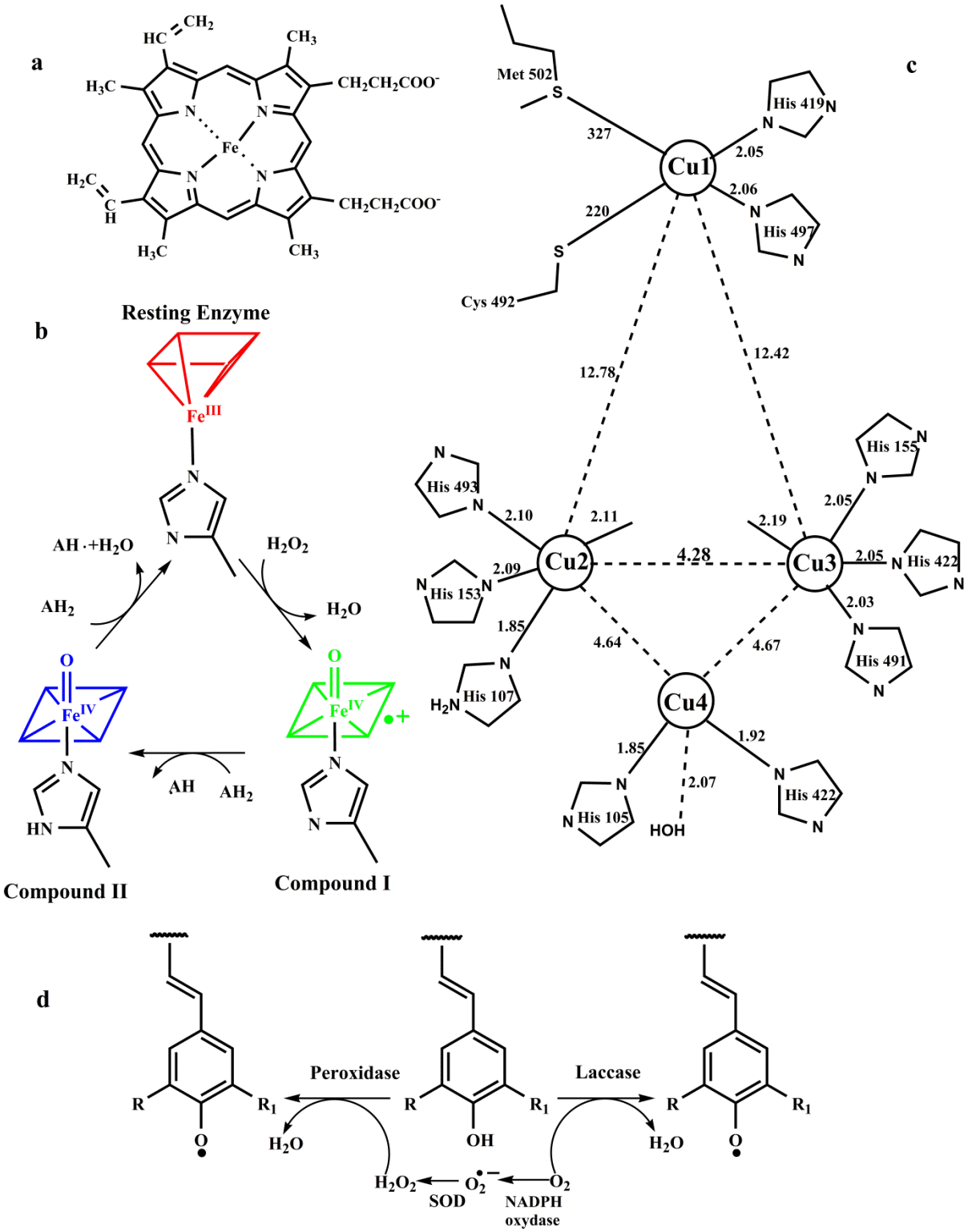

Figure 1.4: *a) Structure of iron heme group in Horseradish Peroxidase[23]; b) Catalytic cycle of heme peroxidase[22a]; c) Structure of multi-copper cluster in laccase[24]; d) Monolignol oxidative dehydrogenation by HRP or laccase.*

In contrast with HRP, laccase is a blue copper oxidase. It catalyzes the oxidation of four monolignol molecules with the four-electron reduction of oxygen to water. Four copper atoms exhibited in laccase play an important role in laccase catalytic mechanisms[25]. The four coppers are classified into Type 1 (Cu1), Type 2 (Cu4) and Type 3 (Cu2 and Cu3) in Fig. 1.4c, in which Type 2 and 3 centers are combined to function as a tri-nuclear copper cluster with respect to the reaction with oxygen. The two-electron reduction of oxygen appears to occur from Type 2/3 bridging mode to generate peroxide-level intermediate. Later the peroxide-level intermediate facilitates the second two-electron reduction from the Type 1 and 2 centers in that the peroxide is directly coordinated to reduced Type 2 copper, and the reduced Type 1 is coupled to the Type 3 by the covalent Cys–His linkages[26].

1.5 Lignin structure extension

Dehydrogenation of the hydroxyl group of monolignol molecule yields a radical species with the unpaired electron delocalized over benzene ring and side-chain in conjugate structures (Figure 1.5). Instead of the growth of polymer chain through the combination of two oligomer molecules, the elongation of the molecule will predominantly take place through so called "endwise" polymerization[6a]. In fact, radical coupling reaction results in radical quenching, thus, a new coupling site is required for each step of structure elongation. However, the oxidative dehydrogenation of oligomer molecule seems not to be controlled by enzyme: first, bulky enzyme is difficult to diffuse freely within the structure of oligomer; second, unlike cellulose and other biomolecules produced in the active site of an enzyme and having very defined structures, lignin presents many different types of bonds connecting the monomer residues in a random pattern. One of the accepted ideas about radical transport in

the network of oligomer is via the diffusion of some relative small species, such as monolignol radical itself[27], superoxide radical or Mn(II)/Mn(III) oxalate[28]. Some common types of linkages such as *β*-O-4, *β*-5, *β*-*β*, 5-5, *α*-O-4 and 4-O-5 (the latter two only occur between oligomers) and minor *β*-1 have been found from spruce lignin degradation study(Figure 1.5)[29], in which *β*-O-4 coupling results in a quinonemethide that will react further by addition of a molecule of water to give a glycerol-*β*-aryl ether structure, or react with a monolignol molecule having phenolic hydroxyl group through additive, nondehydrogenative mode to give a glycerol-*α, β*-diaryl ether unit[30]. The DPHs study[31] proves that the coupling of radicals by *β*-O-4 and *β*-5 would lead to a linear polymer while biphenyl 5-5 coupling and diary ether 4-O-5 coupling may give rise to molecule branching preferentially occurred between two end-group radicals[30].

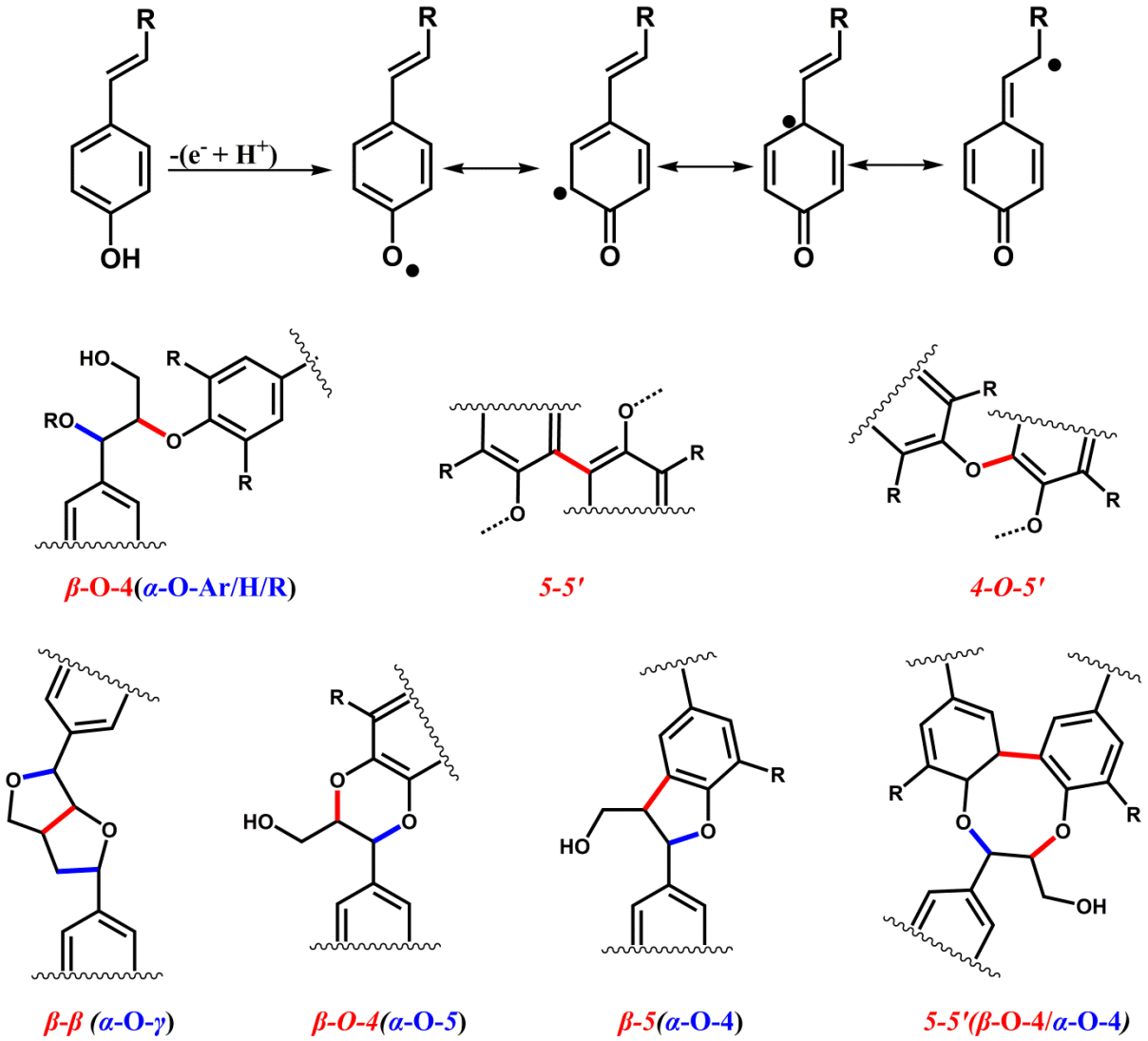

Figure 1.5:*.Delocalization of unpaired electron over the molecule of phenoxy radical (top). The main structural units in lignins (bottom) including C-C or C-O bond formed in the oxidative coupling of two phenoxy radicals (red) and the post-coupling bonds (blue).*

1.6 EPR studies on lignin

Relative to the identification and characterization of products derived from monolignol segments through these radical reactions, the direct examination of how polymerization processes take place in vivo has demonstrated less progress and the actual process for formation of lignin remains elusive.

A number of spectroscopic methods was utilized to elucidate polymerization process[11, 32]. Spectroscopic studies of lignin polymerization were generally limited to model systems. Based on the current theory that lignin polymerization occurs by combinatorial-like coupling reactions between phenolic compounds through radical mechanism, efforts were put forward to elucidate the structure of the intermediate radicals.

It has been assumed by Steelink et al[33] that the radical species are semiquinone radicals stabilized in the polyphenolic lignin matrix. However, experimental characterization of such radical species using X-band CW EPR is strongly limited as the inhomogeneously broadened single line only yielding the principle g-value[34]. From the unresolved nature of lignin EPR spectrum the detailed structure information of the lignin based radical cannot be extracted. Recently, the anisotropy of g-tensor ($g\ anisotropy = \frac{g_{xx}-g_{yy}}{g_{zz}}$) was resolved using a high-field EPR, and with the assistance of DFT calculation the substituted *o*-semiquinone radical species in different protonation states were identified[35]. However, the calculated g_{xx} was overestimated because DFT calculation was performed on a single molecule in gas phase with artificial modified dielectric constant, but the bimolecular matrix interactions, in particular dipolar hyperfine couplings with neighboring protons were not

considered. To map the proton hyperfine interactions, we conducted CW EPR and pulsed EPR study on radical species of lignin precursors.

The CW X-band EPR has been employed to demonstrate the possibility of generation of free radical species from 4-hydroxycinnamic acids and 4-hydroxycinnamyl alcohols and to study the effect of hydroxylation and methoxylation on the ease of oxidation[36]. The free radicals studied were generated under non-biologically relevant conditions – using highly acidic (pH=0.5-1.5) solution of ammonium cerium (IV) nitrate containing 50 v/v% of ethanol. The generation of radical species from 4-hydroxycinnamic acids, 4-hydroxycinnamyl alcohols, 4-hydroxycinnamates, 4-hydroxy-3-methoxycinnamaldehydes and various dimeric substrates by HRP/H_2O_2 oxidation at 77k was also reported, the unresolved peak that appeared in the presence of monolignol did not provide any useful information with aspect to the proton hyperfine interactions[37]. The formation of other phenoxy radicals by oxidation with horseradish peroxidase were observed[32d, 38].

1.7 Theory of EPR Spectroscopy

Since we used EPR spectroscopy through-out the entire work, a fundamental of EPR theory is necessary to be described. EPR spectroscopy is amenable for studying the paramagnetic ions or molecules containing at least one unpaired electron. For free organic radicals, its electronic spin has spin quantum number *s*=1/2 so its corresponding magnetic quantum number are m_s= +1/2 and m_s= -1/2. In the absence of an external magnetic field, the states with different values of m_s are degenerate, when the external magnetic field B_0 is present, splitting of two states occurs due to Zeeman Effect,

$$E_{ms} = -g\gamma_e m_s \hbar B_0 = g\mu_B m_s B_0 \quad (1.1)$$

where γ_e is magnetogyric ratio of electron, $\hbar$ is modified Planck's constant, g is electronic g-factor and μ_B is Bohr magneton. The g-factor is dependent upon the paramagnetic species and is characteristic of electronic structure. For the free electron, g_e is equal to 2.002319.

In the external magnetic field, the state with m_s =+1/2 moves up in energy by 1/2$g_e\mu_B B_0$ while the state with m_s=-1/2 moves down in energy by -1/2$g_e\mu_B B_0$. Therefore the energy gap between these two states of electron spin in a magnetic field B_0 is,

$$\Delta E = g\mu_B B_0 \quad (1.2)$$

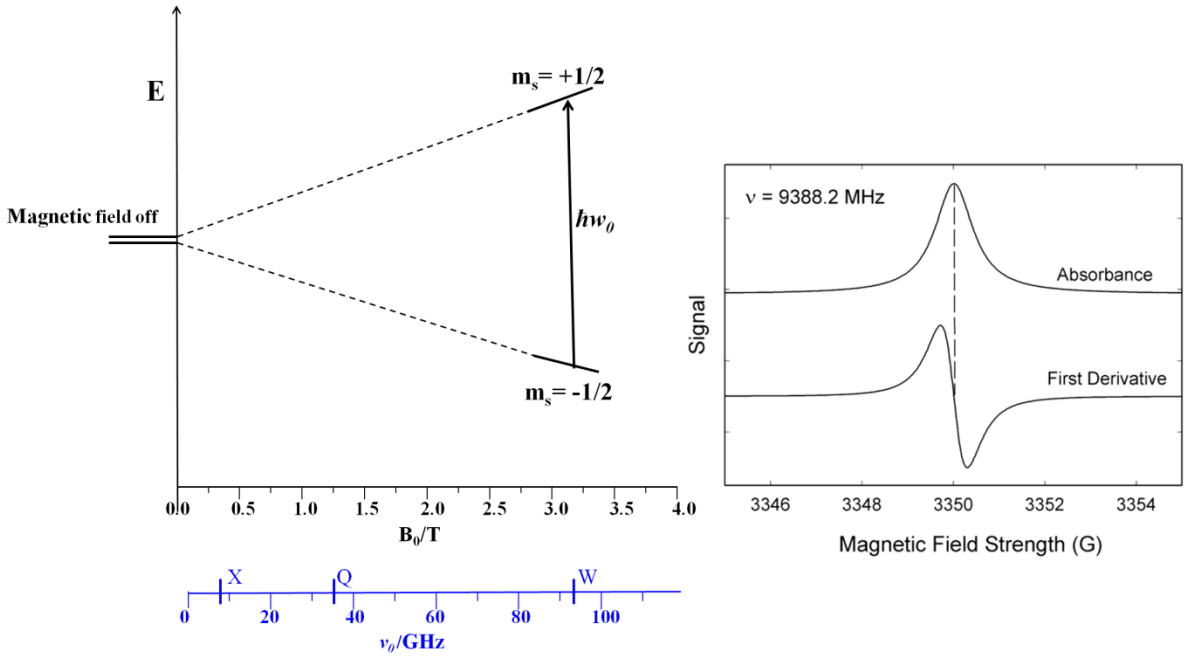

Figure 1.6: *The energy diagram of an unpaired electron in an external magnetic field (top left), first derivative of an absorption (right) and various frequency regions used in EPR spectrometer (bottom).*

The magnetic moment of the electron can transfer from a state with a lower energy level to a state with a higher energy level by absorbing monochromatic radiation if the resonance condition is satisfied (Figure 1.6):

$$h\nu = g\mu_B B_0 \tag{1.3}$$

To produce a microwave source that provide a variable frequency range with a sufficient amplitude and frequency stability is extremely difficult, most facile EPR experiment is realized by continuous microwave irradiation of a sample placed in a varied magnetic field. The first derivative of the absorption is recorded as EPR spectra (Figure 1.6). Magnetic field of about 0.3T with corresponding electromagnetic field of frequency ca. 10 GHz (X-band at g≈2) is used in most commercial EPR spectrometers (Figure 1.6). For organic radicals, the deviation of g-factor from g_e is very small and mainly attributed to spin-orbital coupling (interaction of the spin with orbital angular momentum of the unpaired electron).

When interacting with the nearby nuclei possessing an intrinsic spin angular momentum, the unpaired electron spins experience a local field from magnetic nuclei, which results in small changes in their allowed energy levels depending on the nuclear spin state. It is referred to as the hyperfine interaction. The resonance condition in such case is described by:

$$h\nu = g\mu_B(B_0 + B_{local}) \tag{1.4}$$

where B_{local} is magnetic field generated by nuclear spin at the location of the unpaired electron.

The perturbation to the electronic energy from hyperfine interaction can be described by the modified spin Hamiltonian,

$$\hat{\mathrm{H}} = g\mu_B \hat{\mathrm{S}} \cdot B_0 + A\hat{\mathrm{I}} \cdot \hat{\mathrm{S}} \qquad (1.5)$$

where A is the hyperfine splitting constant, $\hat{I}$is nuclear spin operator.

There are two main ways in which hyperfine interaction occurs, one is anisotropic part by direct dipole-dipole forces between the magnetic moments of the unpaired electron and nuclei, the other is isotropic part by Fermi contact interaction depending on the density of unpaired electron spin at the magnetic nuclei. The anisotropic hyperfine interaction depends on sample orientation to the magnetic field and the distance between the electron and nuclei as well as the orbital shape. It is averaged out to zero if the molecule is rotating rapidly, such as in liquid. The Fermi contact interaction, unaffected by sample orientation to the magnetic field, is related to the magnitude of an electron density directly at the nucleus. .

In Figure 1.7, m_s= +1/2 and m_s= -1/2 states are simply notated as symbols α and β, respectively. Depending on the magnetic quantum number of nuclear spin, the local field generated by nuclei adds to or subtracts from the external magnetic field. Thus, instead of a single line, the CW EPR spectrum of a radical in fast motion is split into 2I+1 hyperfine lines with a binomial intensity distribution. The splitting of the resonance lines is also an important feature of the EPR spectrum.

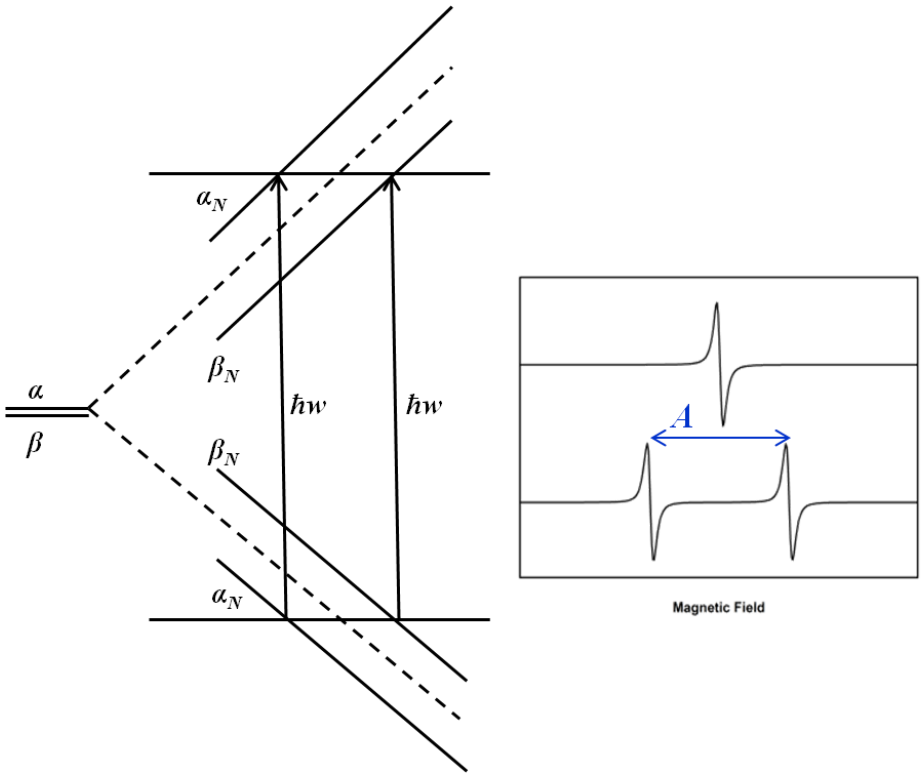

Figure 1.7: *The hyperfine interaction resulting in four energy levels and the corresponding two EPR transitions ($\Delta m_s = 1$) in $S = \frac{1}{2}, I = \frac{1}{2}$ system.*

Another important feature of EPR spectrum is peak-to-peak line width (ΔH_{P-P}), the distance between maximum and minimum of a derivative signal. ΔH_{P-P} is comprised of two kinds of contributions. One is related to the spin-lattice relaxtion which results from the interations between an electorn in upper enenrgy level and its surroundings. The fast relaxation process would cause a broadening of spectral lines. The second contribution is known as inhomogeneous broadening which occurs when molecules are either static or tumbling slowly, the magnetic fieds surrounding each moelcule are slightly different, as a result, the resonance frequency spreds and yeids a overall diffuse signal.

1.8 Pulsed EPR

Pulsed EPR is an advanced technique of CW EPR in which a series of microwave pulses excite the electron spin and the signal induced by those pulses is acquired. Similar to the basic principle of NMR spectroscopy, B_0 is the static magnetic field establishing the spin equilibrium condition, an additional magnetic field B_1 perpendicular to B_0 is applied to manipulate the magnetization away from the *z*-axis. The subsequent magnetic behavior during its return to equilibrium is detected by detection coils lie in the *x-y* plane, so the transverse magnetization having an *x-y* component is detected to give a signal. Pulses are often named by their tip angles, and the most commonly employed tip angles are $\pi/2$ (90 degrees) and π (180 degrees). A $\pi/2$ pulse tips the magnetization from *z*-axis into the *x-y* plane, then due to the electron spins interaction with their surroundings, the transverse magnetization will decay away and return to equilibrium through relaxation processes after the pulse ends. During this event, the stationary magnetization rotates in the *x-y* plane relaxes back to equilibrium, which generates currents and voltages in the resonator that gives a signal. This is called a Free Induction Decay (FID). Using Fourier transformation (FT), the recorded time-domain signal is converted into frequency-domain spectrum. Detection of FID signal after the microwave pulse must tolerate an approximately 80 ns deadtime, if the FID is very short, it will disappear before the deadtime ends. To overcome this limitation, a subsequent π pulse is applied to regenerate the dissipated signal from the first pulse and it eventually produces an "echo" (Figure 1.8).

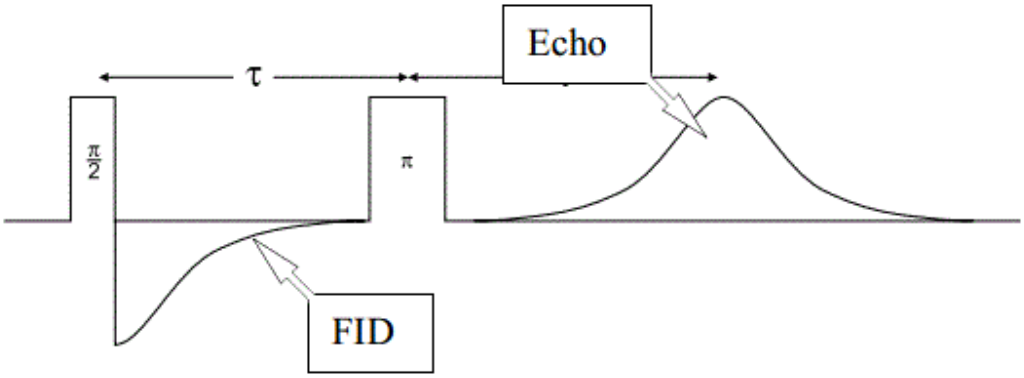

Figure 1.8: *Two-pulse spin echo sequence: a π /2 pulse followed by a π pulse*[39].

In Figure 1.9, first *π/2* pulse rotates the magnetization from *z*-axis to *y*-axis followed by dephasing in *x*-*y* plane in interval time, *τ*. Then *π* pulse inverts the magnetization about *x*-axis, magnetization rotates in the same direction and speed toward equal phasing motion. After all spin packets bunch up along *y*-axis, they will dephase again like a FID.

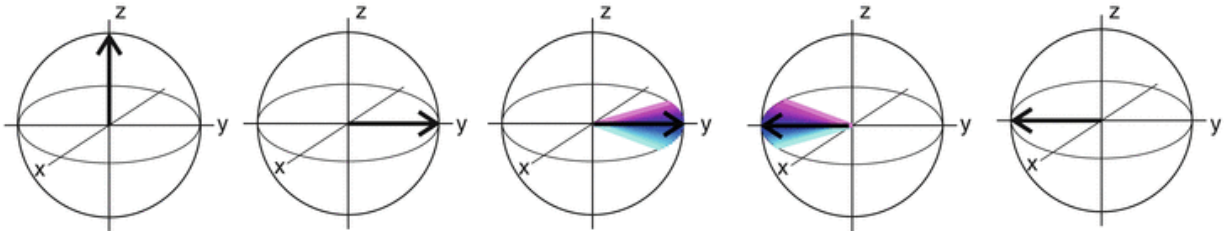

Figure 1.9: *Dephasing and refocusing of magnetization during a two-pulse spin echo*[40].

In Chapter 4, we used hyperfine sub-level correlation (HYSCORE), a six-pulse EPR technique, to characterize the anisotropic component of hyperfine interactions between un-paired electron and the protons in vicinity. The basic introduction of HYSCORE will be given in Chapter 4.

1.9 Doctoral Research Plan

The overall goal of this project is to develop novel magnetic resonance methods for studies of the structure of monolignol radicals generated from enzymatically catalyzed oxidative dehydrogenation under biologically relevant conditions and to provide information on magnetic parameter of monolignol-based radicals to be used as a "fingerprint" for identification of lignin-based radical species.

Specifically, we have the following objectives:

(1) Use spin-trapping EPR method to trap the enzyme-catalyzed transient monolignol radicals and deduce the structure of radicals from the characteristic feature of EPR spectra of spin adducts.

(2) Use continuous-flow enzyme surface immobilization in combination with EPR spectroscopy to study the monolignol radicals generated in situ.

(3) Use CW EPR and 2D HYSCORE spectroscopy to characterize the monolignol radicals photogenerated at 77 K to provide information on hyperfine tensor of the radicals to potentially be used as a "fingerprint" to identify lignin-based radicals.

(4) Design a method to study the radical structure of water-insoluble monolignol using continuous-flow EPR spectroscopy. Introduce enzymatic deglucosidation of monolignol glucoside prior to oxidative dehydrogenationto of monolignol to circumvent the difficulty of monolignol solubility in aqueous buffer.

CHAPTER 2

Spin-trapping EPR Study of Radicals Formed upon HRP/H_2O_2-Catalyzed Oxidation of Monolignols

2.1 Introduction to spin-trapping technique

Spin trapping was used to detect phenolic-like compounds, but was mostly utilized to trap protein-base radicals, like tyrosine radicals or small reactive radicals accompanying enzyme-catalyzed reactions[41]. ^{31}P NMR spin-trapping was found to be informative in identification of intermediate phenolic radical species[42]. This work demonstrated that some of monolignol-based radicals can react with spin trap very similar in structure to DMPO spin trap used in our work, with exception of phenols with very bulky substituents. Using sensitivity of ^{31}P NMR shift to the nature of trapped radical, the authors demonstrated formation of phenoxy-radical adduct as well as formation of carbon-centered radicals. NMR spin trapping requires high sample volumes (up to 1 ml)[42], as compared to maximum of 20 ul samples used in conventional EPR spin-trapping experiments or maximum of 200 uL if flat cell EPR is used. NMR spin-trapping also requires buildup of higher concentration of a spin-adduct. For example, the final concertation of phenolic compounds used in the work mentioned above was 5 mM[42]. The advantage, however, is in stability of diamagnetic adducts, allowing for long averaging of the NMR signal. NMR spin trapping, in a way similar to EPR spin-trapping, requires generation and characterization of model radicals and corresponding adducts to establish ^{31}P signal dependence upon the structure of trapped

radical. Low concentration sensitivity of the MNR spin trapping could hinder application of this method to biologically relevant systems.

Monolignol radicals generated in solution are found to undergo rapid recombination reaction into diamagnetic species, resulting in the stationary state concentration of radicals below the detection limit of the EPR spectrometer. Thus, to overcome sensitivity problems due to short lifetime of monolignol radicals, a simple expedient method – EPR spin-trapping was introduced. EPR spin-trapping is a technique for detecting and identifying short-lived free radicals by intercepting them with diamagnetic compounds (e.g., nitrone compounds) called "spin traps" and converting them into more stable EPR-detectable radicals, or "spin adducts". The structures of the monolignol radicals trapped by spin trap can be deduced from the characteristic features of EPR apectra of the spin adducts. The g-value, splitting pattern, values of the nitrogen and other nuclear hyperfine splitting constants and peak- to-peak line width of individual lines are all important features that contribute to an assignment of structure for the spin adduct.

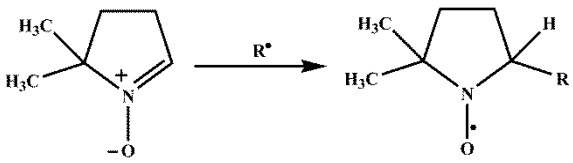

Figure 2.1: *Scheme of the spin-trapping reaction using DMPO.*

The spin trap we used in this work is 5,5-Dimethyl-1-Pyrroline-N-Oxide (DMPO) (Figure 2.1). Two reasons to employ this spin trap are: 1) the spin adducts of short-lived radicals and DMPO demonstrate relatively long lifetime, for example, 20 minutes for DMPO-OH adduct and 1 minute for DMPO-O_2^- adduct at pH=7; 2) there exists a large library of hyperfine splitting constants assigned to a wide variety of spin adducts of DMPO,

which is useful for spectra assignments to characterize the unknown spin adducts generated in experiment. The structure of DMPO spin adduct has one nitroxide group (N-O$^{\bullet}$) as a three π-electron two-atom function group in which unpaired electron occupies a π^* orbital localized at the N-O bond. Since there is also an N-O σ-bond, the effective N-O bond order is 1.5. A covalent attachment of a transient radical to carbon atom of the nitrone group of the spin trap results in formation of a stable nitroxide radical.

The EPR spectrum of spin adducts in non-viscous solvents exhibit large nitrogen hyperfine splitting and additional hyperfine splitting from hydrogen adjacent to the nitrogen atom of the nitroxide moiety. The precise value of nitrogen splitting, α_N, is critically dependent on the nature of substituents at nitrogen atom and polarity of the medium, usually found in the range *ca.* 4 to *ca.* 30 G. Generally, an increase in solvent polarity results in the increase in α_N due to the increase of spin density on the nitrogen atom, and correspondingly cause the decrease in β-H hyperfine splitting $\alpha_{H\beta}$. $\alpha_{H\beta}$ is mainly dependent upon the structure of the trapped radicals affecting the unique dihedral angle θ between α-C-N p_z-orbital and N-α-C-β-H planes. This angular dependence relationship is well described by Heller-McConnell equation[43],

$$\alpha_{H\beta} = B_0 + B_2 cos^2\theta \qquad (2.1)$$

where B_0 and B_2 are constants ($B_0 \cong 0$ and $B_2 \cong 26.8\ G$ for nitroxide).

Thus, small difference in the bulkiness of the groups attached to the α-C lead to the unique $\alpha_{H\beta}$. In Figure 2.2, the hyperfine splitting pattern of DMPO spin adduct of $^{\bullet}$OH radical ($\alpha_N = \alpha_H$= 14.9 G) in water is shown as an example.

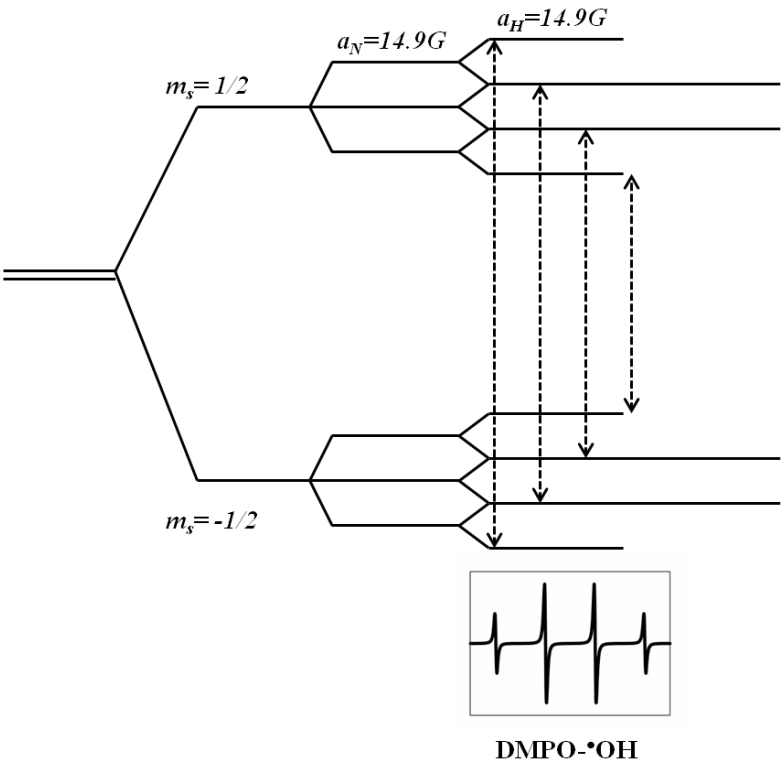

Figure 2.2: *The hyperfine splittings of DMPO-•OH spin adduct in aqueous solution and its corresponding EPR spectrum.*

Oxygen-centered radicals, such as hydroxyl radical (•OH) and superoxide radical ($^{\bullet}O_2^-$) are common intermediates in reactions occurring in biological system. The reaction of DMPO with radicals is very fast, for example, it is producing DMPO-•OH radical with k= 2 * 10^9 $M^{-1}s^{-1}$ [44]. Since the *g*-factors for different DMPO spin adducts only slightly varies no matter what type of radical is trapped, the signals of DMPO-•OH and DMPO-$^{\bullet}O_2^-$ species often overlap with signals from other spin adducts, thus significantly complicating the overall EPR spectrum. In our work, the monolignol radicals with the unpaired electron localized on phenolic oxygen atom and/ or carbon atoms in resonance structure are expected to be trapped to produce the corresponding DMPO-•oxygen and/ or DMPO–•carbon spin adducts. With the uncertainty about the unpaired electron location and the interference from DMPO-OH

and DMPO-$^{\bullet}O_2^-$, the identification of signal associated with DMPO-$^{\bullet}$monolignol spin adduct and their correct assignment seem to be challenging.

The general procedure for identification of the structure of spin adduct from its EPR spectrum is to numerically simulate EPR spectrum, determine hyperfine parameters and the nature of hyperfine splitting and carefully compare the data to those spin adduct structures unambiguously assigned in library. It should be considered that the splitting constants may vary based on the type and bulkiness of the trapped radical and polarity of solvent environment. Quantity of radical is proportional to the intensity of its EPR spectrum, which can be determined by double-integration of first derivative EPR signal and comparison with a reference sample.

Precautions should be taken, however, to avoid misinterpretation of the observed EPR signals in spin-trapping experiments, as in some cases radical species could be formed by mechanisms other than direct spin-trapping of short-lived radical. For example, in the O_2-saturated solutions, addition of DMPO could result in formation of DMPO-$^{\bullet}$OH adduct through the mechanism that does not involve trapping of $^{\bullet}$OH radicals (Figure 2.3). Therefore, additional control experiments should be conducted to eliminate possibility of the spin adducts formation through alternative, non-radical mechanisms[44].

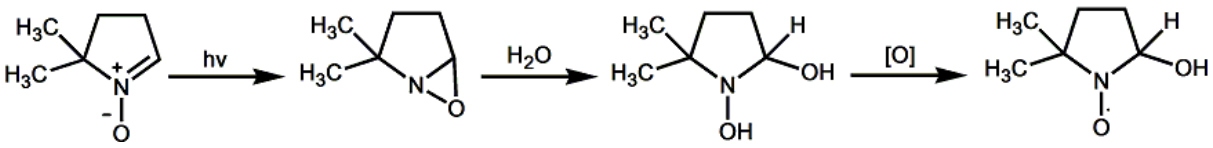

Figure 2.3: *Formation of DMPO-$^{\bullet}$OH adduct through the reaction not involving trapping of $^{\bullet}$OH radical.*

2.2 Materials and reagents

Abbreviations used in the text: Horseradish peroxidase (HRP), 2,2'-Azino-bis(3-ethylbenzothiazoline-6-sulphonic acid) (ABTS), 5,5-Dimethyl-1-Pyrroline-N-Oxide (DMPO)**,** Dimethyl sulfoxide (DMSO).

HRP (Type II) and laccase (from *Trametes versicolor*) were purchased from Sigma Chemical Co Ltd and used without further purification. Methyl *p*-coumarate was provided by our collaborator Dr. Wayne Zeller (USDA). Coniferyl alcohol was synthesized using previously published procedures. DMPO was purchased from Enzo Life Sciences and additionally purified by vacuum distillation and treated with charcoal. ABTS was purchased from Amresco. Desferoxamine mesylate was used as chelating agent to prevent HRP inactivation by trace heavy metals in buffer salts and transition metal-induced decomposition of H_2O_2.

Synthesis of coniferyl alcohol[36]: Ethyl 4-hydro-3-methoxycinnamate (2.33g, 10.41 mmol) in anhydrous toluene (50 ml) was reduced by dropwise addition of diisobutylaluminum hydride (DIBAL-H) (10.41 ml, 10.41 mmol) via a dropping funnel over 10 min at 0 ℃ under argon. After 1h the reaction was complete and quenched with ethanol. Water was added and the product was exhaustively extracted in ethyl acetate. The organic layer was then dried over anhydrous Na_2SO_4 and filtered and solvent was removed in vacuum. Recrystallization from hexanes/ethyl acetate gave coniferyl alcohol (yield 46%): ^{1}H NMR ($(CD_3)_2SO$), 4.08 (d, 2H, CH_2OH), 6.18 (d, t, 1H, CH=CH), 6.42 (d, 1H, CH=CH), 6.71 (s, 1H, H5), 6.75 (d, d, 1H, H6), 7.00 (d, 1H, H2) ppm; ^{13}C NMR ($(CD_3)_2SO$), 56.21 (OCH_3), 62.41 (Cγ), 110.36 (C2), 116.12 (C5), 120.11 (C6), 128.17 (Cβ), 129.17 (C1), 129.66 (Cα), 146.83 (C4), 148.38 (C3) ppm.

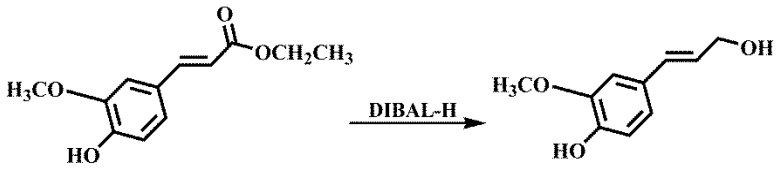

Figure 2.4: *Scheme of the synthesis of coniferyl alcohol.*

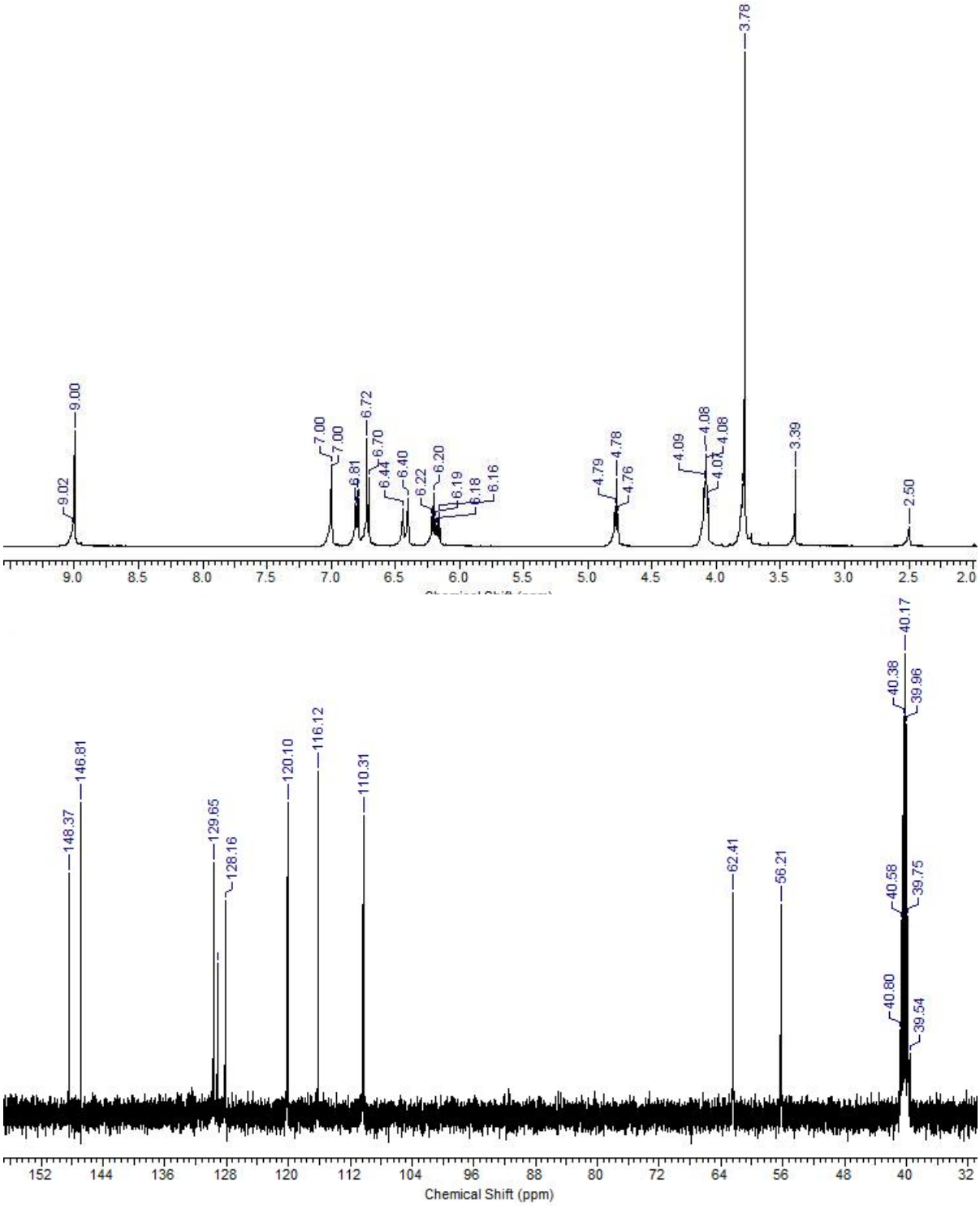

Figure 2.5: *1H and 13C NMR spectra of coniferyl alcohol.*

2.3 Enzyme assay in buffer containing organic solvent

Due to limited solubility of monolignols in aqueous buffer solutions, DMSO or CH_3CN were used as a co-solvent with buffer. However, the presence of organic solvent (even in concentration of a few volume %) may cause a significant decrease of the enzyme activity. To investigate effect of organic solvents on enzyme activity and find out the best ratio between an organic solvent and a buffer to accommodate the solubility of different monolignols and to ensure acceptable activity loss of enzymes, enzyme assay was conducted in organic solvent-buffer mixtures in 0.5:9.5 (v/v) and 1:9 (v/v) ratios. ABTS was used as a substrate for HRP/H_2O_2 or laccase to form a green radical cation that could be measured by absorbance at 420 nm ($\varepsilon_{420nm} = 3.6 \times 10^4\ M^{-1}cm^{-1}$) in a steady-state kinetics. The enzyme assay relies on measurement of the increase in the reaction product concentration as a function of time during the initial period of reaction using UV-vis spectrophotometry. Solutions of ABTS (pH=5.5 and pH=7), HRP (pH=7) and laccase (pH=5.5) were prepared in phosphate buffers (40 mM) with suitable concentrations (Table 2.1) to ensure the acceptable range of absorbance at 420 nm. The experiment was conducted using Varian Cary 50 Bio UV-Vis spectrophotometer equipped with kinetics software module. The increase in absorbance at 420 nm was monitored for 2 min period upon initiation of the reaction by addition of H_2O_2 to the mixture containing ABTS and HRP or by addition of laccase to ABTS.

2.4 EPR spin-trapping experiment

2.4.1 CW EPR spectroscopy

Room temperature CW EPR measurements were conducted using Bruker ELEXSYS E500 spectrometer operating at approximately 9.5 GHz (X-band). The modulation amplitude was 0.5 G and the modulation frequency was 100 kHz. The time constant was set at 20.48 ms with a 29.65 ms conversion time and a 30.36 s sweep time. 1024 point spectra were collected over a 100 G range. The incident microwave power was 2 mW. Liquid samples were drawn in glass capillaries (0.81 i.d. × 1.42 mm, Jaguar Industries, Inc., Haverstraw, NY) to ensure high Q-factor of the resonator. The capillary was sealed at both ends and inserted with a standard EPR tube into the resonator. EPR spectra were collected sequentially over 30 min for each sample. Averaged spectra were obtained by post-processing depending on the lifetime of spin adducts.

2.4.2 Preparation of samples for EPR spin-trapping experiments

Two monolignols, coniferyl alcohol and methyl *p*-coumarate, were used in EPR spin-trapping experiments. Mixtures of phosphate buffer with either CH_3CN or DMSO (1:9) were used to prepare monolignol solutions. Solutions of DMPO, HRP and desferoxamine mesylate were prepared in 40 mM pH=7.0 phosphate buffer. Final reaction mixtures prepared in glass vessels contained DMPO (300 mM), HRP (10.00 μM), deferoxamine (16.25 μM), monolignol (2.5 mM) and H_2O_2 (100.00 μM) in organic solvent: buffer (1:9) reaction environment. Each reaction mixture was freshly prepared and EPR data acquisition was started immediately after preparation. Control spin-trapping experiments were conducted using samples as described above, but in the absence of monolignol.

2.4.3 EPR spectral simulation

EPR spectral simulations were done utilizing PEST WinSim program[45]. The standard simulation approach involved using measured or theoretical hyperfine splitting constants to obtain a computer-calculated spectrum and then compare it with the experimental spectrum. All the parameters in simulation for each species were sequentially varied until a minimum in the error surface is located. Goodness of the fit was determined by visual inspection and by comparing the sum of the squared residuals. Based on the hyperfine splitting constants reported in spin-trapping database (maintained by National Institute of Environment Health Sciences[46]) and other database[47] and influence of polarity and viscosity of solvent, each species and corresponding hyperfine splitting constants were preliminary assigned. Convx (Alex I. Smirnov, NCSU) program was used to determine the intensity of EPR spectra. All of the spectral simulation data are summarized in Table 2.3.

2.5 Results and discussion

Plotting the increase of concentration of ABTS green radical cation (*y*-axis) during the period of 1 min (*x*-axis) yields a linear relation from which the slope representing the initial velocity of enzymolysis was calculated. As the results shown in Figure 2.7, a linear relationship exists between the loss of HRP activity and increase of organic solvent content. HRP demonstrates somewhat better tolerance to DMSO (75% of activity in 0.5:9.5 mixture and 54% in 1:9 mixture) than CH_3CN (67% in 0.5:9.5 mixture and 47% in 1:9 mixture), however, the effect of both co-solvents is comparable. In general, laccase shows lower tolerance to the presence of organic co-solvents compared to HPR (Figure 2.8). Laccase preserves only 38% of activity in DMSO: buffer (1:9 mixture) which is lower than 50%

activity in CH_3CN: buffer (1:9 mixture). Compared to HRP, relative effect of the co-solvents is reversed: laccase losses more activity in the presence of DMSO than in the presence of CH_3CN. We employed both CH_3CN and DMSO as a co-solvent in spin-trapping experiment. Since the loss of activity of HRP is comparable for DMSO and CH_3CN, we compared quantitative results of EPR spin-trapping experiments in DMSO/buffer and CH_3CN/buffer mixtures.

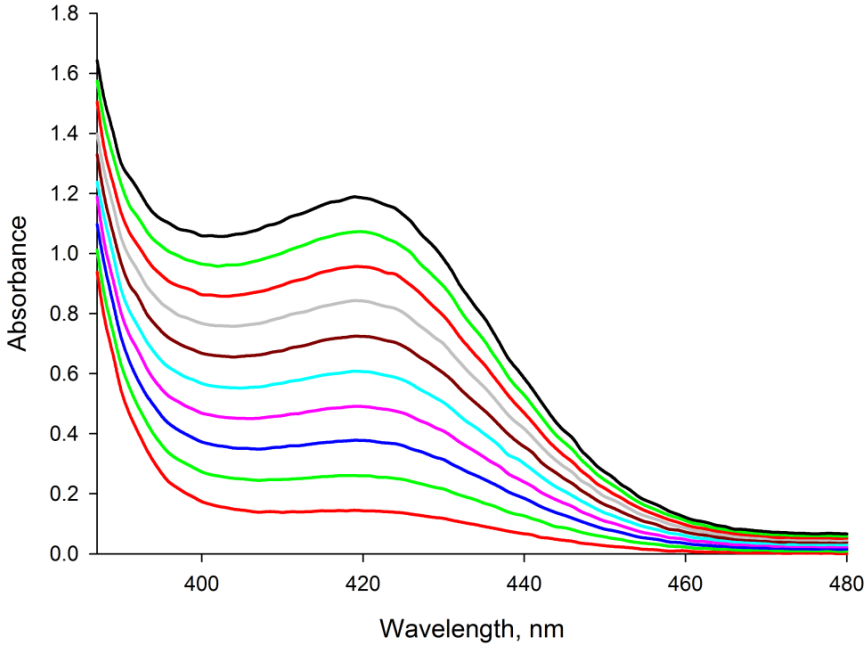

Figure 2.6: *The increase of absorbance of the product of oxidation of ABTS by HRP in 100% buffer.*

Table 2.1: *Concentration of reagents used in enzyme assay*

Reagent	**ABTS**	**HRP**	**H_2O_2**	**Laccase**
Final Concentration	1000 μM	0.005 μM	100 μM	0.3 U/mL

Table 2.2: *Initial rates (uM/min) of enzymolysis in various solvent compositions.*

HRP in 100% buffer	**HRP in buffer: CH_3CN (9.5: 0.5)**	**HRP in buffer: CH_3CN (9: 1)**	**Doubled HRP in buffer: CH_3CN (9: 1)**	**HRP: in buffer: DMSO (9.5: 0.5)**	**HRP: in buffer: DMSO (9: 1)**	**Doubled HRP in buffer: DMSO (9: 1)**
32.06	21.56	15.03	27.78	24.01	17.30	32.39
Laccase in 100% buffer	**Laccase in buffer: CH_3CN (9: 1)**	**Laccase in buffer: DMSO (9: 1)**		**2.1 fold of laccase in buffer: CH_3CN (9: 1)**		**2.6 fold of laccase in buffer: DMSO (9: 1)**
36.30	17.63	13.89		32.25		32.16

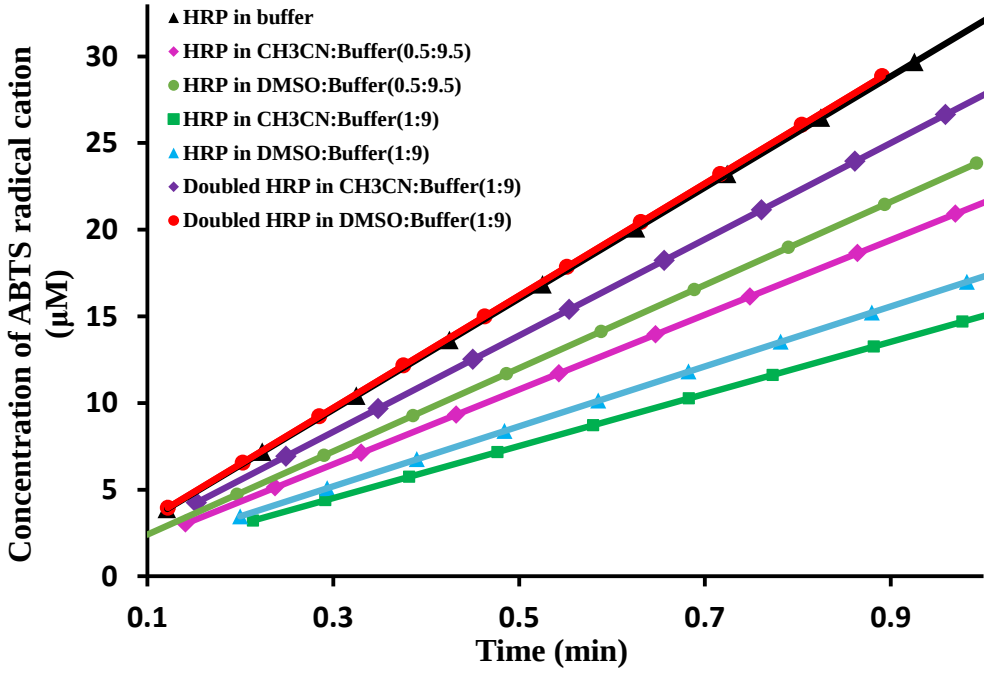

Figure 2.7: *Initial rates of HRP enzymolysis as a function of solvent composition.*

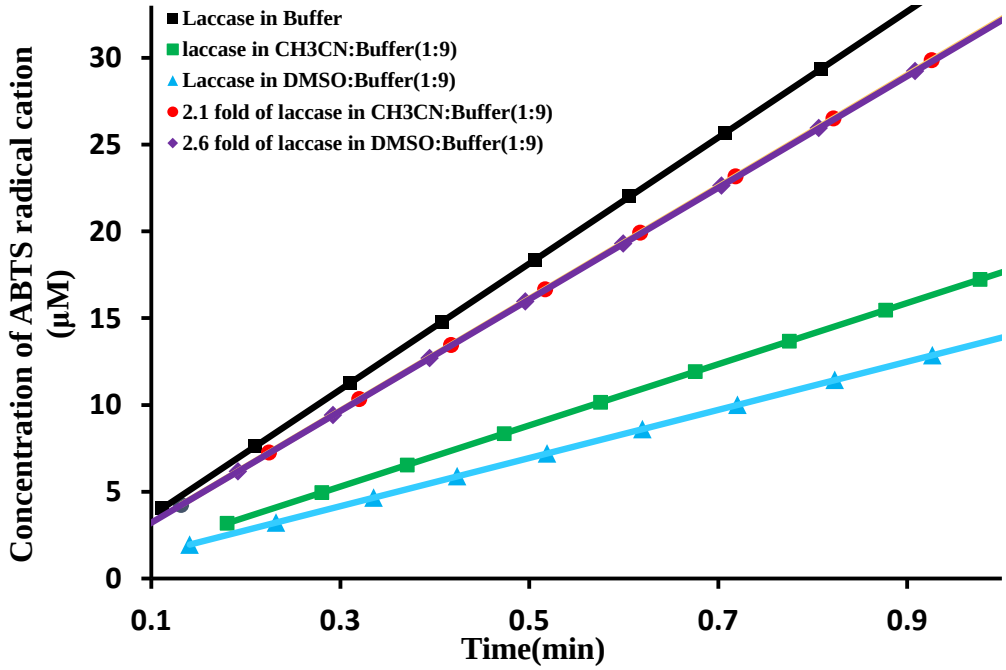

Figure 2.8: *Initial rates of laccase enzymolysis as a function of solvent composition.*

EPR signals of all spectra decayed dramatically fast, which only allowed for data acquisition for ~ 5 min (~ 10 scans). The sequentially collected spectra were averaged to obtain a moderate signal-to-noise ratio.

Control experiments in the absence of monolignols

Figure 2.9 and Figure 2.10 show EPR spectra detected in two control experiments in the presence of DMPO, HRP, H_2O_2, but in the absence of monolignol in buffer containing either CH_3CN or DMSO as organic co-solvent. Both experimental and simulated spectra are shown. On the basis of hyperfine coupling constants, the spin adducts formed in control experiment in CH_3CN-buffer mixture were identified as DMPO-$^{\bullet}$OH and DMPO-$^{\bullet}$OOH, respectively, and these two species were also found in control experiment in DMSO/buffer mixture. Hydroxyl ($^{\bullet}$OH) and hydroperoxyl ($^{\bullet}$OOH) radicals are the known intermediates in the catalytic cycle of HRP in the presence of H_2O_2. Decomposition of H_2O_2 provides another pathway for $^{\bullet}$OH radical formation[48]. The observed reduction in the overall intensity of the EPR signal, as well as in the relative intensity of the DMPO-$^{\bullet}$OH in the control experiment using DMSO as a co-solvent, as compared to using CH_3CN as a co-solvent, is readily explained by quenching of hydroxyl radicals by DMSO. The observation of residual intensity of DMPO-$^{\bullet}$OH in the experiment with DMSO containing buffer indicates that the remaining DMPO-$^{\bullet}$OH could be either a) a result of decomposition of OOH- adduct, or b) incomplete quenching of $^{\bullet}$OH radical. Both scenarios are possible.

To verify the assignment of $^{\bullet}$OOH radical, we also conducted the control experiments with presence of 100 units of superoxide dismutase (SOD). SOD is known to catalyze the conversion of superoxide radicals into hydrogen peroxide and molecular oxygen. For the

sample prepared with CH_3CN, addition of SOD resulted in significant, at least by a factor of 2, decrease in the overall EPR signal intensity. In addition, the relative intensity of the DMPO-$^{\bullet}$OH adduct increased relative to the superoxide radical adduct, consistent with SOD removing OOH from the reaction mixture. In samples containing DMSO as a co-solvent, addition of SOD resulted in almost complete loss of the EPR signal, with the remaining intensity characteristic of DMPO-$^{\bullet}$OH. Drastic loss of EPR intensity in this experiment is expected as effective quenchers for both hydroxyl (DMSO) and superoxide radicals (SOD) are present in the reaction mixture.

Reactions with methyl p-coumarate

In the presence of methyl *p*-coumarate in reaction in CH_3CN-buffer mixture, as shown in Figure 2.11, besides $^{\bullet}$OH and $^{\bullet}$OOH radicals, a new species (α_N(G)=15.11 and $\alpha_{\beta H}$(G)= 17.12) was observed and assigned as phenoxy ($^{\bullet}OC_6H_4R$) radical. Hyperfine parameters for DMPO-$^{\bullet}OC_6H_4R$ adduct in dichloromethane as a solvent is reported as α_N(G)=12.9, $\alpha_{\beta H}$(G) =8.4[49]. In more polar solvents, as in our experiments, the hyperfine on nitrogen is expected to increase as well as the hyperfine splitting on the β-H nuclear. . The assignment was made also based on reported parameters for oxygen-centered radical adducts formed by $^{\bullet}$O-C$(CH_3)_3$, (α_N(G) =15.0, $\alpha_{\beta H}$(G) =16.8, aqueous solution, neutral pH) and $^{\bullet}$O-C(R) (α_N(G)=14.7, $\alpha_{\beta H}$(G)=16.9, aqueous solution, neutral pH). The other reported adducts with similar characteristics are all formed from sulfur-based radicals. We have considered to assign this signal to DMPO-$^{\bullet}CH_2$(CN) compound. Potentially, detected adduct could be formed by reaction with acetonitrile used as a co-solvent, as it was observed in case of DMSO. Data on hyperfine parameters of DMPO-$^{\bullet}CH_2$(CN) are absent in the database.

Parameters for DMPO adduct of $C(CH_3)CN$ in xylene as a solvent is reported as α_N(G)=14.6, $\alpha_{\beta H}$(G) =20.9[50]. Considering the influence of solvent polarity, one would expect the hyperfine parameter on β-hydrogen to be much higher than 17.12 G observed in our experiments. Overall, all carbon-centered radicals demonstrate very high hyperfine splitting on the β-hydrogen, typically above 22 G, making it highly unlikely that the component observed in our experiment comes from reaction with acetonitrile.

Upon addition of methyl *p*-coumarate to the reaction mixture with DMSO as a co-solvent (shown in Fig 2.12), in addition to the dominating DMPO-•OOH adduct and a very weak DMPO-•OH adduct, a species with (α_N(G)=16.24 and $\alpha_{\beta H}$(G)=23.10) was found and assigned to a carbon-centered radical (•CH_3). This species is likely a methyl radical adduct. Methyl radical is a product of the reaction between DMSO and hydroxyl radical. DMSO is a highly effective quencher of the hydroxyl radicals, and it reacts with hydroxyl radicals at a faster rate than spin trap DMPO. Reduction in relative intensity of the OH-adduct and a simultaneous appearance of methyl-adduct confirm that OH-adduct is formed by a direct trapping of the •OH radical and not a result of decomposition of superoxide adduct. However, for the type of methly *p*-coumarate molecule, two types of carbon radicals could be formed resulting in spin adducts with very similar hyperfine parameters, tertiary (•CHR) and quaternary (•CR), are both possible to be produced. The explicit structure of generated carbon radical cannot be simply derived by direct hyperfine comparison.

Surprisingly, we did not detect formation of phenoxy (•OC_6H_4R) adducts in the presence of DMSO. This observation suggests that formation of phenoxy radicals is mediated by hydroxyl radicals, but not •OOH radical.

To further investigate the role of hydroxyl radicals in formation of the signal assigned to phenoxy adduct, we added SOD to the reaction mixtures. As expected addition of SOD to DMSO containing system resulted in almost complete loss of EPR signal with remaining intensity contributed from hydroxyl adduct. Addition of SOD to CH_3CN containing mixture resulted in partial loss of the EPR intensity accompanied by an increase in relative contribution from hydroxyl adduct. Smaller, but measurable increase in relative contribution of the signal tentatively assigned to phenoxy radical adduct was observed, supporting our suggestion that its formation is mediated by hydroxyl radical.

Reactions with coniferyl alcohol

In Figure 2.13 and 2.14, the reaction of coniferyl alcohol with HRP/H_2O_2 system in the presence of DMPO trap was found to generate $^{\bullet}OH$, $^{\bullet}OOH$ radicals and adducts tentatively assigned to $^{\bullet}OC_6H_3R$ radical in CH_3CN-buffer mixture and $^{\bullet}OH$, $^{\bullet}OOH$ and $^{\bullet}CH_nR$ in DMSO-buffer mixture. From our results, the methoxyl substitution and functional group on side monolignol chain have no observable influence on the magnetic parameters of radical species, as expected because these substitutions are very distant to the nitrogen and hydrogen nuclei, but the solvent environment of reaction played an important factor that $^{\bullet}OC_6H_3R$ is found as dominate species produced in CH_3CN-buffer while it is not formed in the systems containing DMSO.

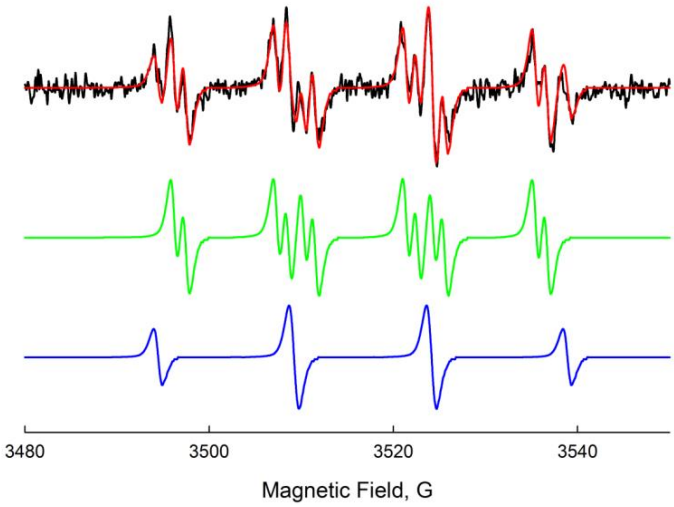

Figure 2.9: *Room temperature CW EPR spectra obtained from control experiments in the mixture of DMPO, HRP and H_2O_2 in CH_3CN-buffer 1:9 mixture in the absence of monolignol and corresponding simulations. (Black) Experiment spectrum. (Red) Spectral simulation. (Green) Spin species assigned as DMPO-$^{\bullet}$OOH. (Blue) Spin species assigned as DMPO-$^{\bullet}$OH.*

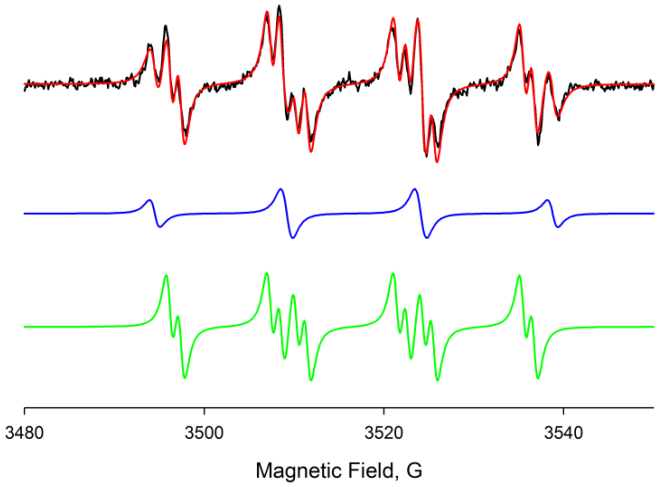

Figure 2.10: *Room temperature CW EPR spectra obtained from control experiments in the mixture of DMPO, HRP and H_2O_2 in DMSO-buffer 1:9 mixture in the absence of monolignol and corresponding simulations. (Black) Experiment spectrum. (Red) Spectral simulation. (Green) Spin species assigned as DMPO-$^{\bullet}$OOH. (Blue) Spin species assigned as DMPO-$^{\bullet}$OH.*

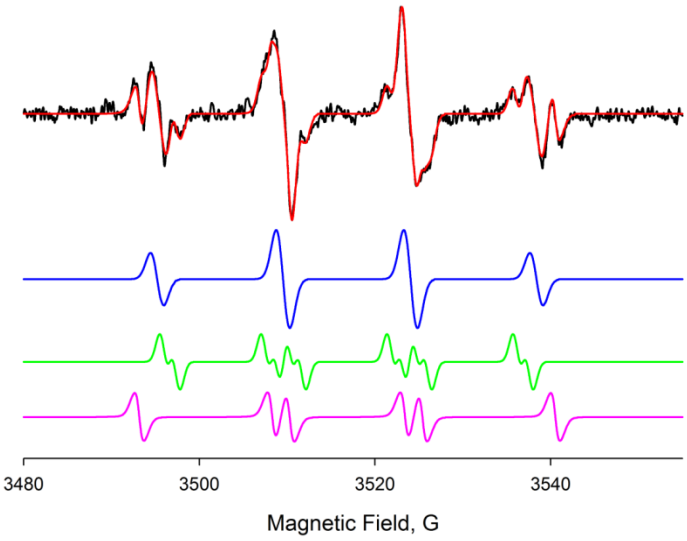

Figure 2.11: *Room temperature CW EPR spectra obtained from the reaction of DMPO, HRP, methyl p-coumarate and H_2O_2 in CH_3CN-buffer 1:9 mixture and corresponding simulations. (Black) Experiment spectrum. (Red) Spectral simulation. (Green) Spin species assigned as DMPO-$^{\bullet}OOH$. (Blue) Spin species assigned as DMPO-$^{\bullet}OH$. (Pink) Spin species assigned as DMPO-$^{\bullet}OC_6H_4R$.*

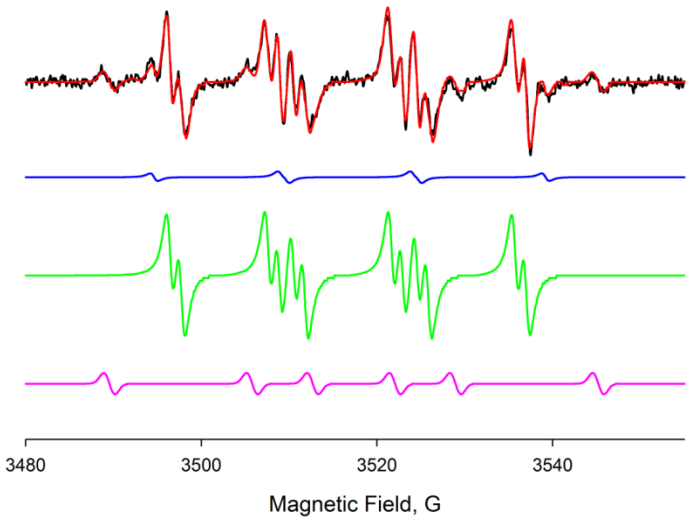

Figure 2.12: *Room temperature CW EPR spectra obtained from the reaction of DMPO, HRP, methyl p-coumarate and H_2O_2 in DMSO-buffer 1:9 mixture and corresponding simulations. (Black) Experiment spectrum. (Red) Spectral simulation. (Green) Spin species assigned as DMPO-$^{\bullet}OOH$. (Blue) Spin species assigned as DMPO-$^{\bullet}OH$. (Pink) Spin species assigned as DMPO-$^{\bullet}CH_nR$.*

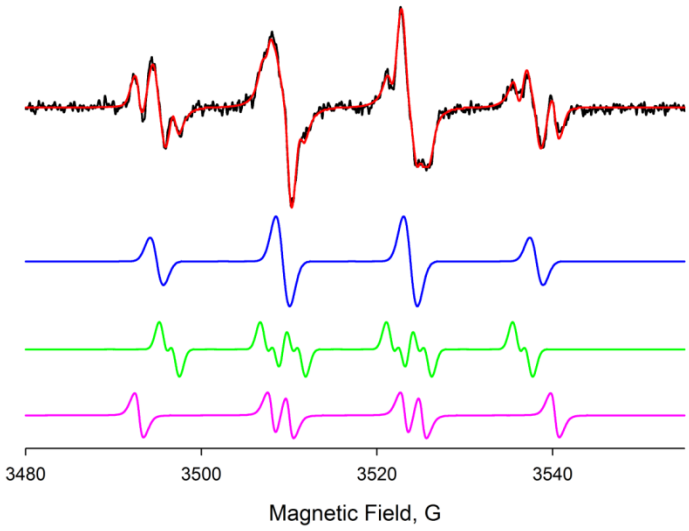

Figure 2.13: *Room temperature CW EPR spectra obtained from the reaction of DMPO, HRP, coniferyl alcohol and H_2O_2 in CH_3CN-buffer 1:9 mixture and corresponding simulations. (Black) Experiment spectrum. (Red) Spectral simulation. (Green) Spin species assigned as DMPO-$^{\bullet}OOH$. (Blue) Spin species assigned as DMPO-$^{\bullet}OH$. (Pink) Spin species assigned as DMPO-$^{\bullet}OC_6H_3R$.*

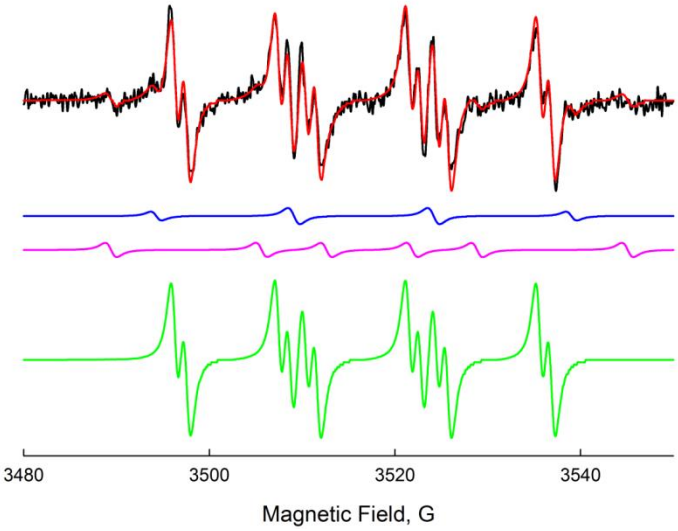

Figure 2.14: *Room temperature CW EPR spectra obtained from the reaction of DMPO, HRP, coniferyl alcohol and H_2O_2 in DMSO-buffer 1:9 mixture and corresponding simulations. (Black) Experiment spectrum. (Red) Spectral simulation. (Green) Spin species assigned as DMPO-$^{\bullet}OOH$. (Blue) Spin species assigned as DMPO-$^{\bullet}OH$. (Pink) Spin species assigned as DMPO-$^{\bullet}CH_nR$.*

Table 2.3: *Parameters of simulated EPR spectra for DMPO spin adducts obtained from the mixtures of DMPO, HRP, H_2O_2 and monolignol in organic- buffer 1:9 mixture.*

Control experiment in CH_3CN-buffer	DMPO-$^{\bullet}$OH (39.9%)		DMPO-$^{\bullet}$OOH (60.1%)
$\alpha_N(\mathbf{G})$	14.91		14.03
$\alpha_{\beta H}(\mathbf{G})$	14.47		11.13
$\alpha_{\gamma H}(\mathbf{G})$			1.25
Control experiment in DMSO-buffer	DMPO-$^{\bullet}$OH (20.2%)		DMPO-$^{\bullet}$OOH (79.8%)
$\alpha_N(\mathbf{G})$	14.89		14.05
$\alpha_{\beta H}(\mathbf{G})$	14.45		11.17
$\alpha_{\gamma H}(\mathbf{G})$			1.21
Methyl *p*-coumarate in CH_3CN-buffer	DMPO-$^{\bullet}$OH (48.5%)	DMPO-$^{\bullet}$OOH (27.9%)	DMPO-$^{\bullet}OC_6H_4R$ (23.6%)
$\alpha_N(\mathbf{G})$	14.66	14.18	15.11
$\alpha_{\beta H}(\mathbf{G})$	14.32	11.82	17.12
$\alpha_{\gamma H}(\mathbf{G})$		1.23	
Methyl *p*-coumarate in DMSO-buffer	DMPO-$^{\bullet}$OH (4.9%)	DMPO-$^{\bullet}$OOH (85.0%)	DMPO-$^{\bullet}CH_nR$ (10.1%)
$\alpha_N(\mathbf{G})$	14.99	14.04	16.24
$\alpha_{\beta H}(\mathbf{G})$	14.56	11.16	23.10
$\alpha_{\gamma H}(\mathbf{G})$		1.26	

Table 2.3 *(continued)*

Coniferyl alcohol in CH_3CN-buffer	DMPO-$^{\bullet}$OH (48.9%)	DMPO-$^{\bullet}$OOH (30.7%)	DMPO-$^{\bullet}OC_6H_3R$ (20.4%)
$\alpha_N(\mathbf{G})$	14.75	14.21	15.09
$\alpha_{\beta H}(\mathbf{G})$	14.02	11.77	17.32
$\alpha_{\gamma H}(\mathbf{G})$		1.35	
Coniferyl alcohol in DMSO-buffer	DMPO-$^{\bullet}$OH (4.6%)	DMPO-$^{\bullet}$OOH (86.9%)	DMPO-$^{\bullet}CH_nR$ (8.5%)
$\alpha_N(\mathbf{G})$	14.57	14.37	16.21
$\alpha_{\beta H}(\mathbf{G})$	14.06	11.67	23.19
$\alpha_{\gamma H}(\mathbf{G})$		1.38	

We examined whether some information about the local structure of monolignol radical could be deduced from EPR spin-trapping method when McConnell equation is applied (Equation 2.1). The local molecular structure is important because it may reflect the features in lignin, like finger prints. The calculated spatial conformation of the spin adducts DMPO-$^{\bullet}OC_6H_nR$ and DMPO-$^{\bullet}CH_nR$ is shown in Figure 2.15. The dihedral angle θ between α-C-N p_z-orbital and N-α-C-β-H planes are calculated to be in the range 36.5 °-36.9 ° for DMPO-$^{\bullet}OC_6H_nR$ and 21.8 °-21.5 ° for DMPO-$^{\bullet}CH_nR$.

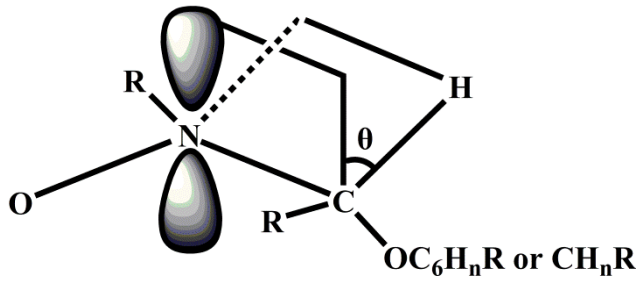

Figure 2.15: *Perspective view of the spin adduct of DMPO-•OC_6H_nR and DMPO-•CH_nR.*

Investigation of free radical formation upon monolignol oxidation catalyzed by laccase

Laccase was also used for the oxidation of coniferyl alcohol and methyl *p*-coumarate, however, only weak EPR signals were detected. The intensity of the observed EPR signal was too low to allow for simulations of spectral line shapes and identification of radicals. Laccase, with lower redox potential compared to HRP, is known to be less active in the oxidation of phenol derivatives. In addition, loss of 50% of activity because of the influence of organic co-solvent further contributed to low concentration of radicals.

2.6 Conclusions

We conducted the DMPO spin-trapping experiments to study the structures of monolignol radicals formed upon oxidation by HRP/H_2O_2 or laccase oxidation. Low polarity CH_3CN and DMSO were used in separate experiments in experiments as co-solvents to improve solubility of monolignols in buffer. Based on the linear relation between the loss of enzyme activity and the increase in the concentration of organic solvent, solvent to buffer ratio 1:9 (v/v) was chosen as the accepted condition in which both HRP and laccase preserved approximately half of the activity observed in aqueous buffer. In control

experiment without monolignol, we have detected the DMPO-$^{\bullet}$OH and DMPO-$^{\bullet}$OOH adducts formed from the reaction of HRP and H_2O_2 in two solvent environment. The assignment of $^{\bullet}$OOH was verified by the reaction with superoxide dismutase. In the presence of methyl *p*-coumarate or coniferyl alcohol in CH_3CN-buffer, besides $^{\bullet}$OH and $^{\bullet}$OOH, $^{\bullet}OC_6H_nR$ adduct was identified. Slight differences in hyperfine parameters of $^{\bullet}$OH and $^{\bullet}$OOH adducts detected in our experiments comparing to values reported for aqueous buffers, is easily explained by the effect of co-solvents. The deviations are consistent with mixed, less polar solvent, used in our experiments. In DMSO-containing buffer, instead of $^{\bullet}OC_6H_nR$, formation of carbon-based $^{\bullet}CH_nR$ was detected for both monolignols. The explicit structure of $^{\bullet}CH_nR$ cannot be disentangled from $^{\bullet}CHR$, $^{\bullet}CR$ (and $^{\bullet}CH_2R$), based on the information on hyperfine, however, it is believed to be methyl radical formed as a result of a reaction of $^{\bullet}$OH with DMSO. The spatial conformation of the spin adducts DMPO-$^{\bullet}OC_6H_nR$ and DMPO-$^{\bullet}CH_nR$ were preliminarily calculated by McConnell equation. The reduced activity of laccase due to the presence of organic co-solvent is not able to create monolignol radical in the level of concentration for EPR detection.

CHAPTER 3

Continuous-flow in Combination with Immobilized Enzyme Electron Paramagnetic Resonance Spectroscopy (IE-EPR) to Study Enzyme-Catalyzed Formation of Monolignol Radicals

3.1 Introduction

The application of spin-trapping technique as described in Chapter 2 provided limited information about monolignol–based radical intermediates and revealed a number of limitations. First, for relatively short-lived radical species, like DMPO-monolignol spin adduct, acquisition of high resolution spectrum is not easy. Rapid monolignol radical recombination reaction prevents the formation of acceptable stationary state concentration of DMPO-monolignol spin adduct whose EPR signal is often overlapped with the signal from other species, especially in biological system. Trapping bulky monolignol radicals is also expected to be less inefficient than trapping of smaller reactive oxygen species due to steric constraints. Oxygen-centered biological radicals created in reaction were difficult to eliminate, the resultant complexity of spectrum is challenging for spectral simulation and radical assignment. Second, the sensitivity of spin-trapping is not infinite to probe the structure details of radicals with unpaired electron on conjugate structures. Third, to increase monolignol solubility and to achieve detectable EPR signal, use of organic co-solvent is necessary, which inevitably lowers the enzyme activity. Therefore, we shifted our focus towards to the continuous-flow EPR spectroscopy.

The conventional continuous-flow method to study enzymatically produced transient radical is through rapid-mixing of two solutions, one containing enzyme and the other containing substrate, to an observation cell. With continuous flowing and mixing, a steady-state concentration of transient radical will generate. However, considering the large consumption of enzyme to perform a two-solution continuous-flow EPR experiment, an alternative method that can provide same high resolution EPR spectra but with less cost of enzyme is developed and called "immobilized-enzyme EPR" (IE-EPR)[51]. Based on the design of this technique, enzyme is immobilized onto an inert support and packed into the EPR flat cell (~100 μl), a substrate solution is flushed into the flat cell and through the immobilized enzyme in adjustable rate to maximize the generation of radical *in situ.* It fully utilizes the catalytic nature of enzyme but only requires small amount of enzyme and substrate. Bradley and co-workers compared the concentration sensitivity of traditional continuous-flow and IE-EPR method by detecting EPR signal from tyrosine radical generated upon HRP-catalyzed reductive cleavage of hydrogen peroxide. They found that the spectrum collected using IE-EPR set-up presents a better signal-to-noise ratio but only consumes ~1/30 of enzyme compared to traditional flow-through method[51-52]. Based on the same idea of utilizing enzyme surface immobilization, we replaced flat cell with quartz capillary (1.6 mm O.D. × 1.3 mm I.D.) as mixing and observation cell to further minimize consumption of an enzyme and monolignol and were able to obtain CW EPR spectra of intermediate monolignol radicals at sufficient signal-to-noise ratio for spectral analysis.

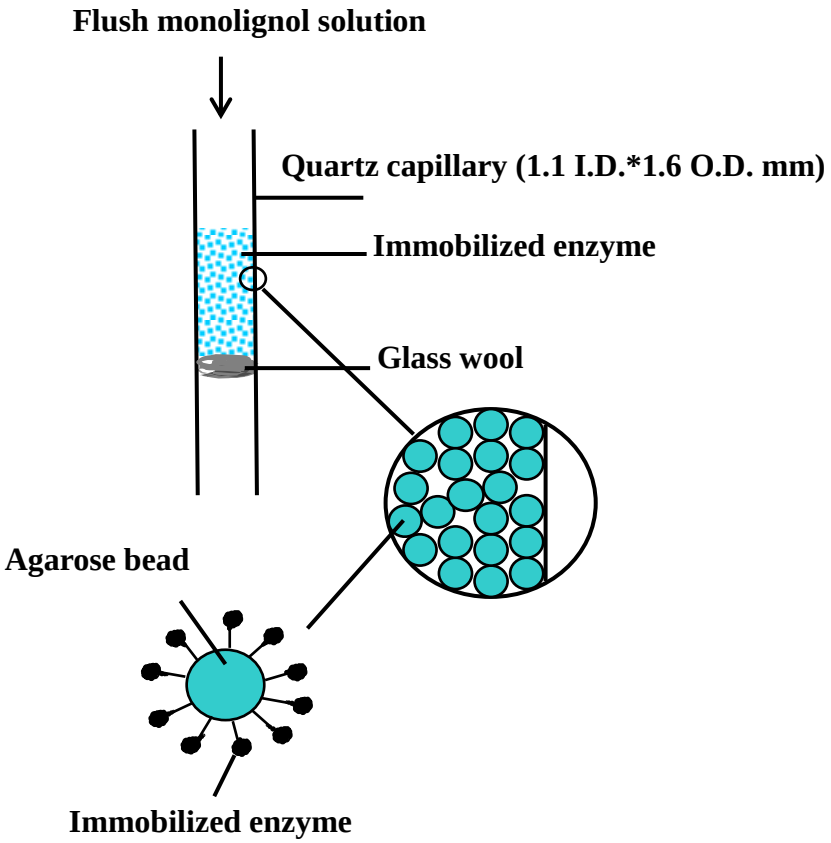

Figure 3.1: *An overview of EPR quartz capillary packed with immobilized enzyme.*

3.2 Materials and reagents

Horseradish peroxidase (HRP, Type II) and laccase (from *Trametes versicolor*) were purchased from Sigma and used without further purification. Affi-Gel 10 and Chelex-100 were purchased from BioRad laboratories. *p*-Coumaric acid, frulic acid, sinapic acid, sinapyl alcohol, methyl *p*-coumarate, ethyl ferulate, coniferyl acetate and sinapyl acetate were provided by our collaborator Dr. Wayne Zeller (USDA). *p*-Coumaryl alcohol, coniferyl alcohol, ethyl sinapate and *p*-coumaryl acetate were synthesized using previously published procedures. Phosphate buffer was made from 10-fold concentration that underwent a 24-hour Chelex-100 treatment. After remove of Chelex-100, diethylenetriaminepentaacetic acid

(DTPA) was added to buffer concentrate which was then diluted to final concentration 50 mM with ultrapure water followed by pH adjustment to 7.4 for HRP and 5.5 for laccase.

Synthesis of Ethyl sinapate[36]: Sinapic acid (2.24g, 10 mmol) was converted to ethyl sinapate in ethanol (50 ml) and acetyl chloride (5 ml). Keep stirring the reaction mixture until all the acid was disappeared. After the solvent was removed in vacuo, the crude product was dissolved in ethyl acetate and washed with sodium bicarbonate (3% w/v). The organic layer was then dried over anhydrous Na_2SO_4 and filtered and solvent was removed in vacuum. Re-crystallization from hexanes/ethyl acetate gave ethyl sinapate (yield 63%): ^{1}H NMR ($(CD^3)^2SO$), 1.27 (t, 3H, CH_2CH_3), 3.81 (s, 6H, OCH_3), 4.17 (q, 2H, CH_2CH_3), 6.58 (d, 1H, CH=CH), 7.05 (s, 2H, H2 and H6), 7.58 (d, 1H, CH=CH) ppm.

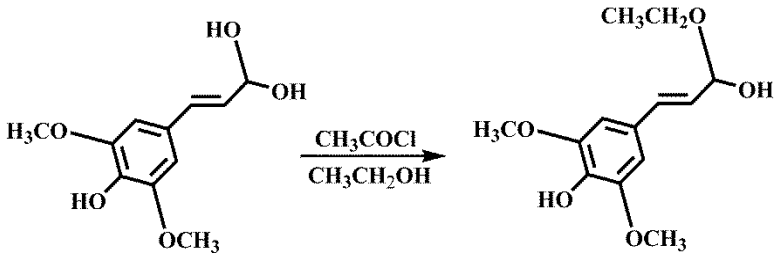

Figure 3.2: *Scheme of the synthesis of ethyl sinapate.*

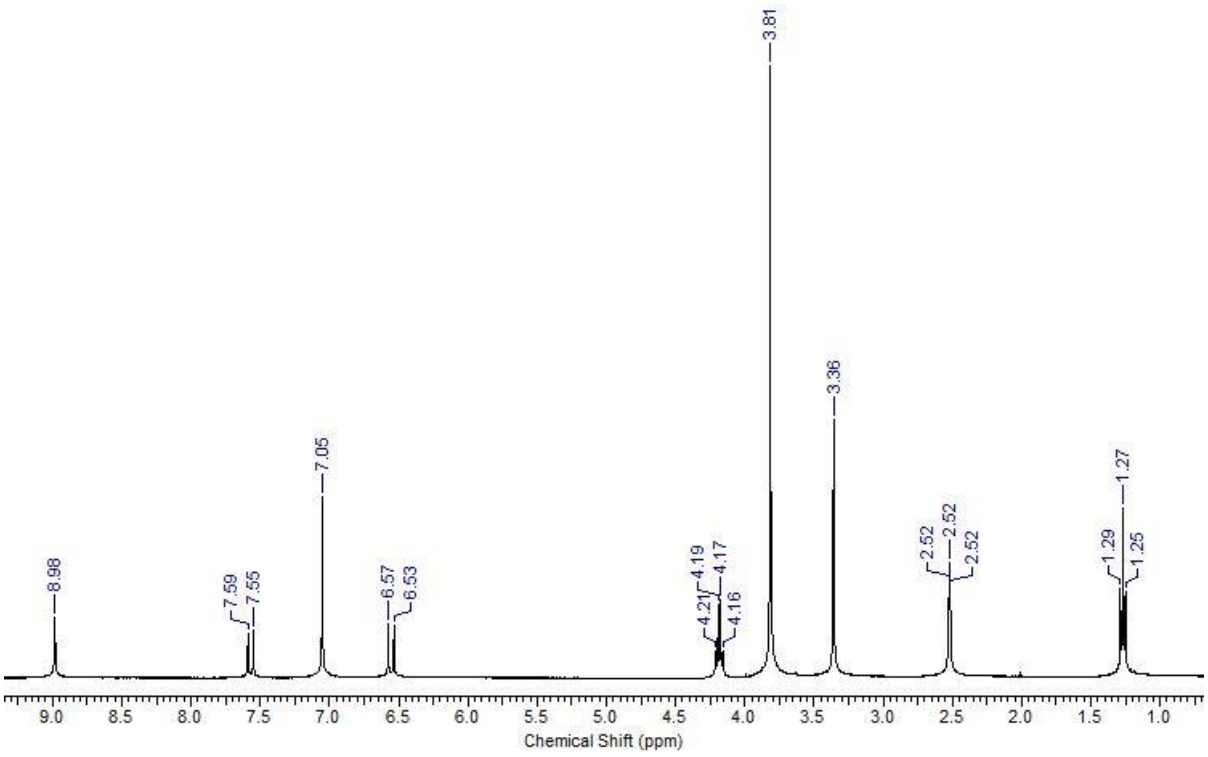

Figure 3.3: *1H NMR spectrum of ethyl sinapate.*

Synthesis of *p*-coumaryl alcohol[36]: Methyl 4-hydroxycinnamate (1.85g, 10.41 mmol) in anhydrous toluene (50 ml) was reduced by dropwise addition of diisobutylaluminum hydride (DIBAL-H) (10.41 ml, 10.41 mmol) via a dropping funnel over 10 min at 0 ℃ under argon. After 1h the reaction was complete and quenched with ethanol. Water was added and the product was exhaustively extracted in ethyl acetate. The organic layer was then dried over anhydrous Na_2SO_4 and filtered and solvent was removed in vacuum. Re-crystallization from hexanes/ethyl acetate gave *p*-coumaryl alcohol (yield 50%): ^{1}H NMR ($(CD_3)_2SO$), 4.09 (d, 2H, CH_2OH), 6.13 (d, t, 1H, CH=CH), 6.43 (d, 1H, CH=CH), 6.72 (d, 2H, H2 and H6), 7.23 (d, 2H, H3 and H5) ppm; ^{13}C NMR ($(CD_3)_2SO$), 62.43 (C9), 116.06 (C3 and C5), 128.82 (C8), 128.08 (C2 and C6), 128.58 (C1), 129.37 (C7), 157.50 (C4) ppm.

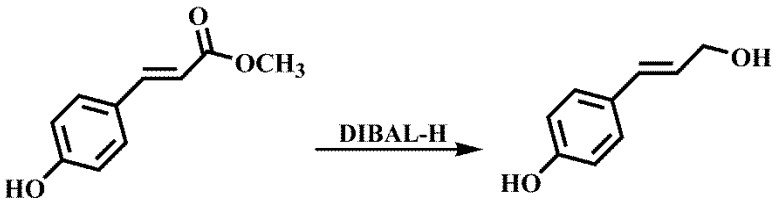

Figure 3.4: *Scheme of the synthesis of p-coumaryl alcohol.*

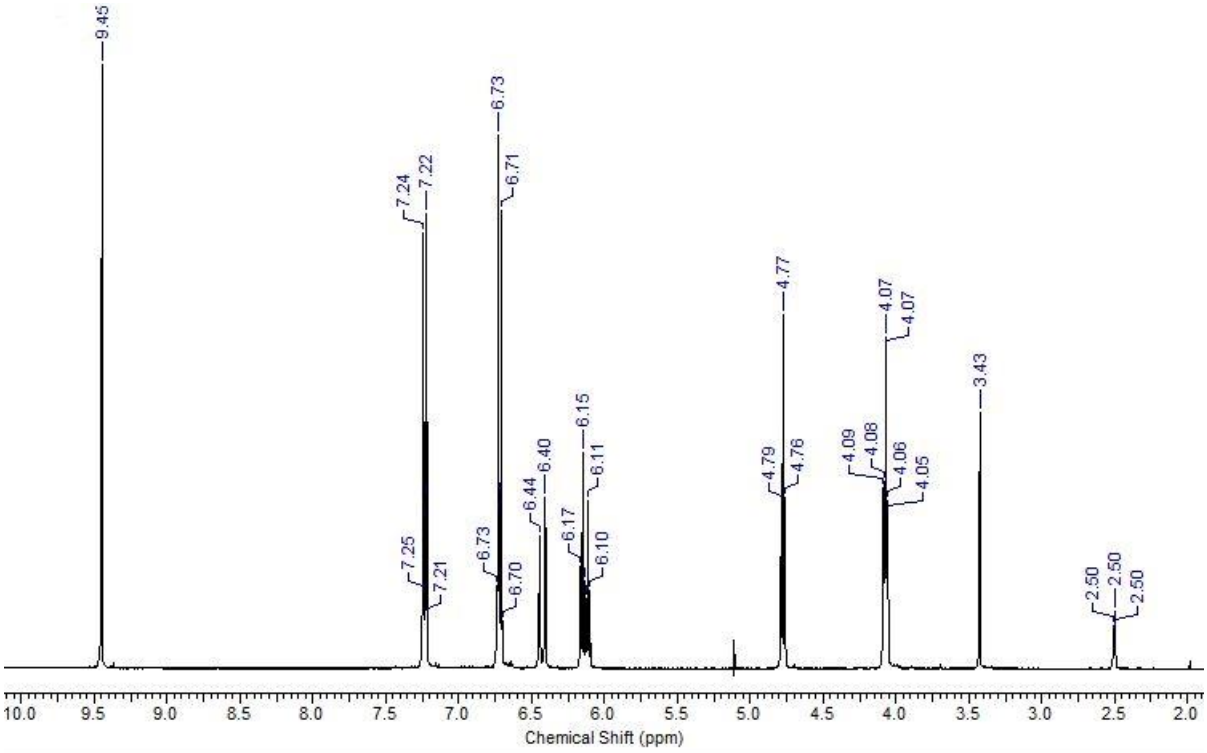

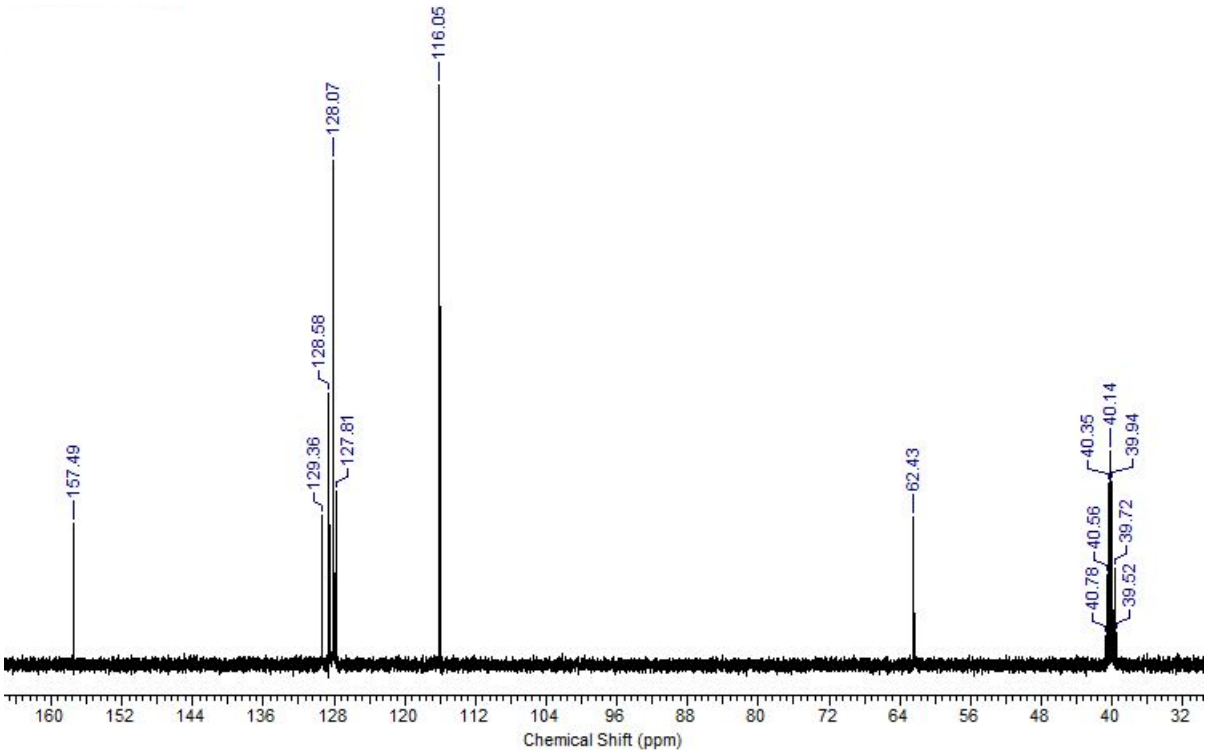

Figure 3.5: *1H and 13C NMR spectrum of p*-coumaryl alcohol.

Synthesis of *p*-coumaryl acetate[53]: *P*-coumaryl alcohol (100mg, 0.67 mmol) was dissolved in pyridine (1.6 ml) and anhydrous toluene (1.4 ml), acetic anhydride (2.67 mmol, 0.264 ml) and 4-dimethylaminopyridine (0.02 mmol, 1.8 mg) were added at room temperature. After 1h reaction, TLC showed the consumption of *p*-coumaryl alcohol. Continue reaction for another 1h and TLC showed no difference compared to the earlier one. Successively add toluene to azeotropically remove acetic anhydride and 4-dimethylaminopyridine under vacuum. The resultant oil was dissolved in ethyl acetate (10 ml) and extracted with diluted HCl (3*10 ml) and saturated NaOH (2*10 ml). The aqueous payers was back-extracted with ethyl acetate (2*10 ml). The organic layers was combined and dried over anhydrous Na_2SO_4 and filtered and solvent was removed in vacuum. The residual was then purified by silica gel column chromatography (n-hexane: ethyl acetate = 4:1 (v/v)) to give 4-acetoxycinnamyl

acetate (98 %): ^{1}H NMR ($CDCl_3$), 7.39 (d, 2H, H2 and H6), 7.05 (d, 2H, H3 and H5), 6.63 (d, 1H, Hα), 6.22 (dt, 1H, Hβ), 4.71 (dd, 1H, Hγ), 2.29 (s, 3H, OAc), 2.01 (s, 3H, OAc) ppm; ^{13}C NMR ($CDCl_3$), 170.93 (OAc), 169.51 (OAc), 150.48 (C4), 134.09 (C1), 133.24 (Cα), 127.69 (C2 and C6), 123.54 (Cβ). 121.85 (C3 and C5), 65.06 (Cγ), 21.24 (OAc), 21.10 (OAc) ppm. 4-Acetoxycinnamyl acetate (153.9 mg, 0.657 mmol) was dissolved in pyrrolidine (7.86 ml) and stirred for 10 min, then diluted with ethyl acetate (300 ml) and washed with 3% HCl (2*150 ml) and sat. NH_4Cl (2*150 ml). The organic layer was then dried over anhydrous Na_2SO_4 and concentrated in vacuum to yield an organic residue that, after purification by plate TLC, afford *p*-coumaryl acetate (29.85 %): ^{1}H NMR ($CDCl_3$), 7.32 (d, 2H, H2 and H6), 6.80 (d, 2H, H3 and H5), 6.58 (d, 1H, Hα), 6.17 (dt, 1H, Hβ), 4.71 (dd, 1H, Hγ), 2.11 (s, 3H, OAc) ppm; ^{13}C NMR ($CDCl_3$), 171.68 (OAc), 156.03 (C4), 134.39 (Cα), 128.95 (C1), 128.22 (C2 and C6), 120.63 (Cβ). 115.67 (C3 and C5), 65.76 (Cγ), 21.24 (OAc) ppm.

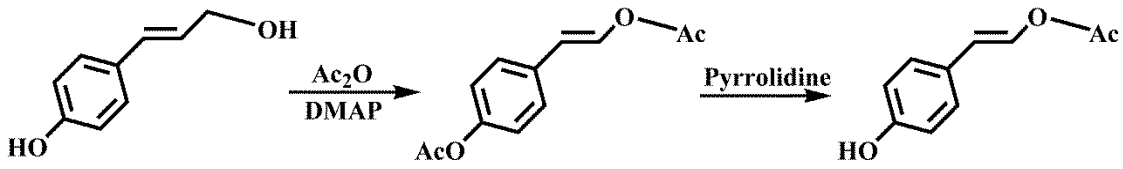

Figure 3.6: *Scheme of the synthesis of p*-coumaryl acetate.

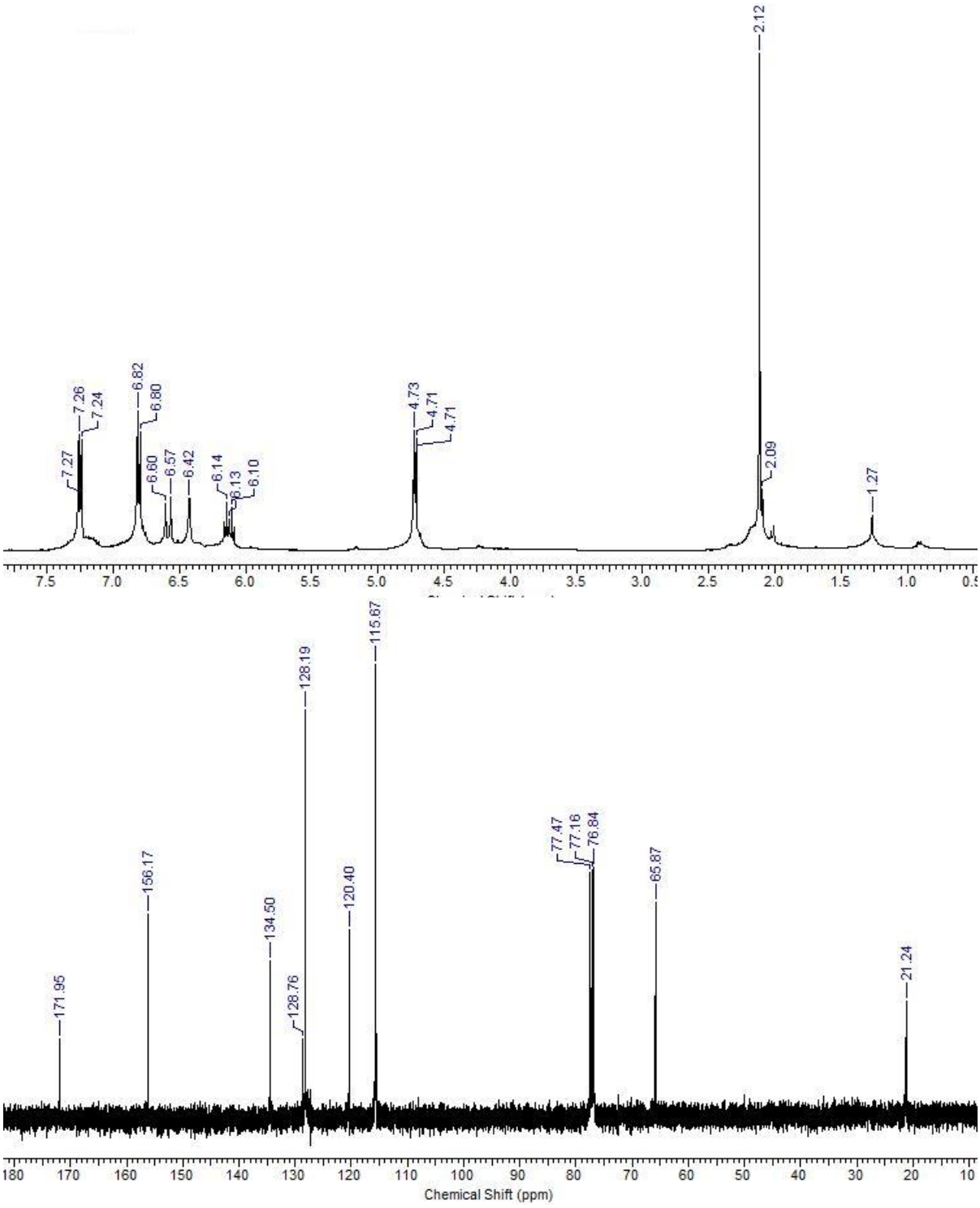

Figure 3.7: *1H and 13C NMR spectrum of p-*coumaryl acetate.

3.3 Immobilization of HRP or laccase on Affi-Gel 10

Affi-Gel 10 is an N-hydroxysuccinimide ester of a derivatized crosslinked agarose gel bead support, in aqueous solution it spontaneously couples with all ligands that have a primary amino group (Figure 3.8). We used Affi-Gel 10 as inert support for immobilization of HRP and laccase for experiments described in this Chapter and for immobilization of HRP and *β*-glucosidase described in Chapter 5.

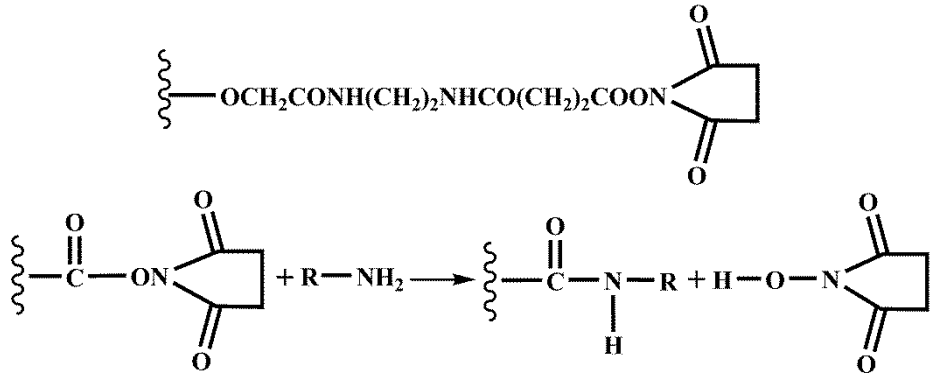

Figure 3.8: *Coupling reaction of Affi-Gel 10 with enzyme containing free amino groups.*

The immobilization of HRP or laccase on *Affi-Gel 10* was achieved following the protocol published[51]. 2 ml Affi-Gel 10 was transferred to a small buchner funnel and the gel was washed with 3 bed volumes of cold water at 4 ℃. This step was finished in 20 min to avoid the gel going dry. The moist gel cake was added to cold enzyme solution (60 mg enzyme dissolved in 3 ml MPOS buffer, pH= 7.5 for HRP and pH= 5.5 for laccase) at 4 ℃, agitated sufficiently to make a uniform suspension. The suspension was kept under gentle agitation on a shaker for 4h at 4 ℃. To block the excess of active sites of gel, 0.1 ml 1 M glycine ethyl ester (dissolved in MOPS, pH= 8.0) was added and stirred for 1 h. Gel was separated from solution, washed with phosphate buffer and stored in phosphate buffer at 4 ℃. The coupling efficiency of enzyme was estimated by comparing the concentrations of

enzyme solution prior to and after the immobilization using UV-visible spectroscopy. Coupling efficiency was determined to be 33% for HRP and 25% for laccase.

3.4 CW EPR spectroscopy and continuous-flow experiment set-up

Room temperature CW EPR measurements were conducted using Bruker ELEXSYS E500 spectrometer operating at approximately 9.5 GHz (X-band). The modulation amplitude was 0.8 G and the modulation frequency was 100 kHz. The time constant was set at 81.92 ms with a 41.09 ms conversion time and a 42.08 s sweep time. 1024 point spectra were collected at field center 3515 G over a 60 G range. The incident microwave power was 1.3 mW.

As shown in Figure 3.1, a small glass wool plug was first inserted in a quartz capillary (1.1 mm i.d. * 1.6 mm o.d.), and a suspension of immobilized enzyme (16 ul) was loaded into capillary and placed on the glass wool plug. Then the capillary was mounted with a standard EPR tube in EPR cavity and connected to continuous-flow tubing. A monolignol solution (and H_2O_2) was continuously flushed in 0.5 ml/min flow rate into capillary and through immobilized enzyme. The flushing was maintained by a programmable syringe pump from Braintree Scientific Inc. The EPR data was acquired at the region of the capillary containing immobilized enzyme, where the monolignol radical generation was predicted to occur. In control experiment, the stability of the immobilized enzymes was evaluated by monitoring the intensity of generated tyrosine radical over time by flushing the solution of tyrosine (and hydrogen peroxide). Both HRP and laccase were found very stable under standard conditions (2 mM substrate (and 1 mM H_2O_2)). Freshly prepared

immobilized enzyme was used for each test of different monolignol solutions. Sequential EPR spectra were collected for every 43s in ～40 min period for each sample, and the averaged spectrum used for simulation was obtained by post-processing depending on the lifetime of radical.

3.5 Interpretation and simulations of CW EPR spectra

For conjugated π-system such as monolignol molecule, the conjugated system as a whole is affected by the presence of an un-paired electron spin, leading to a distribution of unpaired electron spin density across over the phenol ring and side chain. EPR spectrum from small monolignol molecule in non-viscous solution falls into fast motional regime, meaning the anisotropic hyperfine tensors of radicals are averaged by rotational diffusion of the molecule. The EPR spectrum from radical in fast motional shows a distinctive pattern resulted from multiple hyperfine splittings due to interactions with protons characterized by isotropic hyperfine splitting constants (hfsc) in different magnitude.

Assuming we only have one radical species present in the solution, the general procedure to interpret the isotropic EPR spectrum is: 1) find the center point about which the positions of lines in a spectrum should be symmetric; 2) the sum of the hfcs for all nuclei must equal the separation in *Guass* between the outermost lines; 3) for equivalent protons, the number of lines is given by n+1 where n is the number of equivalent protons, second-order splitting will follow after that by the second set of protons; 4) do stick-plot reconstruction to match the experimental line positions, especially in the wings of the

spectrum; 4) for the spectrum with serious line overlap, conduct a computer simulation based on assumed hyperfine splittings and line widths.[54]

The hyperfine splitting patterns displayed by different radicals were numerically simulated to obtain an excellent agreement between the experimental and simulated EPR spectra by utilizing Ewvoigt (Alex I. Smirnov, NCSU) and PEST WinSim[45] program. For some spectra shown as a combination of a broad unresolved single line and a resolved multiple-splitting lines, the broad component was first simulated using Ewvoigt and subtracted from original spectrum, the remaining multiplet was fitted using PEST WinSim program. Convx (Alex I. Smirnov, NCSU) program was used to adjust the baseline for each experiment spectrum and determine the double integral of spectrum. Protons at different inequivalent positions are expected to have a distinct magnetic interaction with the unpaired electron and thus yield distinct hyperfine splitting constants (α_H).

3.6 Monolingol radical generation using HRP and H_2O_2

A suspension of immobilized HRP (16 ul) was loaded into a quartz capillary. 1.33 mM monolignol ester or acetate solutions and 2mM monolignol acid or alcohol solutions were prepared separately in pH=7.4 phosphate buffer and flushed with 1mM H_2O_2 through the immobilized HRP, and meanwhile, signal at the region of immobilized HRP was collected. Figure 3.9 are the photographs from three capillaries loaded with immobilized HRP after the flushing of three hydroxycinnamic acid solutions, respectively. All of the twelve monolignols are reacted with HRP/H_2O_2 and give rise to the radicals with spectra containing as a combination of a broad single line and a spectrum showing rich hyperfine-

splitting patterns. For oxidation of ferulic acid (Figure 3.13), *p*-coumaryl alcohol, coniferyl alcohol (Figure 3.15), methyl *p*-comarate, ethyl ferulate, *p*-coumaryl acetate and coniferyl acetate ((Figure 3.18), the asymmetric broad singlet is the dominant component with a weak trace of multiplets. But differently, for oxidation of *p*-coumaric acid (Figure 3.12), sinapic acid (Figure 3.14), sinapyl alcohol (Figure 3.16), ethyl sinapate (Figure 3.17) and sinapyl acetate (Figure 3.19), the sharp multiplets are strong and well resolved and amendable for simulation after subtraction of the broad component. The parameters obtained from measurement including effective g-factor and peak-to-peak line width (ΔH_{P-P}) for broad singlets and obtained from simulation including isotropic g-factor (g_{iso}) and isotropic hyperfine constants (α_H) for sharp multiplets are all summarized in Table 3.1.

In separate set of experiments, to circumvent the inference from broad singlet and obtain a clear spectrum from individual radical species, especially for the monolignols whose signal of multiplets were not well resolved, the position of capillary sitting in EPR cavity was slightly lifted so that the solution that have just passed through the immobilized HRP could be monitored. In this condition, the signals of multiplets were only obtained from sinapic acid (Figure 3.20), sinapyl alcohol (Figure 3.21) and sinapyl acetate (Figure 3.22), no EPR signal was appeared detected from other monolignols. The simulation data for sinapic acid, sinapyl alcohol and sinapyl acetate were included in Table 3.1.

3.7 Results and discussion of HRP-generated monolignol radicals

EPR spectra were observed following the one-electron oxidation of various lignin precursors. The broad unresolved singlet in spectrum appeared in the beginning and kept

growing over time, example of *p*-coumaric acid is shown in Figure 3.10. The simulation on broad singlet in spectra collected at each time point, following by double-integration to determine signal intensity, shows a linear increase of signal intensity as a function of time, which implies a linear production of radical corresponding to broad singlet. The ΔH_{P-P} for singlets at each time point were also determined and found to stay unchanged, suggesting that the same radical species is produced over time. In the solution passed through the immobilized HRP, the intensity of singlet dropped to zero, which is indicative that the radicals are either: 1) unstable and decayed into diamagnetic species or 2) actively participate in polymerization reaction and are not retained in liquid phase. Based on the above facts, the broad singlets are assigned to polymeric radicals remaining in polymeric lignin-like material upon the radical-mediated coupling of monolignols. The polymeric phase has a relatively bulky size, which tumble slowly in solution and cause the inhomogeneous broadening. They precipitate at some extent of polymerization, which is supposed to occur quickly after the coupling initiation. The polymerization cannot proceed forever, after each steps of coupling the polymeric molecules are quenched and need for further oxidation, however, their molecule size do not allow the ease of orientation towards the active center of enzyme. At the moment the polymeric radicals precipitate from solution, their structure extension is almost terminated, the solid-state polymeric radicals are accumulated at the region of immobilized HRP. In contrast to polymeric radicals, the signal intensity and line shape of well-resolved multiplets stayed unchanged, indicating a steady-state concentration in the solution. The plot of signal intensity vs. time of polymeric radical and monolignol radical for *p*-coumaric acid are shown in Figure 3.11. The slope corresponding to the rate of

accumulation of each polymeric radical from corresponding monolignol is summarized in Table 3.1 and Figure 3.23.

The α_H for monolignol radicals are appropriately assigned to protons based on the procedures mentioned above and information found in the literature. The value of α_H at one proton varies with the substitution by electron-donating group as it perturbs the electron density distribution through inductive effects. The protons at chemically equivalent positions are viewed magnetically equivalent based on the resolution scale in our experiment, so their corresponding α_H are assigned to equal values. The value of α_H of *p*-coumaric acid, sinapic acid and sinapyl alcohol measured in our experiment almost agree with the parameters obtained from the corresponding radicals generated through oxidation by ammonium cerium (IV) nitrate in highly acidic condition[36]. The minor difference could be related to the origin of different oxidant, deprotonation at different pH, polarity of the solvent used, etc. Ethyl acetate radical generated from the oxidation by ammonium cerium (IV) nitrate[55] and ethyl sinapate radical generated from the oxidation by galvinoxyl[56] are found to have unpaired electron density located on ring methoxyl groups, however, we do not observe such α_H in our experiment.

Compared to zero- and mono-methoxyl substituted monolignols, the ones with two substituent methoxyl groups on C3 and C5 positions produced the highest stationary state concentration of free monolignol radicals, and have the highest monolignol radical: polymeric radical ratio. The steric effect allows the existence of free monolignol radicals from sinapic acid, sinapyl alcohol and sinapyl acetate in solution underneath the immobilized HRP. Umeo Takahama reported rate of monolignol oxidation by HRP[21b], which was decreased in the order *p*-coumaric acid > ferulic acid > sinapic acid and coniferyl alcohol >

sinapyl alcohol. Therefore, it is reasonable to postulate that the ease of oxidation and difficulty for radical coupling is decided by the electron-donating nature and steric effect of methoxyl substituents, respectively.

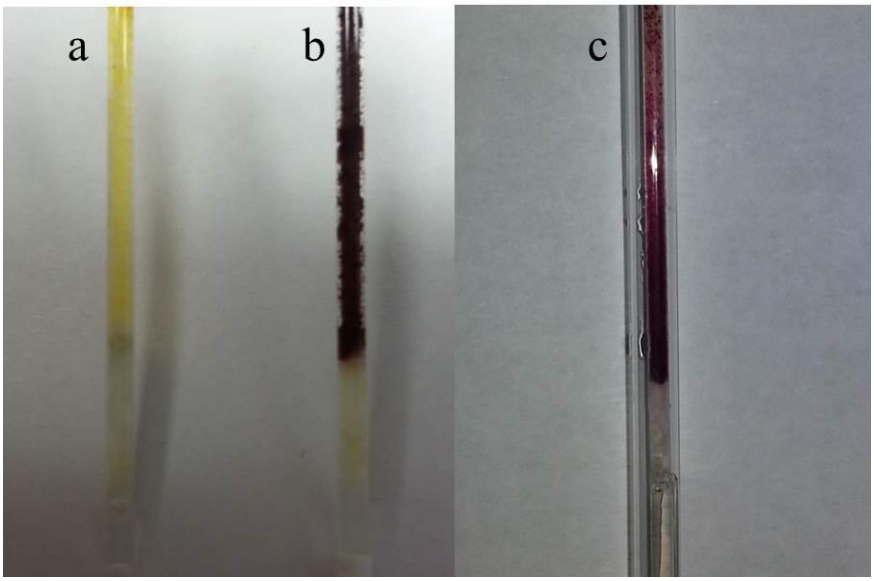

Figure 3.9: *Three photographs taken from the capillaries loaded with immobilized HRP after the flushing of three monolignol acid solutions, respectively. (a) p-Coumaric acid. (b) Ferulic acid. (c) Sinapic acid.*

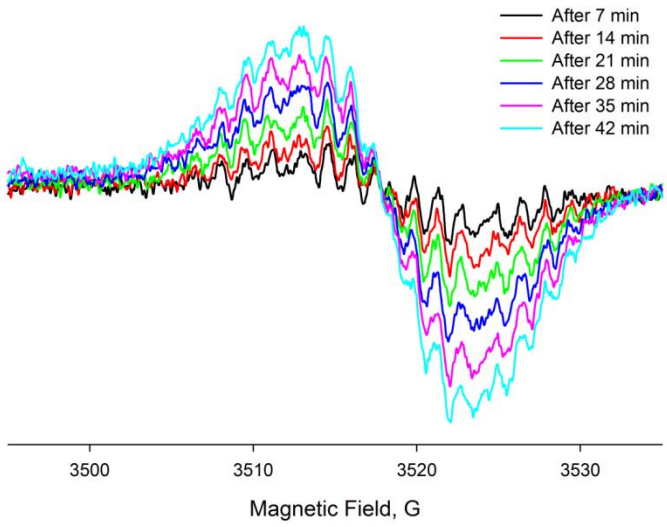

Figure 3.10: *Room temperature CW sequential EPR spectra detected from the region of immobilized HRP during the flushing with p-coumaric acid solution and H_2O_2.*

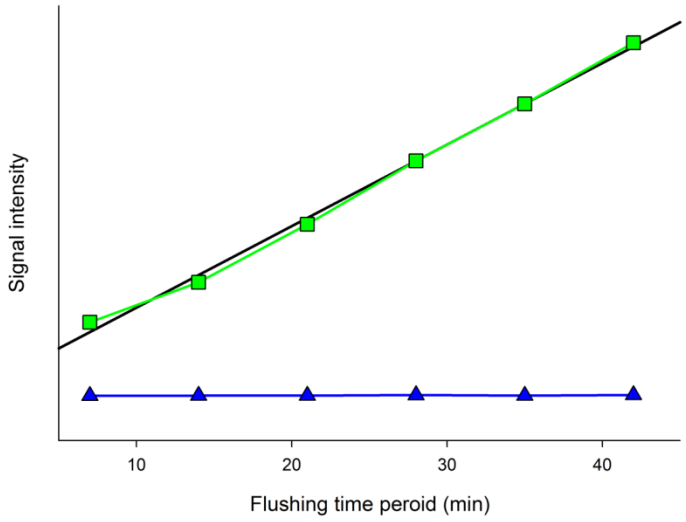

Figure 3.11: *Production of polymeric and monomer radicals during flushing of p-coumaric acid solution and H_2O_2 through immobilized HRP. Measured as double integrated intensity of the corresponding EPR signals as a function of time. (Green) Polymeric radical generation vs. time. (Black) Trendline of green curve giving the slope corresponding to the rate of polymeric radical accumulation. (Blue) Double integrated intensity of the p-coumaric acid radical in solution vs. time.*

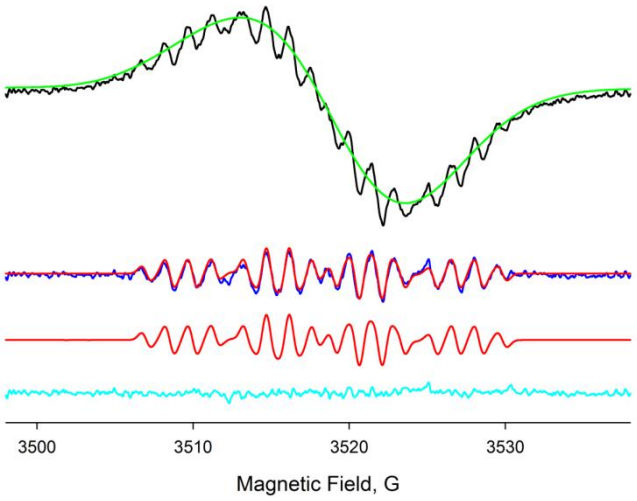

Figure 3.12: *Room temperature CW EPR signal detected from the region of immobilized HRP while flushing of p-coumaric acid solution and H_2O_2 and the corresponding simulations. (Black) Experiment spectrum. (Green) Simulated spectrum of polymeric radical. (Blue) Spectrum of free p-coumaric acid radical obtained from the overall spectrum by subtraction of the simulated broad component. (Red) Simulated spectrum of free p-coumaric acid radical. (Cyan) Residual of the fit.*

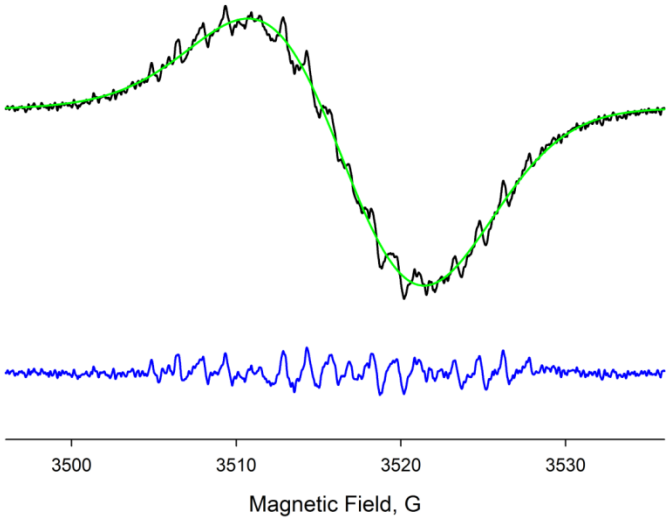

Figure 3.13: *Room temperature CW EPR signal detected from the region of immobilized HRP while flushing of ferulic acid solution and H_2O_2 and the corresponding simulations. (Black) Experiment spectrum. (Green) Simulated spectrum of polymeric radical. (Blue) Spectrum of free ferulic acid radical obtained from the overall spectrum by subtraction of the simulated broad component.*

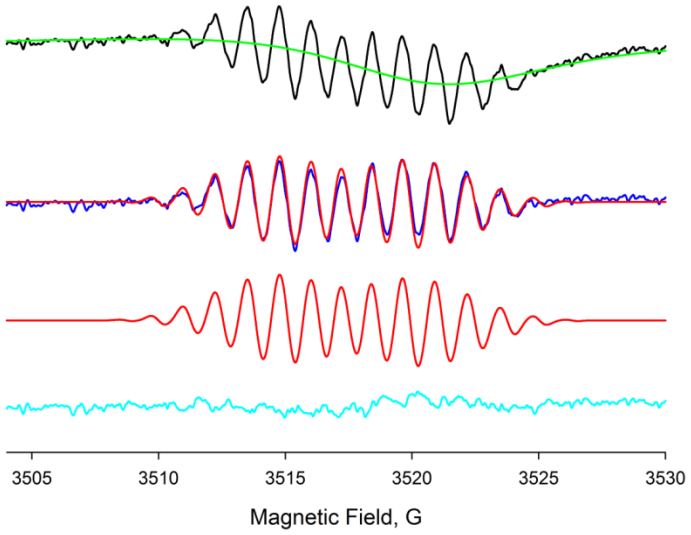

Figure 3.14: *Room temperature CW EPR signal detected from the region of immobilized HRP while flushing of sinapic acid solution and H_2O_2 and the corresponding simulations. (Black) Experiment spectrum. (Green) Simulated spectrum of polymeric radical. (Blue) Spectrum of free sinapic acid radical obtained from the overall spectrum by subtraction of the simulated broad component. (Red) Simulated spectrum of free sinapic acid radical. (Cyan) Residual of the fit.*

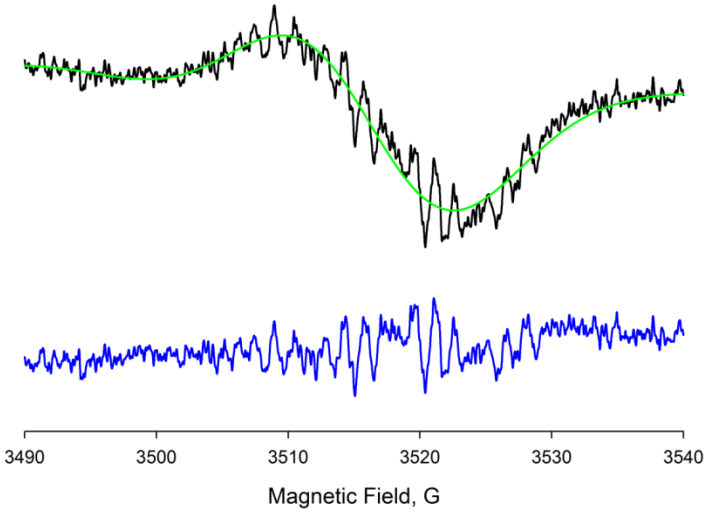

Figure 3.15: *Room temperature CW EPR signal detected from the region of immobilized HRP while flushing of coniferyl alcohol solution and H_2O_2 and the corresponding simulations. (Black) Experiment spectrum. (Green) Simulated spectrum of polymeric radical. (Blue) Experimental Spectrum of free coniferyl alcohol radical obtained from the overall spectrum by subtraction of the simulated broad component.*

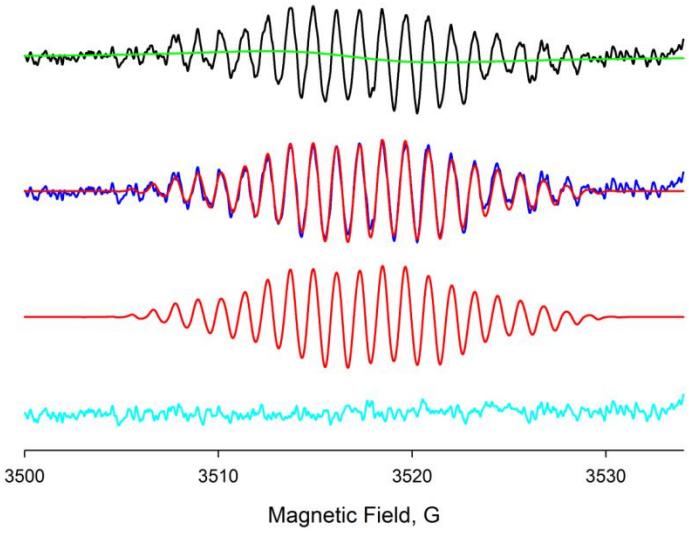

Figure 3.16: *Room temperature CW EPR signal detected from the region of immobilized HRP while flushing of sinapyl alcohol solution and H_2O_2 and the corresponding simulations. (Black) Experiment spectrum. (Green) Simulated spectrum of polymeric radical. (Blue) Spectrum of free sinapyl alcohol radical obtained from the overall spectrum by subtraction of the simulated broad component. (Red) Simulated spectrum of free sinapyl alcohol radical. (Cyan) Residual of the fit.*

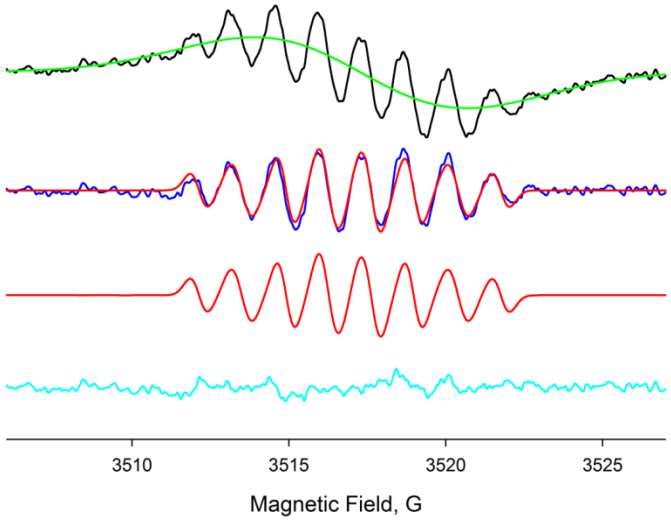

Figure 3.17: *Room temperature CW EPR signal detected from the region of immobilized HRP while flushing of ethyl sinapate solution and H_2O_2 and the corresponding simulations. (Black) Experiment spectrum. (Green) Simulated spectrum of polymeric radical. (Blue) Spectrum of free ethyl sinapate radical obtained from the overall spectrum by subtraction of the simulated broad component. (Red) Simulated spectrum of free ethyl sinapate radical. (Cyan) Residual of the fit.*

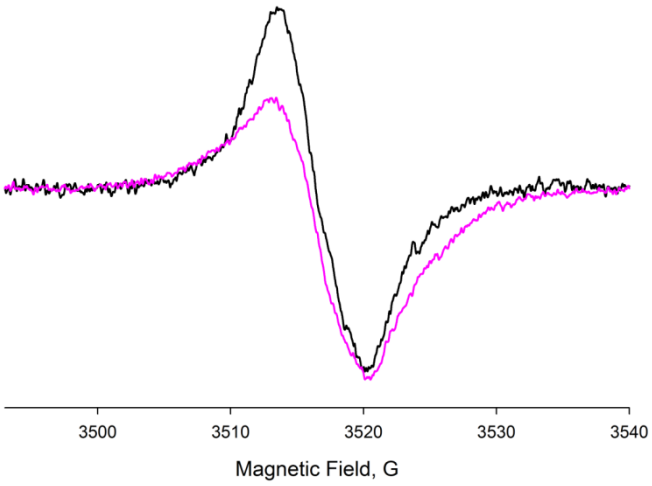

Figure 3.18: *Room temperature CW EPR spectrum detected from the region of immobilized HRP while flushing p-coumaryl acetate (Pink) or coniferyl acetate solution (Black) and* H_2O_2.

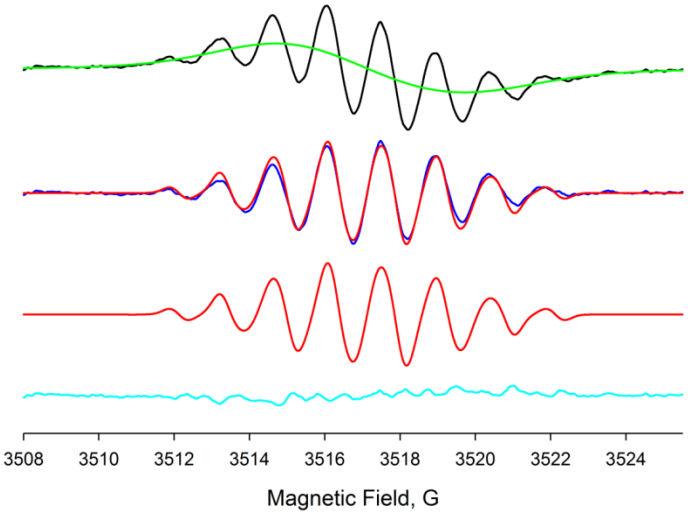

Figure 3.19: *Room temperature CW EPR signal detected from the region of immobilized HRP while flushing of sinapyl acetate solution and* H_2O_2 *and the corresponding simulations. (Black) Experiment spectrum. (Green) Simulated spectrum of polymeric radical. (Blue) Spectrum of free sinapyl acetate radical obtained from the overall spectrum by subtraction of the simulated broad component. (Red) Simulated spectrum of free sinapyl acetate radical. (Cyan) Residual of the fit.*

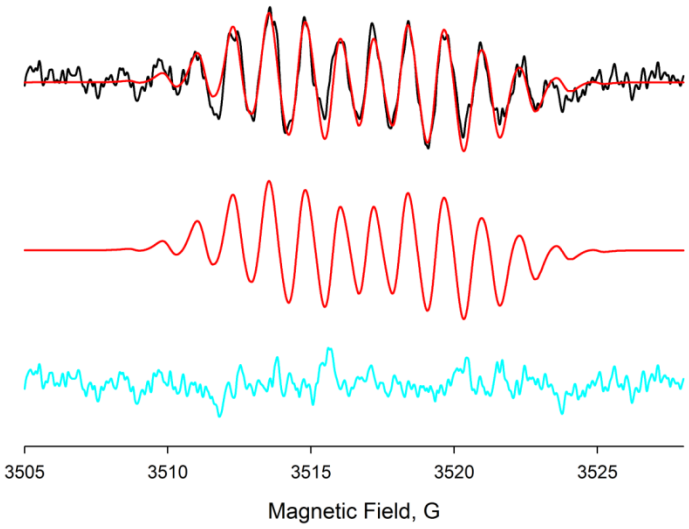

Figure 3.20: *Room temperature CW EPR signal detected underneath the region of immobilized HRP while flushing of sinapic acid solution and H_2O_2 and the corresponding simulations. (Black) Experiment spectrum. (Red) Simulated spectrum of free sinapic acid radical. (Cyan) Residual of the fit.*

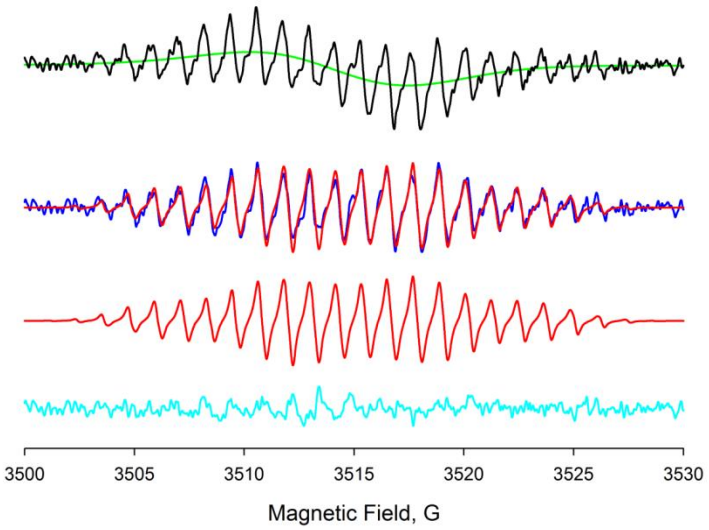

Figure 3.21: *Room temperature CW EPR signal detected underneath the region of immobilized HRP while flushing of sinapyl alcohol solution and H_2O_2 and the corresponding simulations. (Black) Experiment spectrum. (Green) Simulated spectrum of polymeric radical. (Blue) Spectrum of free sinapyl alcohol radical obtained from the overall spectrum by subtraction of the simulated broad component. (Red) Simulated spectrum of free sinapyl alcohol radical. (Cyan) Residual of the fit.*

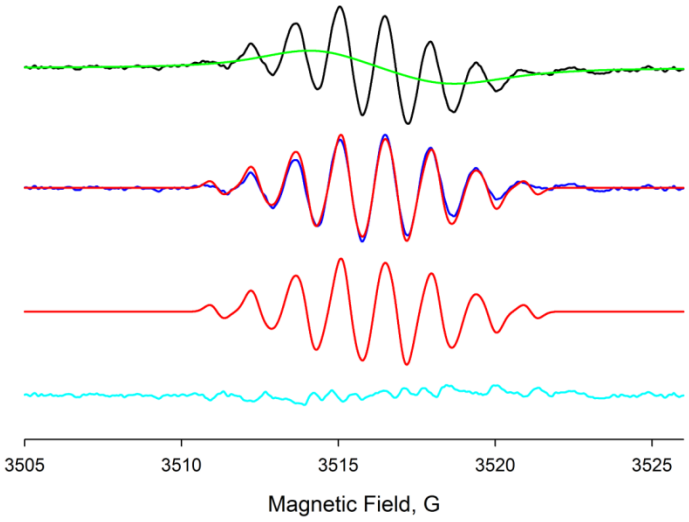

Figure 3.22: *Room temperature CW EPR signal detected underneath the region of immobilized HRP while the flushing of sinapyl acetate solution and H_2O_2 and the corresponding simulations. (Black) Experiment spectrum. (Green) Simulated spectrum of polymeric radical. (Blue) Spectrum of free sinapyl acetate radical obtained from the overall spectrum by subtraction of the simulated broad component. (Red) Simulated spectrum of free sinapyl acetate radical. (Cyan) Residual of the fit.*

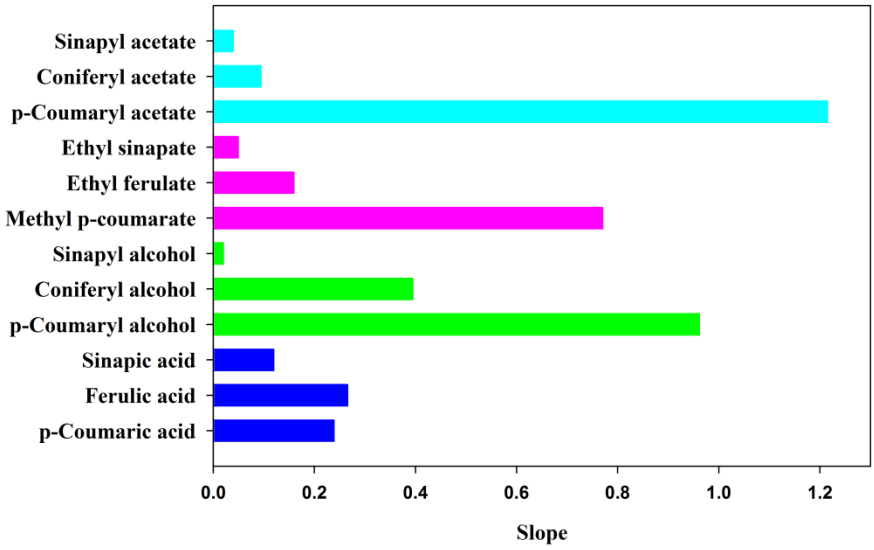

Figure 3.23: *Rate of radical accumulation in polymer phase generated from the coupling of HRP-generated monolignol radicals. (Blue) Three hydroxycinnamic acids. (Green) Three hydroxycinnamyl alcohols. (Pink) Three hydroxycinnamates. (Cyan) Three hydroxycinnamyl acetates.*

Table 3.1: *Room temperature EPR hyperfine splitting constants* (α_H, G) *and* g*-factors for HRP-generated monolignol radicals and effective* g*-factors, peak-to-peak width* $(\Delta H_{P-P}, G)$ *and linear production of corresponding polymeric radicals.*

Monolignol	**Free monolignol radical**									**Polymeric radical**		
	$\alpha_{H(2)}$	$\alpha_{H(3)}$	$\alpha_{H(5)}$	$\alpha_{H(6)}$	$\alpha_{H(\alpha)}$	$\alpha_{H(\beta)}$	$\alpha_{H(\gamma)}$	$\alpha_{H(OMe_3)}$	g_{iso}	**Effective** g	$\triangle H_{p-p}$	**Slope**
***p*-Coumaric acid**	1.51	5.22	5.22	1.51	2.89	6.39			2.0037	2.0032	10.44	0.24
Ferulic acid										2.0041	10.86	0.27
Sinapic acid	1.07			1.07	2.66	4.79		1.36	2.0037	2.0029	11.68	0.12
Sinapic acid (underneath HRP)	1.01			1.01	2.58	4.77		1.31	2.0037			
***p*-Coumaryl alcohol**										2.0031	11.96	0.96
Coniferyl alcohol										2.0033	12.95	0.39
Sinapyl alcohol	1.14			1.14	1.46	5.88	4.74	1.15	2.0038	2.0054	12.00	0.02
Sinapyl alcohol (underneath HRP)	1.12			1.12	1.46	5.88	4.73	1.15	2.0038			
Methyl *p*-coumarate										2.0031	12.54	0.77
Ethyl ferulate										2.0030	13.14	0.16
Ethyl sinapate	1.37			1.37	2.82	4.05			2.0042	2.0044	6.55	0.05
***p*-Coumaryl acetate**										2.0041	7.04	1.22
Coniferyl acetate										2.0047	7.13	0.09
Sinapyl acetate	1.30			1.30	1.26	2.91	1.63		2.0044	2.0048	5.25	0.04
Sinapyl acetate (underneath HRP)	1.28			1.28	1.27	2.83	1.60		2.0044			

3.8 Monolignol radical generation using laccase

A suspension of immobilized laccase (16 ul) was loaded into a quartz capillary. 1.33mM monolignol ester or acetate solutions and 2mM monolignol acid or alcohol solutions were separately prepared in pH=5.5 phosphate buffer and flushed through the immobilized laccase. For oxidation of ferulic acid (Figure 3.24), sinapic acid (Figure 3.25), coniferyl alcohol (Figure 3.27), sinapyl alcohol (Figure 3.28), ethyl sinapate (Figure 3.29), coniferyl acetate (Figure 3.30) and sinapyl acetate (Figure 3.31), their EPR spectra are all presented as a broad unresolved single line and a sharp multiple-splitting lines, of which the broad component is simulated first and subtracted, leaving the sharp multiplets for individual simulation. The parameters obtained from measurement including effective g-factor and peak-to-peak line width (ΔH_{P-P}) for broad singlets and obtained from simulation including isotropic g-factor (g_{iso}) and isotropic hyperfine constants (α_H) for sharp multiplets are all summarized in Table 3.2. Interestingly, the spectra intensity of ethyl sinapate and sinapyl acetate increased as a function of time, however, for others the signal stayed unchanged. The spectrum of oxidation of *p*-coumaryl alcohol only shows a set of sharp lines. However, no radical was detected from the oxidation of *p*-coumaric acid, methyl *p*-comarate, ethyl ferulate, *p*-coumaryl acetate and coniferyl acetate.

3.9 Results and discussion of laccase-generated monolignol radicals

All of the EPR spectra obtained from the laccase-catalyzed oxidation of monolignols present the signal in scale weaker than those catalyzed by HRP. We suppose there are two reasons. First, the ability of enzyme to catalyze one-electron oxidation of phenol derivatives is related to its redox potential[25a]. Laccase with lower redox potential is known to be less active than HRP. Second, the molecule size of laccase, especially when immobilized, may create the steric issues that affect the specificity of laccase towards substrate. It is interesting to note that for monolignols with relative good aqueous solubility, such as ferulic acid, sinapic acid, coniferyl alcohol and sinapyl alcohol, the unresolved single lines are unchanged in magnitude, implying a stable stationary concentration of radicals maintained in active range. According to their g-factors and ΔH_{P-P}, they are safely assigned to polymeric radicals. Given the small ΔH_{P-P} and overall low radical concentration compared to the case in HRP, we believe that the polymeric radicals are created with low degree of polymerization, so they are likely to be removed from the active range with the flushing of solution. In contrast, the increasing signals appeared for the polymeric radicals from ethyl sinapate and sinapyl acetate imply the molecule precipitation and accumulation as occurred in HRP. For oxidation of *p*-coumaryl alcohol (Figure 3.26), the polymerization is expected to occur as other monolignols, however, the absence of polymeric radical signal may give a clue that the polymer-based molecule is possibly created in linear mode so it has no complex structure to secure the active unpaired site. The reason for the absence of signal of *p*-coumaric acid is not quite clear but the rate of oxidation by fungal laccase was previously

studied and reported in the order of sinapic acid > ferulic acid ≥ *p*-coumaric acid[21b]. The absence of signal for other esters and acetates might be related to the low solubility of the monolignols, which could be greatly improved by the method proposed in Chapter 4. The isotropic α_H corresponding to monolignol radicals are carefully assigned, and they are found to be consistent to the ones obtained in the experiment of HRP and the ones obtained by oxidation of ammonium cerium (IV) nitrate and galvinoxyl. However, same as HRP, the α_H from ring methoxyl groups for ethyl sinapate and sinapyl acetate were not observed in here. Comparison among the monolignol radicals with different methoxyl substitution reveals that the ease of oxidation is highly controlled by the nature of the electron-donating methoxyl substituents.

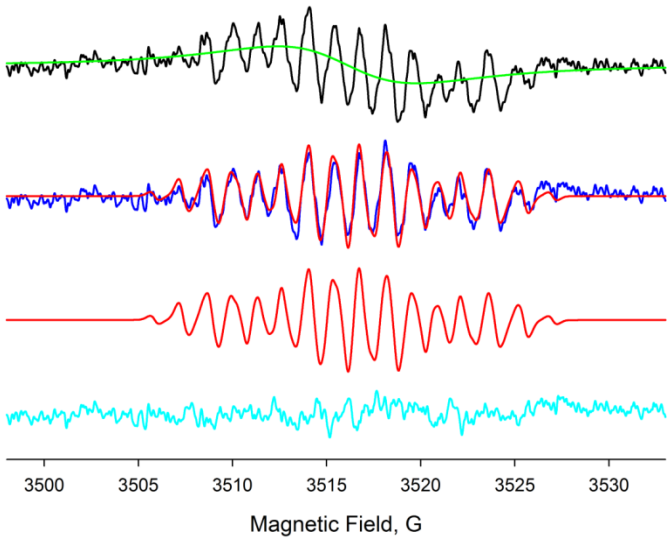

Figure 3.24: *Room temperature CW EPR signal detected at the region of immobilized laccase while flushing of ferulic acid solution and corresponding simulations. (Black) Experiment spectrum. (Green) Simulated spectrum of polymeric radical. (Blue) Spectrum of free ferulic acid radical obtained from the overall spectrum by subtraction of the simulated broad component. (Red) Simulated spectrum of free ferulic acid radical. (Cyan) Residual of the fit.*

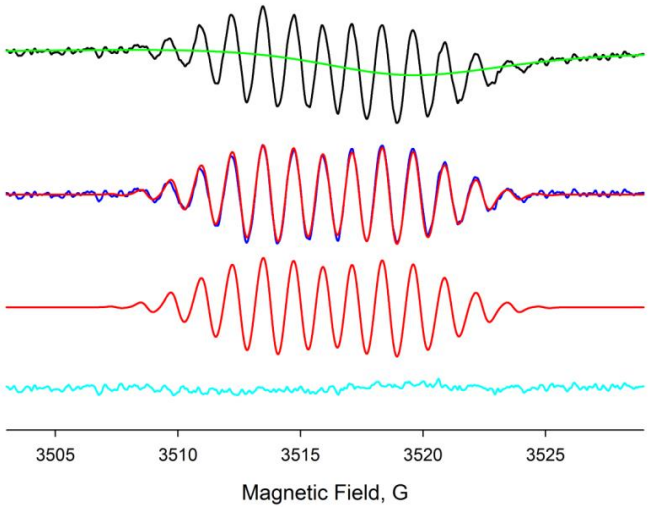

Figure 3.25: *Room temperature CW EPR signal detected at the region of immobilized laccase while flushing of sinapic acid solution and corresponding simulations. (Black) Experiment spectrum. (Green) Simulated spectrum of polymeric radical. (Blue) Spectrum of free sinapic acid radical obtained from the overall spectrum by subtraction of the simulated broad component. (Red) Simulated spectrum of free sinapic acid radical. (Cyan) Residual of the fit.*

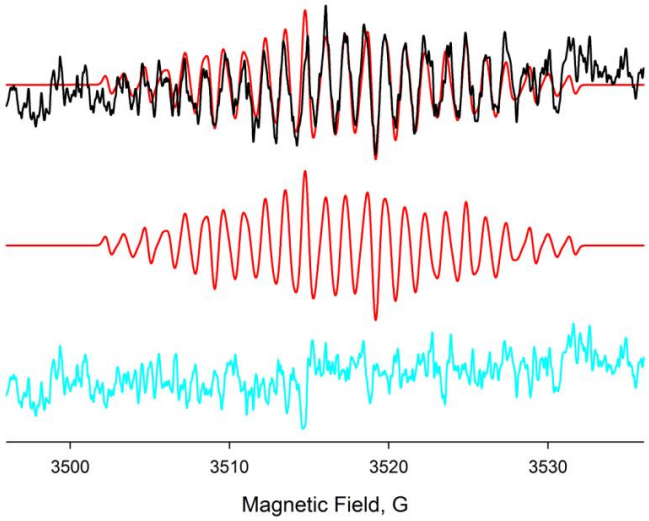

Figure 3.26: *Room temperature CW EPR signal detected at the region of immobilized laccase while flushing of p-coumaryl alcohol solution and corresponding simulations. (Black) Experiment spectrum. (Red) Simulated spectrum of free p-coumaryl alcohol radical. (Cyan) Residual of the fit.*

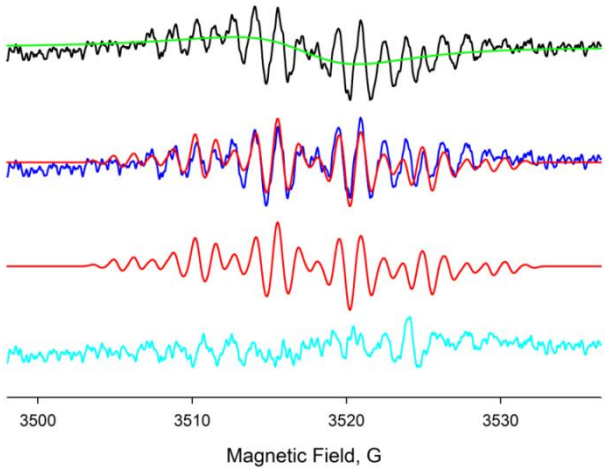

Figure 3.27: *Room temperature CW EPR signal detected at the region of immobilized laccase while flushing of coniferyl alcohol solution and corresponding simulations. (Black) Experiment spectrum. (Green) Simulated spectrum of polymeric radical. (Blue) Spectrum of free coniferyl alcohol radical obtained from the overall spectrum by subtraction of the simulated broad component. (Red) Simulated spectrum of free coniferyl alcohol radical. (Cyan) Residual of the fit.*

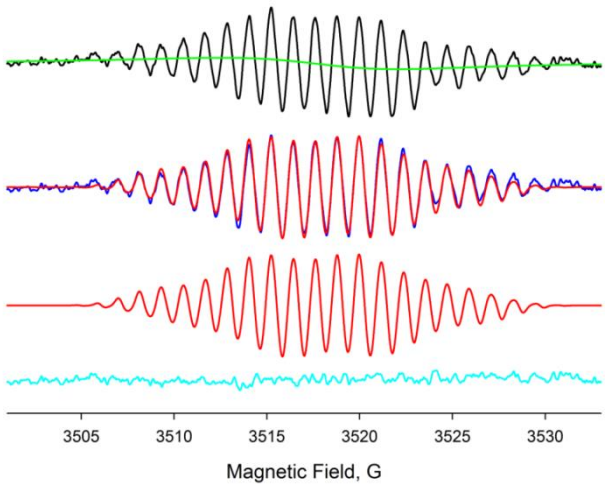

Figure 3.28: *Room temperature CW EPR signal detected at the region of immobilized laccase while flushing of sinapyl alcohol solution and corresponding simulations. (Black) Experiment spectrum. (Green) Simulated spectrum of polymeric radical. (Blue) Spectrum of free sinapyl alcohol radical obtained from the overall spectrum by subtraction of the simulated broad component. (Red) Simulated spectrum of free sinapyl alcohol radical. (Cyan) Residual of the fit.*

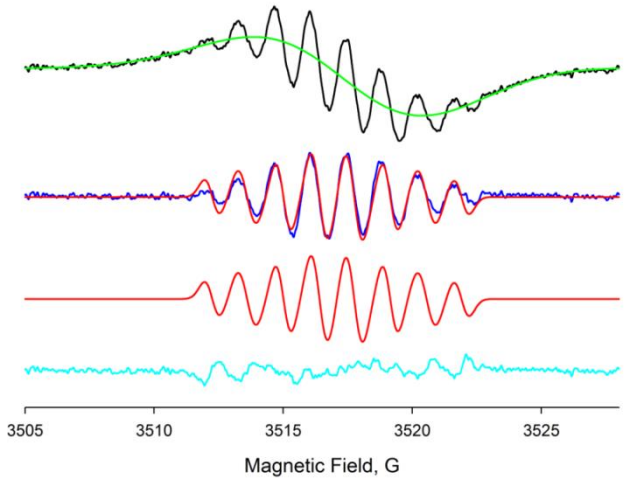

Figure 3.29: *Room temperature CW EPR signal detected at the region of immobilized laccase while flushing of ethyl sinapate solution and corresponding simulations. (Black) Experiment spectrum. (Green) Simulated spectrum of polymeric radical. (Blue) Spectrum of free ethyl sinapate radical obtained from the overall spectrum by subtraction of the simulated broad component. (Red) Simulated spectrum of free ethyl sinapate radical. (Cyan) Residual of the fit.*

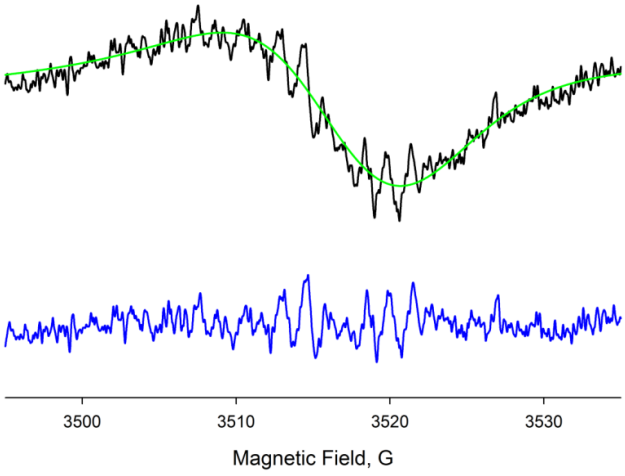

Figure 3.30: *Room temperature CW EPR signal detected at the region of immobilized laccase while flushing of coniferyl acetate solution and corresponding simulations. (Black) Experiment spectrum. (Green) Simulated spectrum of polymeric radical. (Blue) Spectrum of free coniferyl acetate radical obtained from the overall spectrum by subtraction of the simulated broad component.*

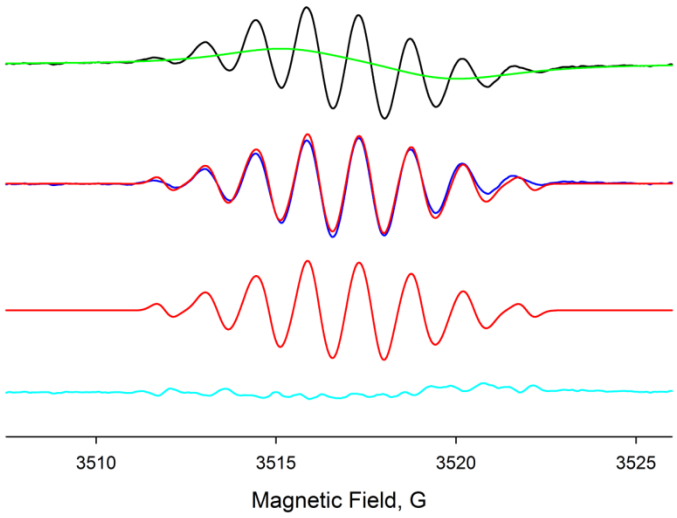

Figure 3.31: *Room temperature CW EPR signal detected at the region of immobilized laccase while flushing of sinapyl acetate solution and corresponding simulations. (Black) Experiment spectrum. (Green) Simulated spectrum of polymeric radical. (Blue) Spectrum of free sinapyl acetate radical obtained from the overall spectrum by subtraction of the simulated broad component. (Red) Simulated spectrum of free sinapyl acetate radical. (Cyan) Residual of the fit.*

Table 3.2: *Room temperature EPR hyperfine splitting constants* (α_H, G) *and* g*-factor for laccase-generated monolignol radicals and effective* g *-factors, peak-to-peak width* $(\Delta H_{P-P}, G)$ *of corresponding polymeric radicals.*

Monolignol	**Free monolignol radical**									**Polymeric radical**	
	$\alpha_{H(2)}$	$\alpha_{H(3)}$	$\alpha_{H(5)}$	$\alpha_{H(6)}$	$\alpha_{H(\alpha)}$	$\alpha_{H(\beta)}$	$\alpha_{H(\gamma)}$	$\alpha_{H(OMe_3}$	g	g	ΔH_{p-p}
Ferulic acid	1.48		5.35	1.76	2.60	5.34		1.51	2.0038	2.0049	7.45
Sinapic acid	1.04			1.04	2.64	4.79		1.30	2.0037	2.0038	9.90
***p*-Coumaryl alcohol**	1.25	5.05	5.05	1.25	2.46	6.06	4.00		2.0037		
Coniferyl alcohol	1.33		5.35	1.89	2.31	5.39	3.89	1.39	2.0038	2.0040	7.11
Sinapyl alcohol	1.12			1.12	1.43	5.95	4.74	1.12	2.0038	2.0046	9.85
Ethyl sinapate	1.38			1.38	2.84	4.01			2.0042	2.0043	6.50
Sinapyl acetate	1.33			1.33	1.19	2.88	1.64		2.0044	2.0049	4.72

3.10 Probe unpaired electron density from isotropic hyperfine parameters

The conjugate system of monolignol is affected by the presence of an unpaired electron spin, leading to a spin density distribution which can be probed through the hyperfine splitting of protons at 2, 6- and 3, 5- positions, methylene and methine at side chain and substituent methoxyl group. The hyperfine splitting constant to a proton is proportional to the density of the unpaired electron on the carbon adjacent to that proton. The McConnell

equation[43] is used for the calculation of spin density from hyperfine parameters for α-protons,

$$\alpha_{\alpha-H}{}^{H} = Q_{CH}{}^{H}\rho_{C}{}^{\pi} \quad (3.1)$$

where ρ is the spin density of carbon to which the proton is bonded. Q is a proportionality constant which varies in range of 20-30 *G*, but in this case the value of 22.5 *G* was used[36].

Hyperfine interactions of γ-methylene protons which are not directly bound to the conjugate system are explained by hyperconjugation mechanism that *1s* orbital of γ-proton is overlapped with $2p_z$ orbital of Cβ for electron transfer therefore the spin density at the nucleus of the γ-proton depends on the dihedral angle θ between the $2p_z$ and the plane containing eight-carbon skeleton. To calculate the spin density for β-methylene, the Mclachlan formula is used[43, 57],

$$\alpha_{\beta-H}{}^{H} = (B_0 + B_1 cos^2\theta)\rho_c{}^{\pi} \quad (3.2)$$

Where B_0 is a constant approximately equal to zero. Referred to β-methylene in tyrosine radical, the value of B_1 and θ in solution are taken as 58 *G* and 60 °[58].

For free rotating methyl group on C3 and C5, a simplified Mclachlan equation is used,

$$\alpha_{ME}{}^{H} = (B_1/2)\rho_{C}{}^{\pi} \quad (3.3)$$

According to above equations, the absolute value of spin density distribution for three hydroxycinnamic acids and three hydroxycinnamyl alcohols are calculated. Previous studies conducted by Russell et al[36] distinguished the positive and negative spin densities of phenylpropanoid radicals using computational methods. Therefore, the calculated unpaired

electron spin density at carbon nuclei of EPR-active positions and the density on EPR-silent positions are shown in Table 3.3. In fact, The Q and B_1 are approximate values and equations have their own limitations therefore the calculated spin density are only regarded to an order of magnitude, however, for comparison among the compounds differing in their degree of substitution the summation overall presents a general trend that each monolignol follows in their series.

Table 3.3: *Unpaired electron spin density at carbon nuclei and EPR-silent positions of hydroxycinnamic acid and hydroxycinnamyl alcohol radicals calculated from CW fast-motion EPR spectra using the McConnell and Mclachlan equations.*

	$C_{(2)}$	$C_{(3)}$	$C_{(5)}$	$C_{(6)}$	$C_{(\alpha)}$	$C_{(\beta)}$	$C_{(\gamma)}$	$C_{(OMe_3)}$	$S_{(Others)}$
***p*-Coumaric acid**	-0.07	0.23	0.23	-0.07	-0.13	0.28			0.53
Ferulic acid	-0.07		0.24	-0.08	-0.12	0.24		0.05	0.64
Sinapic acid	-0.05			-0.05	-0.11	0.21		0.05	0.85
***p*-Coumaryl alcohol**	-0.06	0.22	0.22	-0.06	-0.11	0.27	-0.21		0.73
Coniferyl alcohol	-0.06		0.24	-0.08	-0.10	0.24	-0.20	0.05	0.81
Sinapyl alcohol	-0.05			-0.05	-0.06	0.26	-0.21	0.04	0.87

3.11 Conclusions

We studied the radicals generated from enzyme-catalyzed oxidation of twelve monolignols using a combination of continuous-flow and enzyme surface immobilization method. Eight monolignol radicals were enzymatically generated HRP/H_2O_2 and laccase.

The structures of monolignol radicals were assigned based on the magnitudes of the hyperfine splitting constants deduced from the simulation of EPR spectra. Structures of monolignol radicals were shown to be identical no matter what enzyme was used. The methoxyl substitutents on phenol ring play a key role on the ease of oxidation of monolignol by enzyme, and selectivity of radical coupling due to steric effect and unpaired electron spin density perturbation that electron density is induced to spectroscopically blind positions (except phenolic oxygen).

The amount of polymerized radicals formed as a result of HRP-catalyzed dehydrogenation of monolignols increase linearly with time. As a rule, the polymerized radicals were formed and accumulated at highest rate from unsubstituted monolignols and slowest rate from 3,5-dimethoxy-substituted monolignols. Based on effective g-factors and peak-to-peak linewidth (ΔH_{P-P}), the polymerized radicals formed from coupling of monolignol radicals were found to have different structures depending on what enzyme was used for monolignol radical generation. The data of effective g-factors and ΔH_{P-P} could be used as a reference to identify the structure of polymeric radicals obtained from monolignols by different methods and paramagnetic species in natural lignin.

CHAPTER 4

Hyperfine Sublevel Correlation (HYSCORE) Spectroscopy Study on Model Monolignol Radicals

4.1 Introduction

In the case of monolignol radicals, the unpaired electron is delocalized over the phenol ring and side chain, therefore, we preliminary determined the spin density distribution through the isotropic component of the hyperfine couplings of the 2,6-, 3,5- protons, α, β type-methane and γ-type methylene protons for total eight monolignol compounds. The isotropic component is the result of rapid rotational reorientation of spins in liquid at room temperature. To obtain the anisotropic component of electron-nuclear hyperfine tensor, the sample is prepared in the frozen solution, however, the hyperfine couplings are masked in CW EPR spectrum due to inhomogeneous line broadening. Thus, the pulsed EPR spectroscopy method, especially two-dimensional (2D) Hyperfine Sublevel Correlation (HYSCORE) Spectroscopy, immensely useful for identifying weak anisotropic hyperfine interactions and disentangling complicated overlapping spectra, is utilized in our work. In brief, HYSCORE is a 2D four-pulse sequence electron spin echo envelope modulation (ESEEM) technique in which the intensity of an electron spin echo is modulated by the transition frequencies of interacting nuclear spins [59]. Recently, a six-pulse HYSCORE sequence with enhanced sensitivity was proposed, however addition of two pulses increased

effect of pulse imperfections on the HYSCORE spectrum[60] . A paramagnetic system with an interacting electron spin (s=1/2) and a magnetic nucleus of spin I=1/2 create two allowed EPR transitions ($\Delta m_s = \pm 1$ and $\Delta m_I = \pm 0$), two forbidden EPR transitions ($\Delta m_s = \pm 1$ and $\Delta m_I = \pm 1$) and two nuclear transitions ($\Delta m_s = \pm 0$ and $\Delta m_I = \pm 1$), as shown in Figure 4.1, in which α, β refer to the two $m_s = \pm 1/2$ electron spin manifolds respectively. In ESEEM, the microwave pulses can excite both the allowed and the forbidden EPR transitions, and the nuclear transition frequencies manifest themselves as modulation of the electron spin echo[40]. HYSCORE significantly improves the resolution by separating overlapping nuclear frequencies in two dimensions. This is particularly important if more than one magnetic nucleus is interacting with the unpaired electron spin.

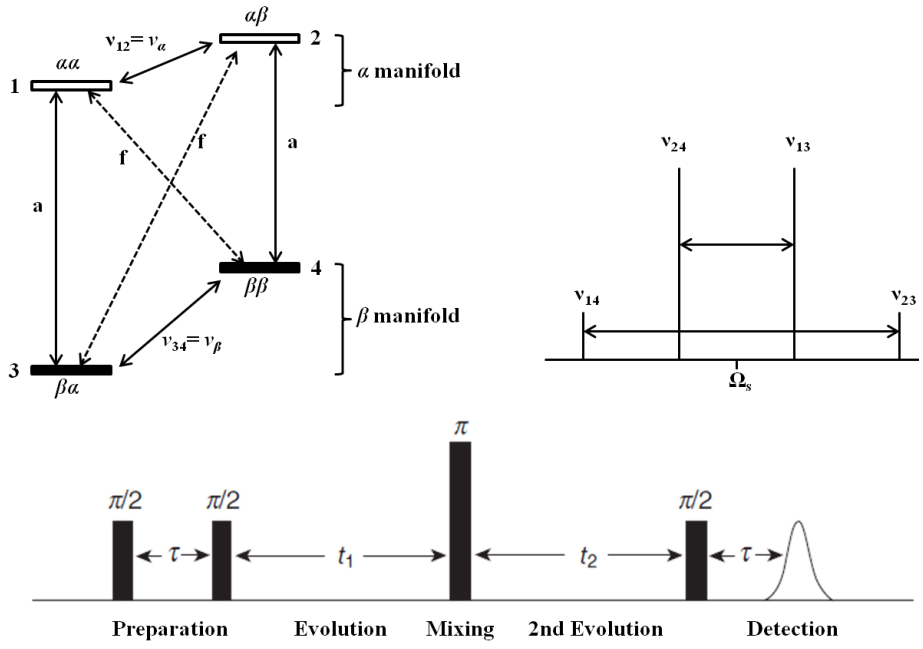

Figure 4.1: *For $s = 1/2, I = 1/2$ system with weak coupling, the energy level diagram showing two allowed, two forbidden EPR transitions and two nuclear transitions (top left). The corresponding schematic EPR spectrum (top right). Four-pulse sequence of HYSCORE (bottom)[40].*

The commonly used 2D HYSCORE experiment involves four-pulse sequences and corresponding four time periods, as shown in Figure 4.2. All the coherences corresponding to the electron α- and β- spin manifolds are generated during the first two $\pi/2$ pulses separated by an interval τ, and then evolve during the period t_1. The following π pulse interchanges the electron spin α and β, transforming the coherences associated with α spin to that of β spin, and *vice versa*. After the second evolution period t_2, a $\pi/2$ pulse is applied which creates the stimulated echo after a period τ. Spin echo amplitude is monitored as a function of pulse separation time periods t_1 in one dimension and t_2 in a second dimension. With the 2D FT of the detected time-domain signal, a 2D correlation map is obtained in which peaks along the diagonal are the coherences undisturbed by pulses while the off-diagonal cross peaks that symmetrically disposed on each side of the diagonal with coordinates (ν_α, ν_β) and (ν_β, ν_α) are indicative of the magnetic coherence transfer between spin α and β[61].

The three principal components of a hyperfine tensor are commonly presented as $(A_x, A_y, A_z) = (A_{iso} - T - \delta, A_{iso} - T + \delta, A_{iso} + 2T)$, where A_{iso}, T, and δ stand for the isotropic, dipolar and rhombic component, respectively. So obviously,

$$A_{iso} = \frac{1}{3}[A_x + A_y + A_z] \tag{4.1}$$

The nuclear transition frequencies ν_α and ν_β for one I=1/2 nucleus is presented[62],

$$\nu^2{}_{\alpha(\beta)} = [\nu^2{}_{z\alpha(\beta)} cos^2\Theta + \nu^2{}_{y\alpha(\beta)} sin^2\Theta sin^2\varphi + \nu^2{}_{x\alpha(\beta)} sin^2\Theta sin^2\varphi] \tag{4.2}$$

Where

$$\upsilon_{x\alpha(\beta)} = -\nu_I \pm \frac{A_{iso}-T+\delta}{2} \quad (4.3)$$

$$\upsilon_{y\alpha(\beta)} = -\nu_I \pm \frac{A_{iso}-T-\delta}{2} \quad (4.4)$$

$$\upsilon_{z\alpha(\beta)} = -\nu_I \pm \frac{A_{iso}+2T}{2} \quad (4.5)$$

Polar angles – θ, φ refer to the magnetic field direction to the principle axis system of the hyperfine tensor. In the case of an axial symmetry, δ=0, the hyperfine tensor is simplified as $(A_x, A_y, A_z) = (A_{iso} - T, A_{iso} - T, A_{iso} + 2T)$ in which $A_x = A_y = A_\perp, A_z = A_\parallel$. In this case, the hyperfine tensor is determined by two components, $A_\perp$, where the direction of magnetic field is perpendicular to the symmetry axis, and $A_\parallel$, where the direction of magnetic field is parallel to the symmetry axis. The equations at above become,

$$\nu^2{}_{\alpha(\beta)} = [\nu^2{}_{\parallel\alpha(\beta)} - \nu^2{}_{\perp\alpha(\beta)}]cos^2\theta + \nu^2{}_{\perp\alpha(\beta)} \quad (4.6)$$

$$\nu^2{}_{\parallel\alpha(\beta)} = -\nu_I \pm (A_{iso} + 2T)/2 \quad (4.7)$$

$$\nu^2{}_{\perp\alpha(\beta)} = -\nu_I \pm (A_{iso} - T)/2 \quad (4.8)$$

After rearrangement,

$$\nu^2{}_{\alpha(\beta)} = \nu^2{}_{\beta(\alpha)} Q_{\alpha(\beta)} + G_{\alpha(\beta)} \quad (4.9)$$

Where

$$Q_{\alpha(\beta)} = \frac{2A_{iso}+T \mp 4\nu_I}{2A_{iso}+T \pm 4\nu_I} \quad (4.10)$$

And

$$G_{\alpha(\beta)} = \pm 2\nu_I \frac{4\nu^2{}_I - A^2{}_{iso} + 2T^2 - A_{iso}T}{2A_{iso} + T \pm 4\nu_I} \quad (4.11)$$

Dikanov and co-workers suggested a way of plotting in squared-frequency coordinates to simplify the 2D HYSCORE data[62]. In such way, the frequency-squared coordinates of the points are measured at the middle of a ridge corresponding to the highest signal intensity along the direction of the ridges, to give a straight line segment with the slope and intercept representing $Q_{\alpha(\beta)}$ and $G_{\alpha(\beta)}$, respectively. Then hyperfine components T and A_{iso} can be calculated in the transformed expressions,

$$T = \pm\sqrt{\frac{16}{9(1-Q_{\alpha(\beta)})}\left[G_{\alpha(\beta)} + \frac{4\nu_I{}^2 Q_{\alpha(\beta)}}{1-Q_{\alpha(\beta)}}\right]} \quad (4.12)$$

$$A_{iso} = \pm 2\nu_I \frac{1+Q_{\alpha(\beta)}}{1-Q_{\alpha(\beta)}} - \frac{T}{2} \quad (4.13)$$

4.2 Preparation of UV-induced monolignol radical

A 2mM monolignol solution was prepared in 12.5 mM borate buffer, pH=11.15. 150 µl monolignol solution was loaded in EPR tube, degassed by bubbling argon and frozen in liquid nitrogen. The sample was kept in cold-finger dewar filled with liquid nitrogen and illuminated with the full spectrum of a 300-watt Xe lamp at 150 W for 5 min (~3 cm distance between cold-finger dewar and Xe lamp), and then the EPR tube was turned 180 ° and illuminated for an another 5 min to result in an average monolignol radical concentration of approximately 27 µM. CW EPR spectra were acquired on a Varian E-102 spectrometer operating at 9.5 GHz (X-Band) and digitized to 2048 data points per spectrum. EPR

Experiments at 77K were performed with a cold-finger Dewar filled with liquid nitrogen. Spectrometer settings were as follows: microwave power 2 mW, scan range of 200 G, field modulation frequency 100 kHz, and amplitude 4 G.

4.3 2D HYSCORE spectroscopy

The EPR spectra were recorded on an X-band Bruker Elexsys 580 pulse spectrometer equipped with a dielectric flexline probe ER 4118-MD5. All experiments were carried out at liquid nitrogen temperatures, approximately 77 K. A six-pulse HYSCORE sequence was used with a τ delay of 136 ns and a 16 ns detector gate (centered at the maximum of the echo signal), the delays are defined as the difference in the starting point of the pulses. The echo intensity was measured as a function of t_1 and t_2, where t_1 and t_2 were incremented in steps of 24 ns from their initial values of 32 and 40 ns, respectively. The static magnetic field value was 3445 G and the microwave frequency was 9.70866 GHz. Equal amplitude pulses of 8 ns for $\pi/2$ and 16 ns for π were used to record a 256 × 256 matrix. The 8 ns time difference between the initial values of the time delays, t_1 and t_2 and $\pi/2$ and π pulses were set equal to obtain a symmetric spectrum. The echo decay was eliminated by a low-order polynomial baseline correction and tapered with a Gaussian function. Before 2D Fourier transformation, the data was zero filled to a 2048 × 2048 matrix. The spectra are presented as contour plot prepared in Matlab R2012a.

4.4 Results and discussion

According to comparison with the signal intensity of CW EPR spectrum, the signal detected by 2D HYSCORE dropped significantly due to unusually fast Tm relaxation time. Such fast relaxation could be consequence of aggregation of the radical species. By incorporating 25% (v/v) glycerol or 50% (v/v) diglyme in the borate buffer, we succeeded in generating the radical in glassy matrices, however, the CW EPR spectra of these glassy samples were severely broadened by an unidentified radicals or higher spin species. Therefore, for now, we ruled out the use of glassing agents.

As shown in Figure 4.2, CW EPR spectra of four monolignols prepared from illumination at pH 11.15 have similar spectral feature and consist of a single line. With no resolved hyperfine splitting the signal does not provide for unique fit to extract magnetic parameters and characterize the radical. . The spectra shown are intensity (double integral) normalized, from which the effective g-factor and ΔH_{P-P} were measured and are listed in Table 4.1. Three hydroxycinnamic acids, differing in methoxyl substitution, present very similar g-factor. The ΔH_{P-P} decreases in the order of *p*-coumaric acid > ferulic acid >sinapic acid, corresponding to the effect of the number of ring protons interacting with unpaired electron and contributing to the unresolved hyperfine pattern that contributes to the linewidth of the EPR signal. Thus, with two more protons at Cγ, *p*-coumaryl alcohol shows much broader line shape than hydroxycinnamic acids. The linewidth alone, however, cannot be used as an "identifier" of the radical species as it is a result of interplay between

unresolved hyperfine interactions and electronic relaxation that can be affected by many factors as temperature, presence of other radicals or paramagnetic impurities in the vicinity.

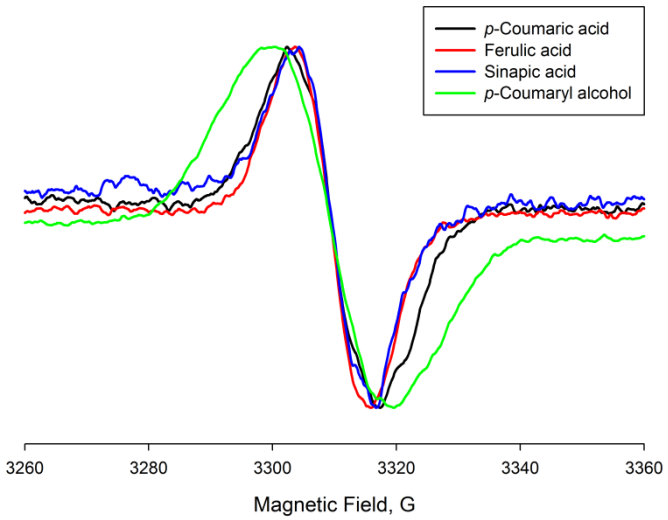

Figure 4.2: *77K normalized CW EPR spectra of four model monolignol radicals generated from UV illumination at pH 11.15.*

Table 4.1: *77k CW EPR g -factors and* ΔH_{P-P} *linewidth of radicals generated by illumination of monolignols in aqueous buffer at pH = 11.15.*

Monolignol type	g**-factor**	ΔH_{P-P}
p-Coumaric acid	2.0036	14.90
Ferulic acid	2.0034	12.18
Sinapic acid	2.0038	12.17
p-Coumaryl alcohol	2.0038	19.26

Figure 4.3 shows the echo detected field sweep spectrum of *p*-coumaric acid. Figure 4.4 shows the full HYSCORE spectrum of *p*-coumaric acid in aqueous buffer measured at

the maximum echo intensity, shown in the figure 4.3 by the arrow. In 2D HYSCORE, hyperfine interactions appear in different quadrants of the spectrum. For monolignol radical, there is no appreciable intensity of cross peaks observed in the (+,-) quadrant, making the (+,+) quadrant as the only nondegenerate quadrant of interest. All the observed non-diagonal cross-peaks in the Figure 4.4 is (+,+) quadrant of the HYSCORE spectrum are related to ^{1}H nuclei magnetically coupled to unpaired electrons, and consists of four pair of ridges, H^{I}-H^{IV}. All the proton cross-peaks are centered about the diagonal (defined by $\nu_1 = \nu_2$) and extend approximately in the direction perpendicular to the main diagonal at 14.7 MHz, which is equal to proton Zeeman frequency ($\nu_1[^1H]$). Also several artifacts are observed on the main diagonal as well as diagonal cross-peak due to very weakly interacting ^{23}Na nuclei from the buffer.

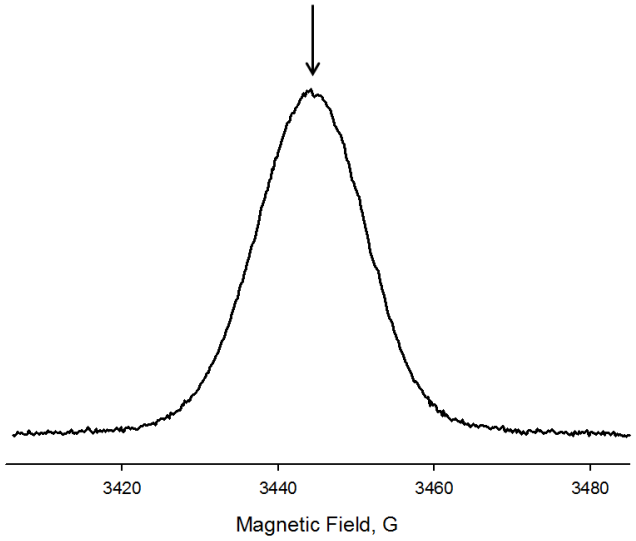

Figure 4.3: *The magnetic field sweep electron spin echo spectrum of the p-coumaric acid illuminated at pH 11.15.*

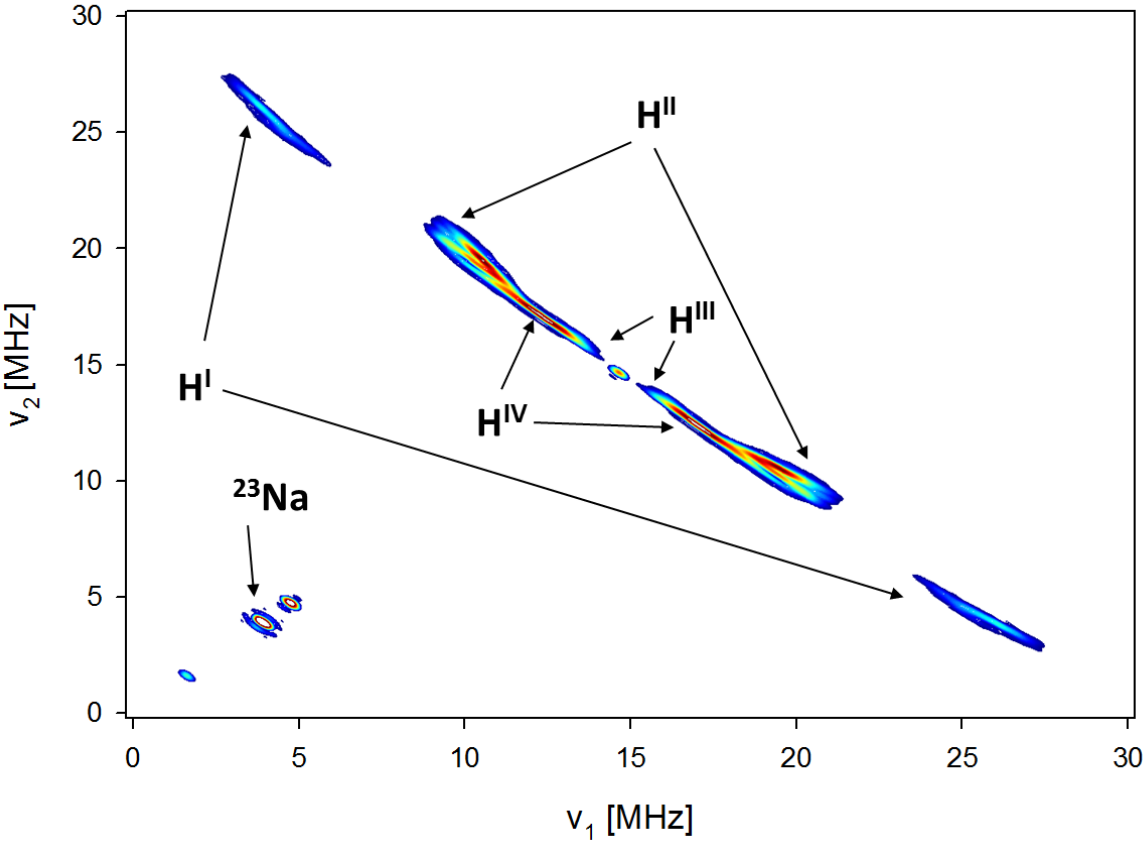

Figure 4.4: *The 2D HYSCORE spectrum obtained from the illumination on p-coumaric acid at pH 11.15.*

To obtain $Q_{\alpha(\beta)}$ and $G_{\alpha(\beta)}$, the frequency-squared coordinates were measured from the middle of the narrow-featured contours corresponding to the highest signal intensity within the proton ridges corresponding to H^{I}-H^{IV}. The measured points were fit by a straight line with good agreement (Figure 4.7), providing the values of $Q_{\alpha(\beta)}$ and $G_{\alpha(\beta)}$. Using the equations 4.12 amd 4.13 provided in the introduction section of the chapter, we obtained four sets of possible hyperfine parameters from each pair of $Q_{\alpha(\beta)}$ and $G_{\alpha(\beta)}$, where the sign of T

can be positive or negative and for a given value of T, there are two possible values of a_{iso}. The appropriate set of hyperfine values from four possibilities was selected by comparison to the literature data of tyrosine radical[63].

Figure 4.5 is a zoomed view of the spectral region of H^I ridge. Large separation of the H^I ridges (20-25 MHz) and very small shift from the anti-diagonal indicates strong hyperfine interaction which has small orientation anisotropy. It is comprised by two sub-ridges which can be clearly seen in the Figure 4.5 where H^I_1 and H^I_2 are shown as plotted in the squared-frequency coordinates. Based on the slopes and the intercepts of the fitted straight lines isotropic hyperfine couplings of 22.47 and 18.48 MHz were obtained for upper and lower sub-ridge respectively. Both of the sub-ridges correspond to a small hyperfine anisotropy 2.62 and 1.77, approximately 10 % of A_{iso}. The only protons capable of having such a combination of strong isotropic and small anisotropic couplings are β-methylene protons of π-radical[60]. The size of hyperfine couplings of these protons directly depends on the dihedral angle of the tail with respect to the plane of the π-bonds. The formation of methylene is highly likely to occur at Cα as a result of the reduction of double bond between Cα and Cβ upon illumination.

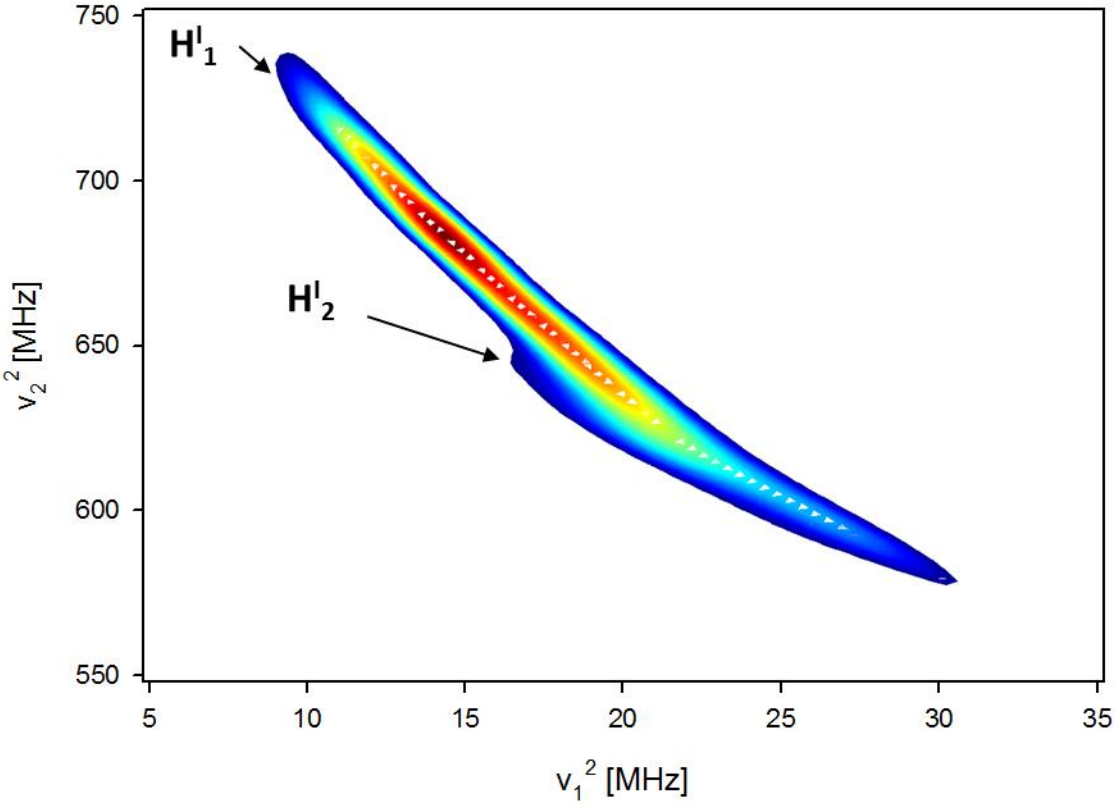

Figure 4.5: *The enlarged region of the 2D HYSCORE spectrum of p-coumaric acid illuminated at pH 11.15 in the frequency-squared coordinate system. This spectrum highlights the* ^1H *ridge* H^I.

H^{II} ridges have limited resolution, they correspond to well-defined hyperfine interaction with strong anisotropic rhombic character. Each of the H^{II} ridge consists of two partly resolved sub-ridges formed by the cross-peaks corresponding to molecular frame orientations in the *xy* and *xz* planes of the hyperfine tensor principal axis. Using linear analysis as well as comparison with data known for tyrosine radicals we calculated the

corresponding hyperfine tensors as [-5.7 -14.3 21.0] and [-5.8 -14.3 -19.3] MHz with A_{iso} as -13.7 and -13.1 MHz, respectively. H^{II} is assigned to ring protons at C3 and C5 positions.

H^{III} ridges are located in relative proximity to the main diagonal reflecting weak isotropic hyperfine component. But H^{III} shows significant shift from the main diagonal, which is caused by strong anisotropy of the hyperfine interactions. The combination of weak isotropic and strong anisotropic hyperfine components is typical for H-bonded protons. Linear analysis determines the hyperfine tensor of the H-bonded proton(s) as [3.68 5.44] MHz with $A_{iso} = 0.64$ MHz and T= 3.04 MHz.

H^{IV} ridges have small separation corresponding to hyperfine coupling less than 11 MHz. Similar to H^{I}, the H^{IV} ridges are distributed along the anti-diagonal with very small shift. Such shape of ridges is attributed by overlapping of multiple weakly interacted protons, such as ring protons at C2 and C6 and tail protons.

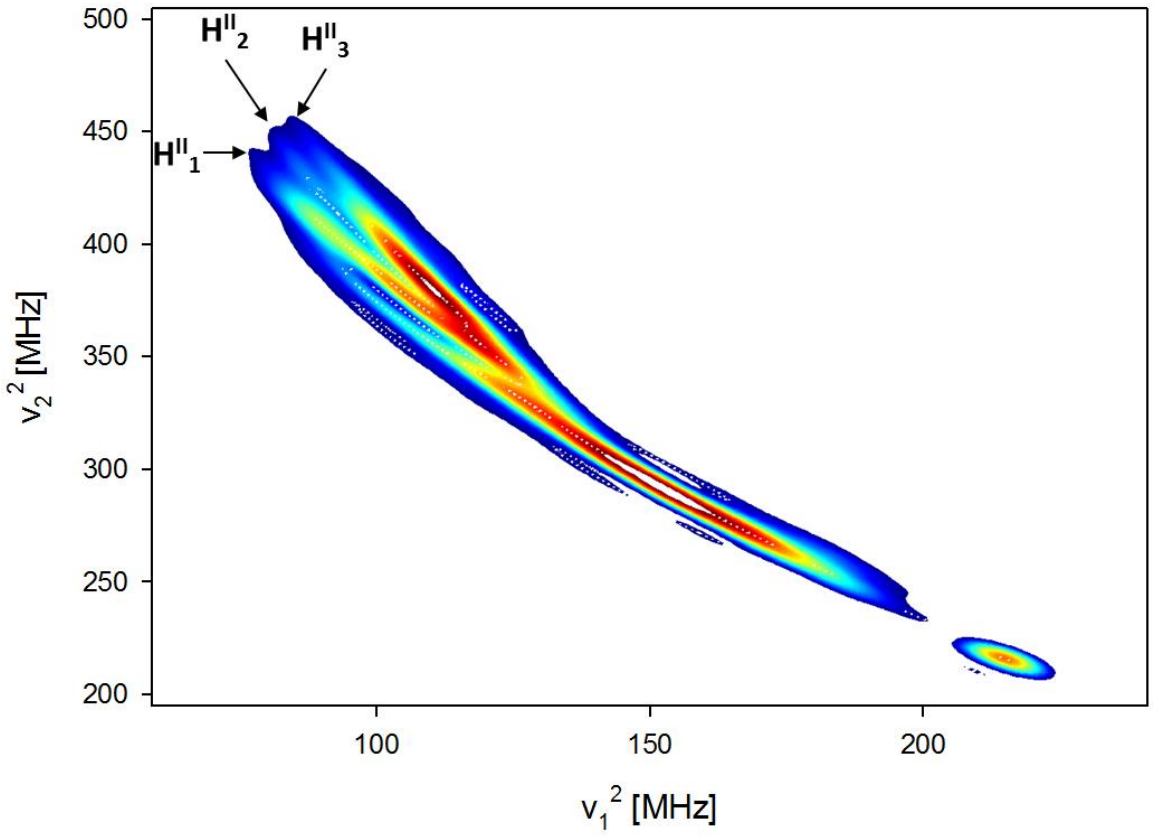

Figure 4.6: *The enlarged region of the 2D HYSCORE spectrum of p-coumaric acid illuminated at pH 11.15 in the frequency-squared coordinate system. This spectrum highlights the ^{1}H ridges H^{II}, H^{III} and H^{IV}.*

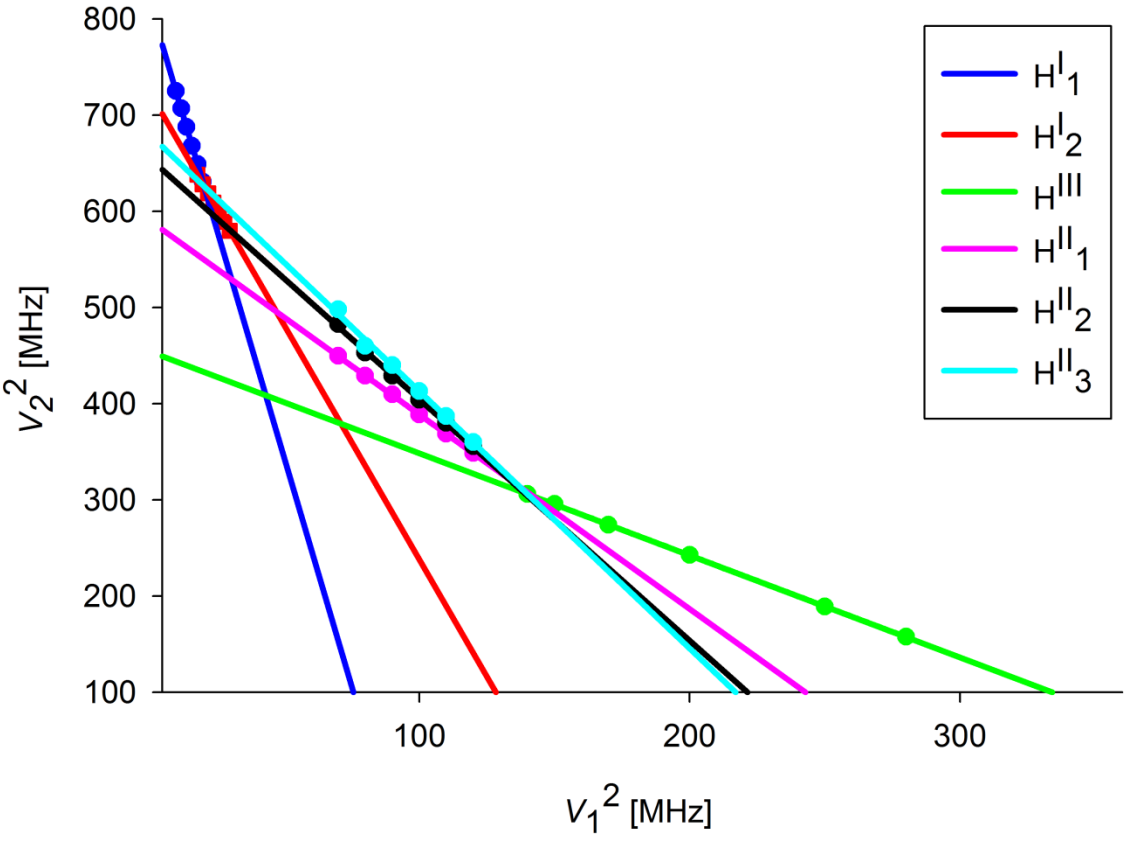

Figure 4.7: *A plot of selected points from the line shapes obtained from illumination on p-coumaric acid at pH 11.15 in the frequency-squared plot of the ^1H hyperfine couplings that are shown in Figure 3S. The straight lines indicate the linear fit of the experimental data points for the individual ^1H ridges.*

Figure 4.8 is the full HYSCORE spectrum of photogenerated radical from *p*-coumaryl alcohol in aqueous buffer. The sample aggregation is even worse than the case of *p*-coumaric acid, resulting a weaker signal and poor spectrum resolution. The spectrum is qualitatively similar to what obtained from *p*-coumaric acid, however, only H^I ridges were resolved but for others, H^I- H^{IV} could not be obtained with satisfactory resolution. H^I ridges shown in Figure 4.8 present hyperfine interaction with small anisotropy that corresponds to

β-methylene protons of π-radical. However, there is a significant difference between *p*-coumaryl alcohol and *p*-coumaric acid. *p*-Coumaric acid H^I present two well defined hyperfine coupling [19.8 27.7] and [16.7 22.03], in contrast, *p*-coumaryl alcohol H^I has long extension and strongly curved in frequency-squared coordinates (Figure 4.9), corresponding to wide distribution of the hyperfine couplings, which in term corresponds to nearly random rotation of β-methylene protons with respect to π-radical. It could indicate the reduction of the double broken between Cα and Cβ, or it could be attributed to the methylene protons at Cγ position. Unfortunately, limited resolution does not allow us to make definite conclusion with respect to the spectrum of this radical species. Techniques like freeze-quench are promising to overcome the problem of sample aggregation and will be used in further investigation.

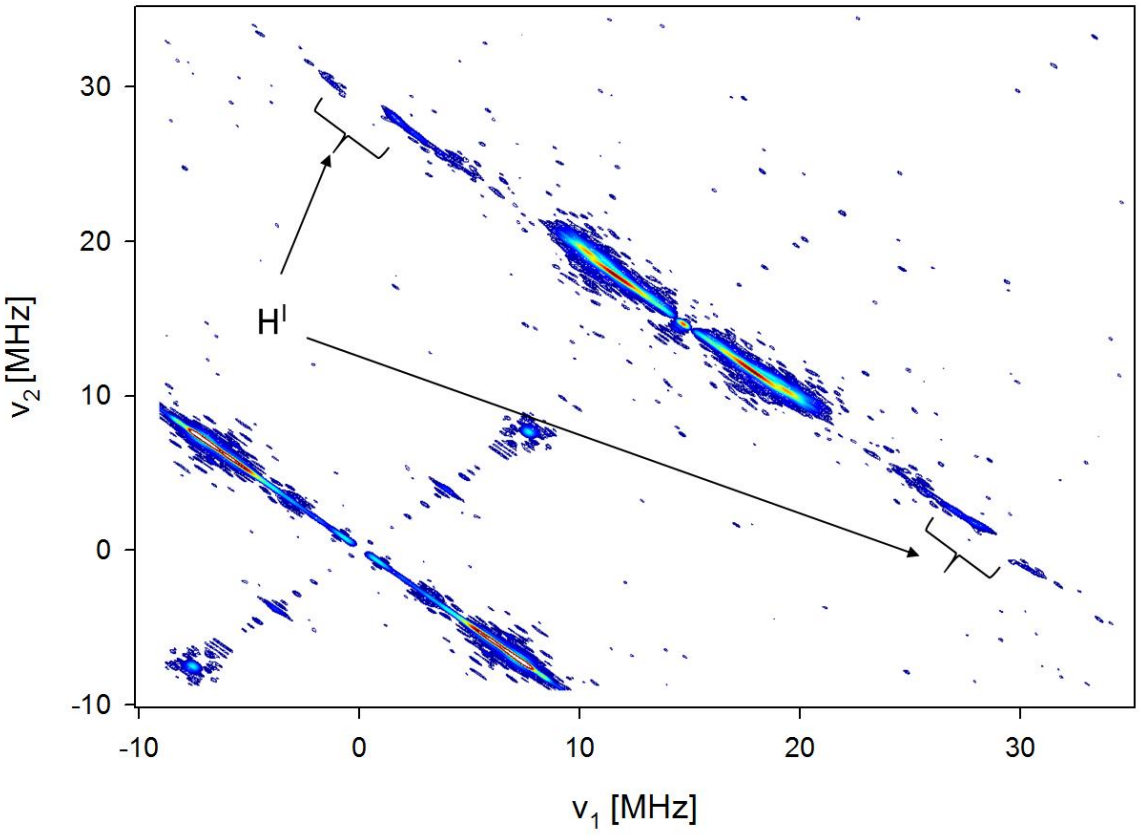

Figure 4.8: *The 2D HYSCORE spectrum obtained from the illumination on p-coumaryl alcohol at pH 11.15.*

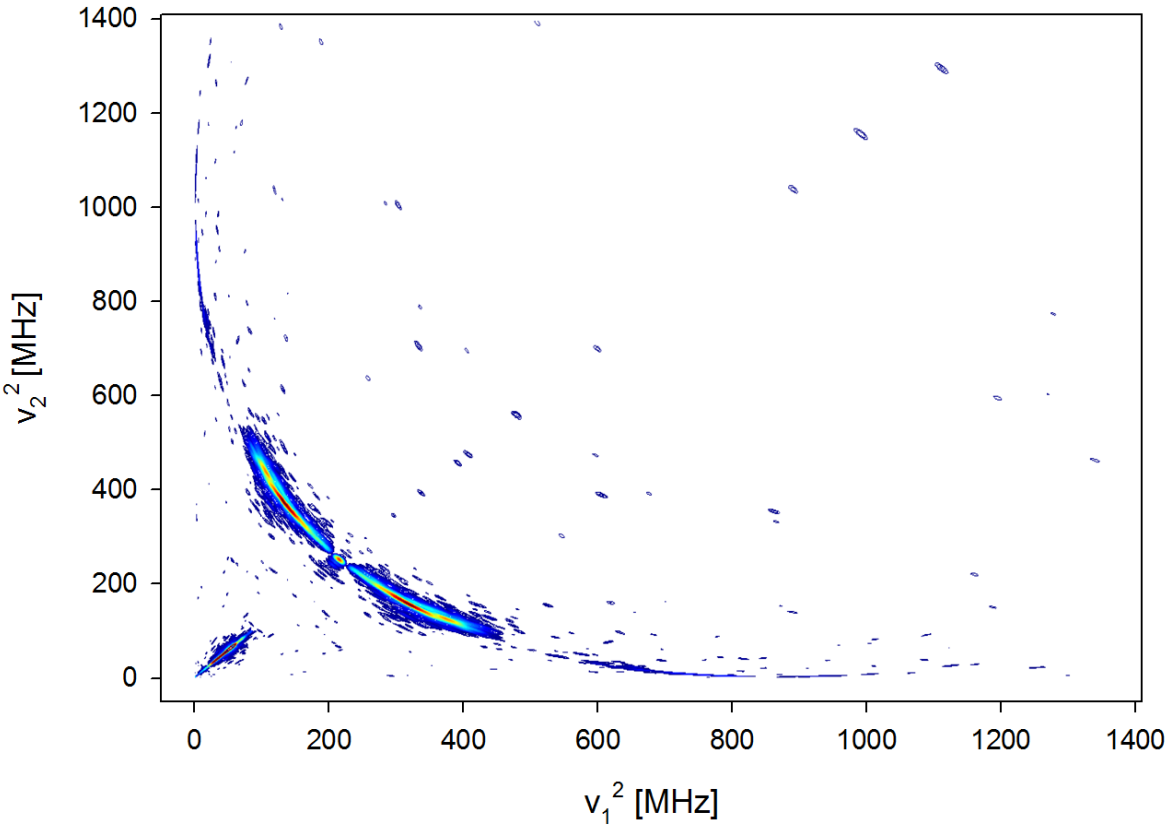

Figure 4.9: *The enlarged region of 2D HYSCORE spectrum of p-coumaryl alcohol illuminated at pH 11.15 in the frequency-squared coordinate system.*

4.5 Conclusions

With the slow motion of radical in the frozen state, anisotropic hyperfine interaction is not averaged out as the sample in liquid, contributing with Fermi contact to result an unresolved single line in CW X-band EPR spectrum. Distinct line shape between hydroxycinnamic acid and hydroxycinnamyl alcohol reflects the fact that the two extra protons at Cγ have significant interactions with unpaired electron. We have obtained

HYSCORE spectra from the radicals generated by broad spectrum illumination in UV-VIS region on *p*-coumaric acid and *p*-coumaryl alcohol in aqueous buffer. Despite surprisingly fast electronic relaxation, likely caused by aggregation of radicals or unusual reactivity of matrix protons in non-glassy matrix, we were able to obtain spectra with sufficient resolution to characterize four unique spin-proton interactions in radicals formed in *p*-coumaric acid: two ring protons at C3 and C5 positions with a_{iso}.= 13.7 MHz and 13.1 MHz, multiple weak couplings assigned to ring protons at C2 and C4 and protons in tail with a_{iso}<11 MHz, hydrogen bonding with small a_{iso}= 0.64 MHz and large hyperfine anisotropy *T*=3.04 MHz, and two free rotating protons in tail with a_{iso}.= 22.47 MHz and 18.48 MHz and *T*=2.62 MHz and 1.77 MHz, respectively. As far as we know, the only protons capable of having a combination of strong isotropic and small anisotropic couplings in ratio $T \approx 10\%\ a_{iso}$ are β-methylene protons of π-radical. Therefore, we assigned the free rotating protons as β-methylene protons. They are highly likely located at Cα where the methylene group is formed as a result of reduction of double bond upon illumination.

2D HYSCORE of *p*-coumaryl alcohol showed worse spectrum resolution, but we still observed a very similar combination of a_{iso} and *T as* β-methylene protons. Thus, we believe that the two protons are either methylene protons at Cγ position or β-methylene protons formed at Cα position as a result of the side chain double-bond reduction upon illumination. Based on above results, during UV illumination of monolignols secondary reactions could occur and result in radical species structurally different from monolignol radicals enzymatically generated. Significant differences between hyperfine parameters for protons in *p*-coumaric acid derived radicals and *p*-coumaryl alcohol derived radical clearly

demonstrates that HYSCORE can provide sufficient information to completely characterize and identify structure of radicals derived from model compounds and opens way to characterize radical spices in natural lignin systems. To our knowledge this is a first report of HYSCORE characterization of model monolignol radicals.

CHAPTER 5

An Approach to Study the Monolignol Radicals formed upon Consecutive Deglucosidation and Oxidative Dehydrogenation of Monolignol Glucoside using Continuous-flow in combination with IE-EPR spectroscopy

5.1 Introduction

Monolignol glucoside, often found in gymnosperms and some angiosperm, are demonstrated to play an important role as intermediate in biosynthesis of lignin in cell wall[64] (Figure 5.1). With glucosylation at 4-*O*-*β* position, monolignol glucoside acts as storage or transport form of monolignol and glucoside is viewed as reservoir to augment the monolignol supply for lignification. Monolignol glucosylation is catalyzed by soluble UDP-glucose, it is possibly sequestrated first from cytosol to vacuole then be transported from vacuole to cell wall through an unknown mechanism. *β*-Glucosidase is known to catalyze the highly efficient hydrolysis of a variety of glucosides via a double displacement mechanism involving two carboxylic acids, providing important function to cell wall lignification[65]. One mechanism is proposed that the glucose from deglucosidation is oxidized by glucose oxidase and oxygen to give hydrogen peroxide which then acts with peroxidase to oxidize monolignol *in situ*[66]. The DHPs from monolignol glucoside in the presence of *β*–

glucosidase, peroxidase, glucose oxidase and oxygen presents the closer approximation to the structure of milled wood lignin than dose the structure of DHP prepared by the conventional method without the step of deglucosidation before oxidation[66].

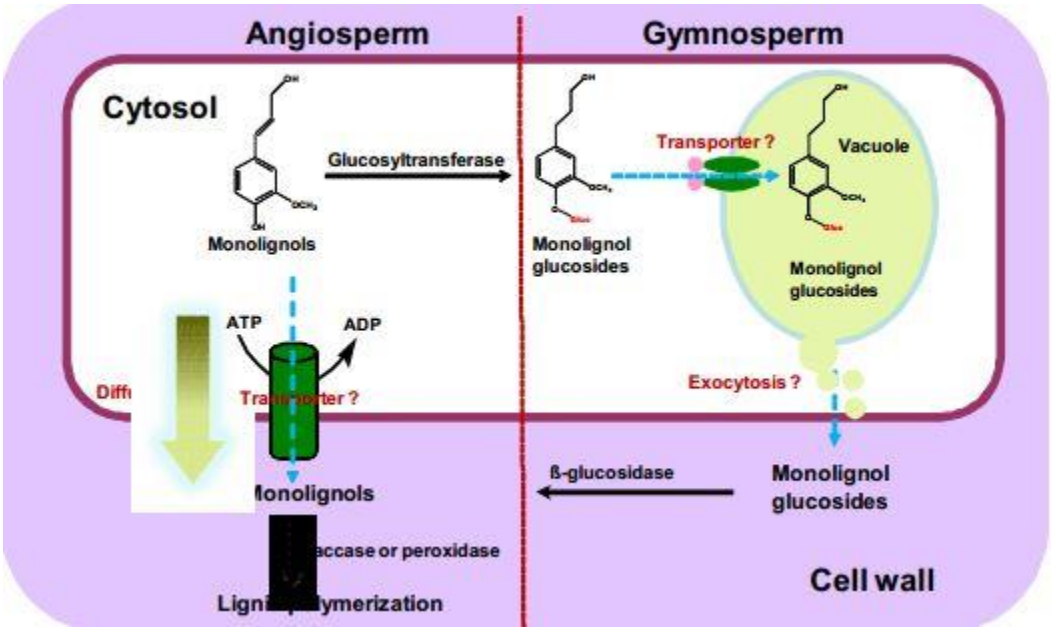

Figure 5.1: *Alternative pathways of monolignol transport*[64].

One character of monolignol glucoside is its stability and hydrophilicity. Monolignol is relatively toxic and unstable. Glucosylation of monolignol is known to reduce the lipophilicity of monolignol, thus preventing the possibility of free diffusion of monolignol across the lipid bilayer. Hydroxycinnamates, hydroxycinnamyl acetates and monolignol-hydrxycinnamate conjugates are all potential lignin precursors, however, limited by aqueous solubility, they are not amendable to the continuous-flow EPR experiments for determination of isotropic hyperfine parameters. Therefore, we propose to mimic the process of glucosylation followed by deglucosidation in attempt to create higher local concentration of

monolignols with limited solubility in water before the reaction with HRP. The monolignol after glucosylation becomes water-soluble, it is flushed first through immobilized *β*–glucosidase for deglucosidation and through HRP for oxidative dehydrogenation. The method allows the continuous generation of monolignol radical and detection by EPR spectroscopy *in situ*. Given the significantly less rapid catalytical circle of *β*–glucosidase compared to HRP, two immobilized enzymes in different amount ratio are separately placed as Figure 5.2, in which the length between two immobilized enzymes is minimized to maximize the amount of deglucosidated compounds in the phase of liquid for next oxidation.

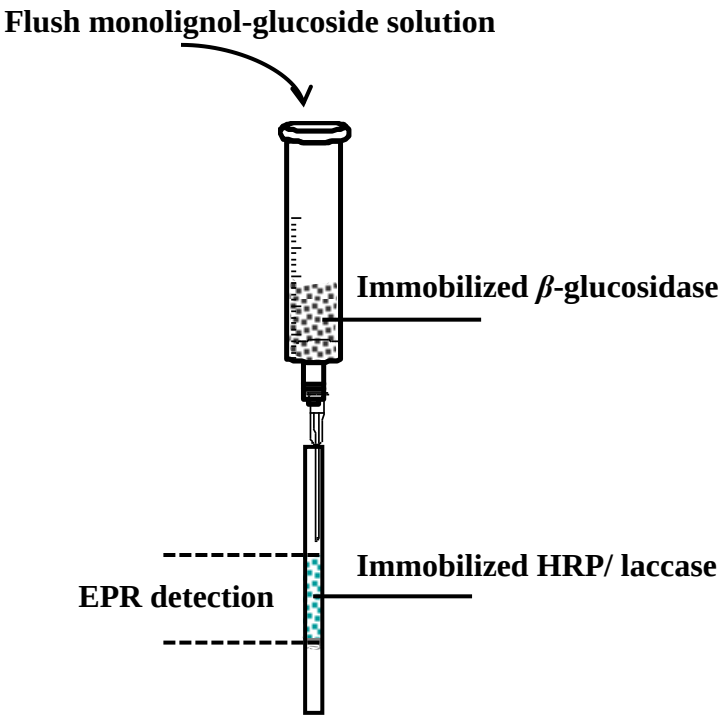

Figure 5.2: *An overview of syringe barrel and EPR quartz capillary packed with immobilized enzymes.*

5.2 Materials and reagents

Horseradish peroxidase (HRP, Type II) from Sigma and *β*-glucosidase (from sweet almonds) from MP Biomedicals were used without further purification. Affi-Gel 10 and Chelex-100 were purchased from BioRad laboratories. *p*-Glucocoumaryl alcohol was synthesized using previously published procedures (Figure 5.3). All other chemicals were optioned from Alfa Aesar, Sigma-Aldrich, and Oakwood. Phosphate buffer was made from 10-fold concentration that underwent a 24-hour Chelex-100 treatment. After removal of Chelex-100, DTPA was added to buffer concentrate which was then diluted to final concentration 50 mM with ultrapure water followed by pH adjustment to 5.5. Quinoline was additionally purified by vacuum distillation.

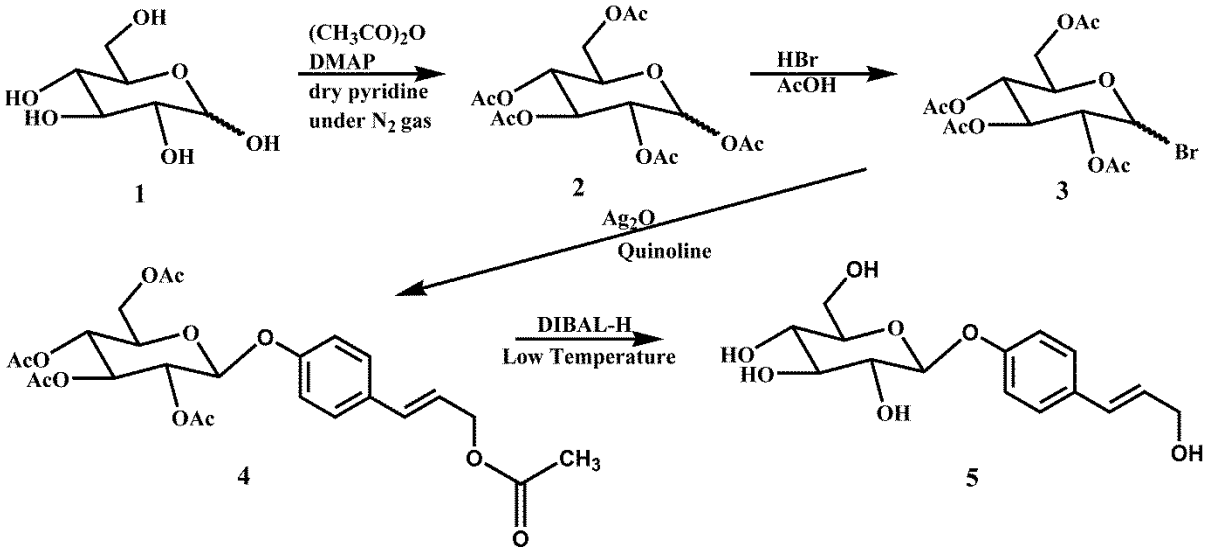

Figure 5.3: *Scheme of the synthesis of p-glucocoumaryl alcohol.*

Synthesis of 1, 2, 3, 4, 6-Penta-*O*-acetyl-*β*-D-glucopyranose (2)[67]: D-glucose (18.0 g, 100 mmol) was acetylated in 150 ml of pyridine in the presence of 4-dimethyllaminopyridine

(DMAP 1.22g, 10 mmol) by dropwise addition of acetic anhydride (95 ml, 1000 mmol) over 20 min at 0 ℃ under nitrogen, followed by overnight stirring at room temperature. Dilute the reaction mixture with ethyl acetate (300 ml) and wash it with 1N hydrochloric acid, saturated sodium bicarbonate and brine. The organic layer was dried over anhydrous $MgSO_4$ overnight and filtered and the solvent was removed in vacuum. Recrystallization from hexanes/ethyl acetate gave 2 (yield 77%) in two forms: ^{1}H NMR ($CDCl_3$), 6.33/5.71 (d, 1H, H1), 5.47/5.25 (t, 1H, H3), 5.17/5.13 (t, 1H, H4), 5.09/5.11 (dd, 1H, H2), 4.28-4.25 (m, 1H, H6b), 4.10-4.07 (m, 2H, H6a); 4.12/3.85 (ddd, 1H, H5), 2.17-2.01 (m, 15H, Ac OCH_3) ppm; ^{13}C NMR ($CDCl_3$), 170.90-169.04 (5Ac C=O), 91.94/89.31 (C1), 73.02/72.95 (C3), 70.45/70.07 (C5), 70.07/69.43 (C2), 68.11/67.97 (C4), 61.70 (C6), 21.16-20.73 (5Ac CH_3) ppm.

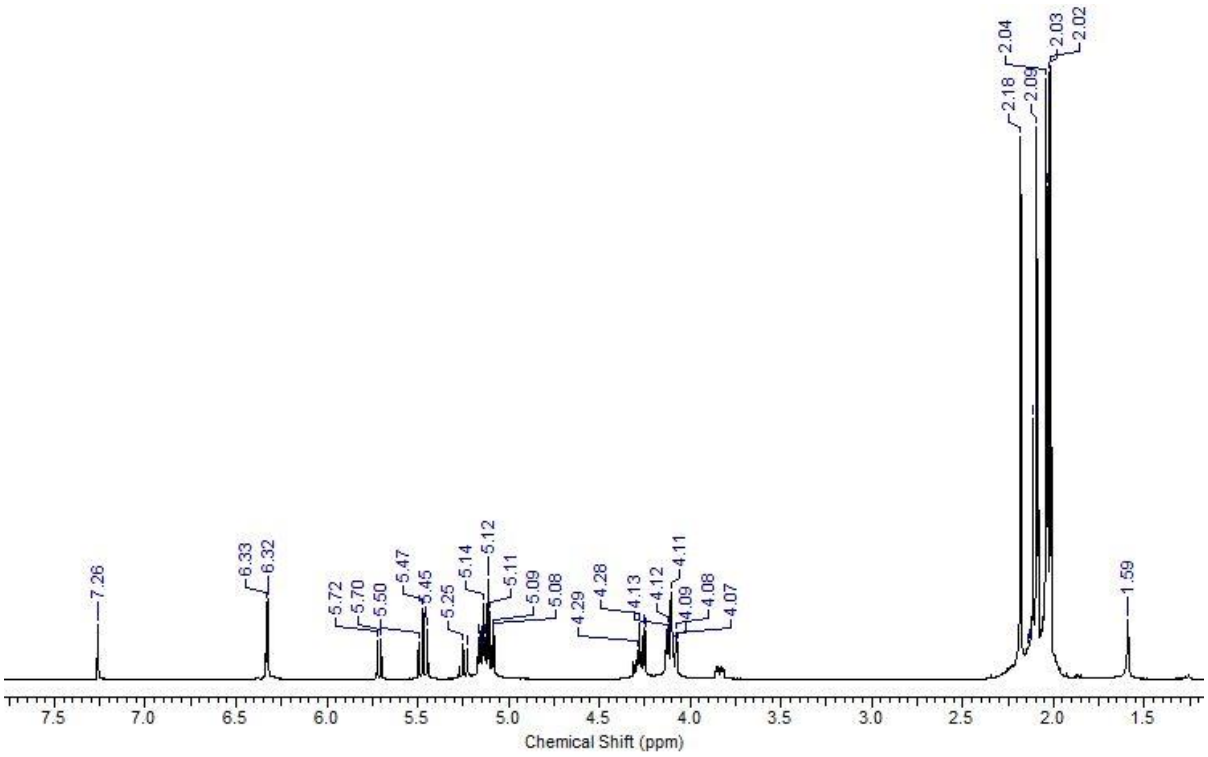
7.26
6.33
6.32
5.72
5.70
5.50
5.47
5.45
5.25
5.14
5.12
5.11
5.09
5.08
4.29
4.28
4.13
4.12
4.11
4.09
4.08
4.07
2.18
2.09
2.04
2.03
2.02
1.59
Chemical Shift (ppm)

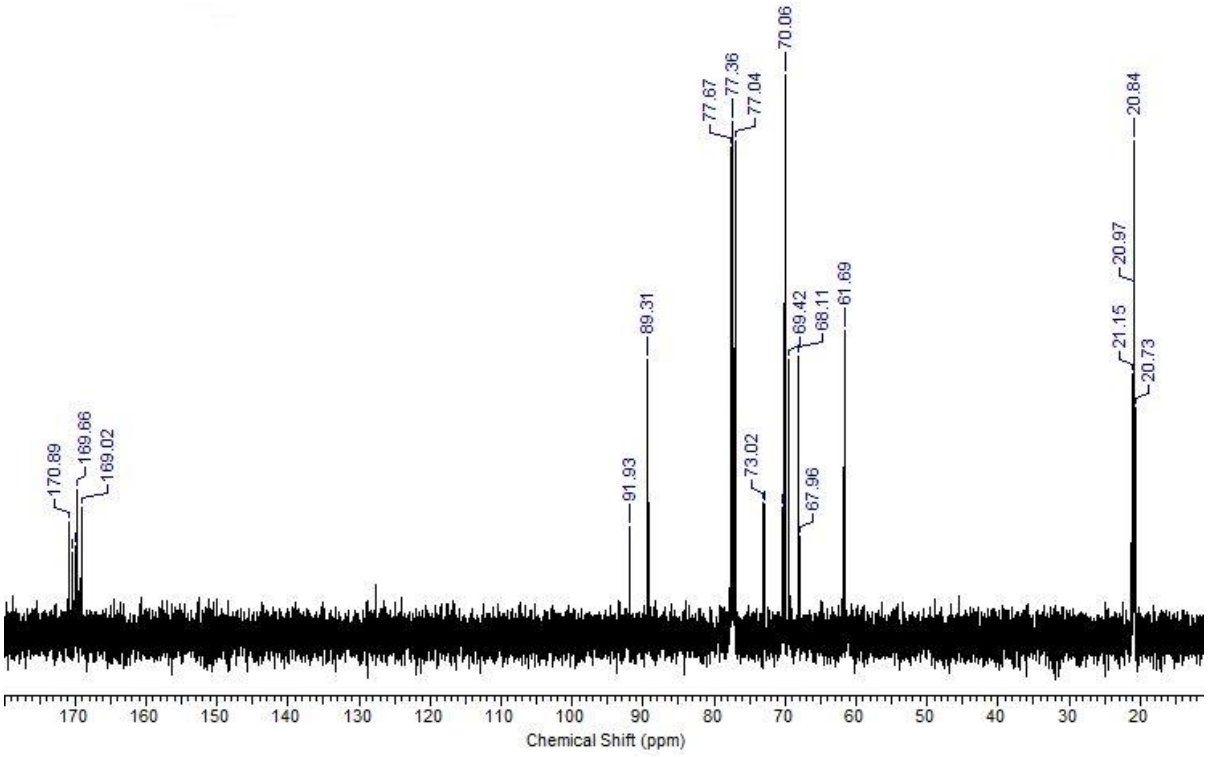
170.89
169.66
169.02
91.93
89.31
77.67
77.36
77.04
73.02
70.06
69.42
68.11
67.96
61.69
21.15
20.97
20.84
20.73
Chemical Shift (ppm)

Figure 5.4: *1H and 13C NMR spectra of 1, 2, 3, 4, 6-Penta-O-acetyl-β-D-glucopyranose.*

Synthesis of 2, 3, 4, 6-Tetra-*O*-acetyl-*α*-D-glucopyranosyl bromide (3)[68]: 2 (25 g, 60 mmol) was potion wise added to a stirred solution of HBr (33% w/w) in acetic acid (62.5 ml) at 0 ℃. After the addition of all 2, the reaction mixture was allowed to warm to room temperature and kept stirring for 45 min. Then the reaction was quenched with ice water (125 ml) and extracted with dichloromethane. The combined organic extracted were washed with saturated $NaHCO_3$, dried over Na_2SO_4 overnight and filtered and the solvent was removed in vacuum. The residual was then purified by silica gel column chromatography (n-hexanes: ethyl acetate = 3:2 (v/v)). Recrystallization from hexanes/ethyl acetate gave 3 (yield 70%): ^{1}H NMR ($CDCl_3$), 6.60 (d, 1H, H1), 5.55(t, 1H, H3), 5.15 (t, 1H, H4), 4.83 (dd, 1H, H2), 4.30 (m, 2H, H6b and H5), 4.12 (m, 1H, H6a), 2.09, 2.08, 2.05, 2.04, 2.03, 2.02 (s, 12H, Ac OCH_3) ppm.

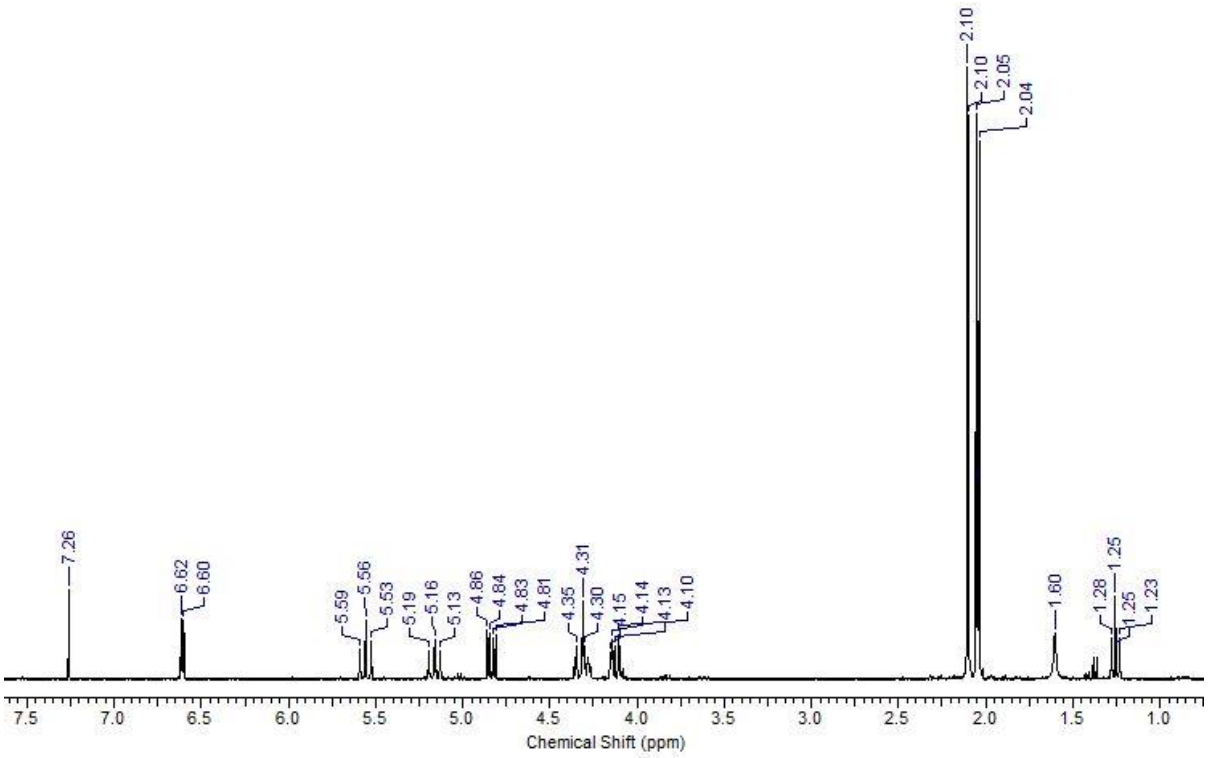

Figure 5.5: *1H NMR spectrum of 2, 3, 4, 6-Tetra-O-acetyl-α-D-glucopyranosyl bromide.*

Synthesis of 4-O-[Tetra-*O*-acetyl-*β*-D-gluco]-methyl *p*-coumarate (4)[69]: Methly *p* – coumarate (1.70 g, 9.52 mmol) and 3 (3.91 g, 9.52 mmol) were dissolved in quinolone (14 ml), and silver oxide (1.326 g, 5.72 mml) was portionwise added. After 1.5 h, acetic acid (10 ml) was added and the whole mixture was poured into water (100 ml). The fine precipitate was collected by filtration and extracted three times with hot ethanol (25 ml*3). After removing solvent, the residual was then purified by silica gel column chromatography (n-hexane:ethyl acetate = 4:1 (v/v)). Re crystallization from ethanol gave 4 (yield 49%): ^{1}H NMR ($(CD_3)_2SO$), 7.72 (d, 1H, H2), 7.63 (d, 1H, Hα), 7.02 (d, 2H, H3 and H5), 6.56 (d, 1H, Hβ), 5.65 (d, 1H, H1'), 5.41 (d, 1H, H3'), 5.07 (t, 1H, H2'), 5.00 (t, 1H, H4'), 4.23-4.05 (m, 3H, H5',H6a' and H6b'), 3.71 (s, 3H, OCH_3), 2.01 (s, 9H, Ac OCH_3), 1.97 (s, 3H, Ac OCH_3)

ppm; ^{13}C NMR ($(CD_3)_2SO$), 166.40 (Ac C=O), 166.05 (Ac C=O), 165.75 (Ac C=O), 165.54 (Ac C=O), 163.22 (Cγ), 154.31 (C4), 140.29 (Cα), 126.57 (C2 and C6), 125.22 (C1), 112.93 (C3 and C5), 112.83 (Cβ), 93.00 (C1'), 68.31 (C3'), 67.30 (C5'), 67.01 (C2'), 64.38 (C4'), 58.00 (C6'), 47.82 (CH_3), 16.91, 16.82 , 16.91, 16.75, 16.70 (5Ac OCH_3) ppm.

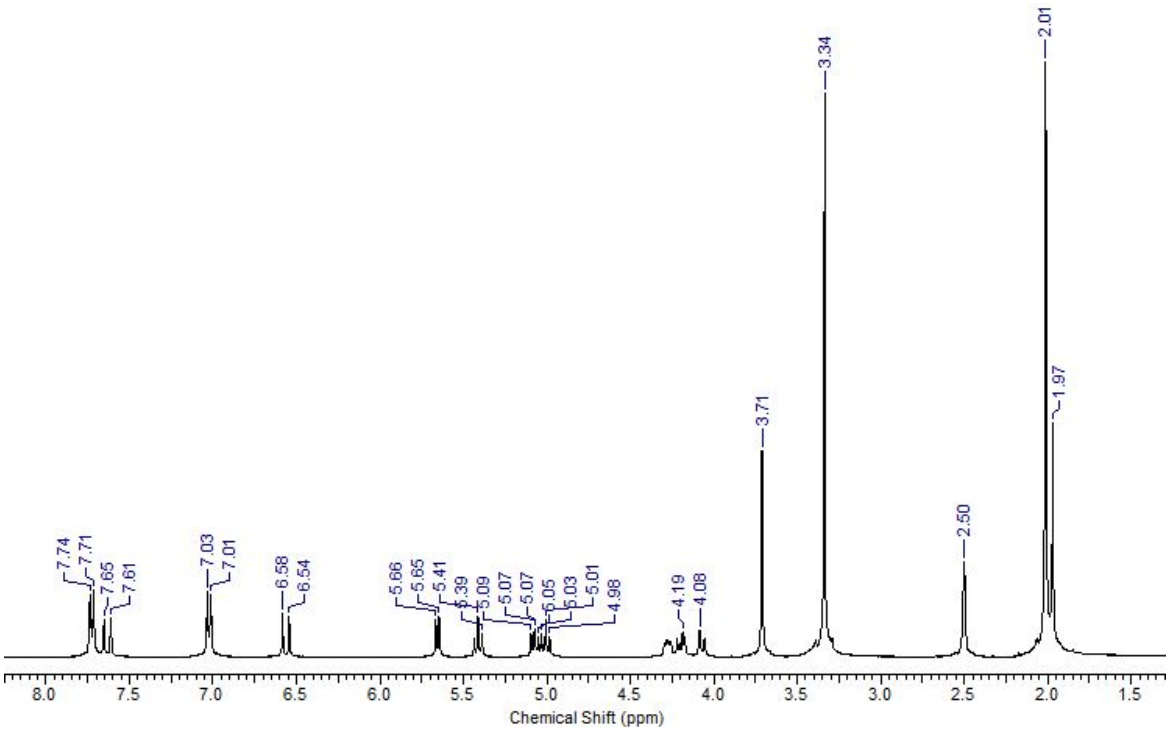

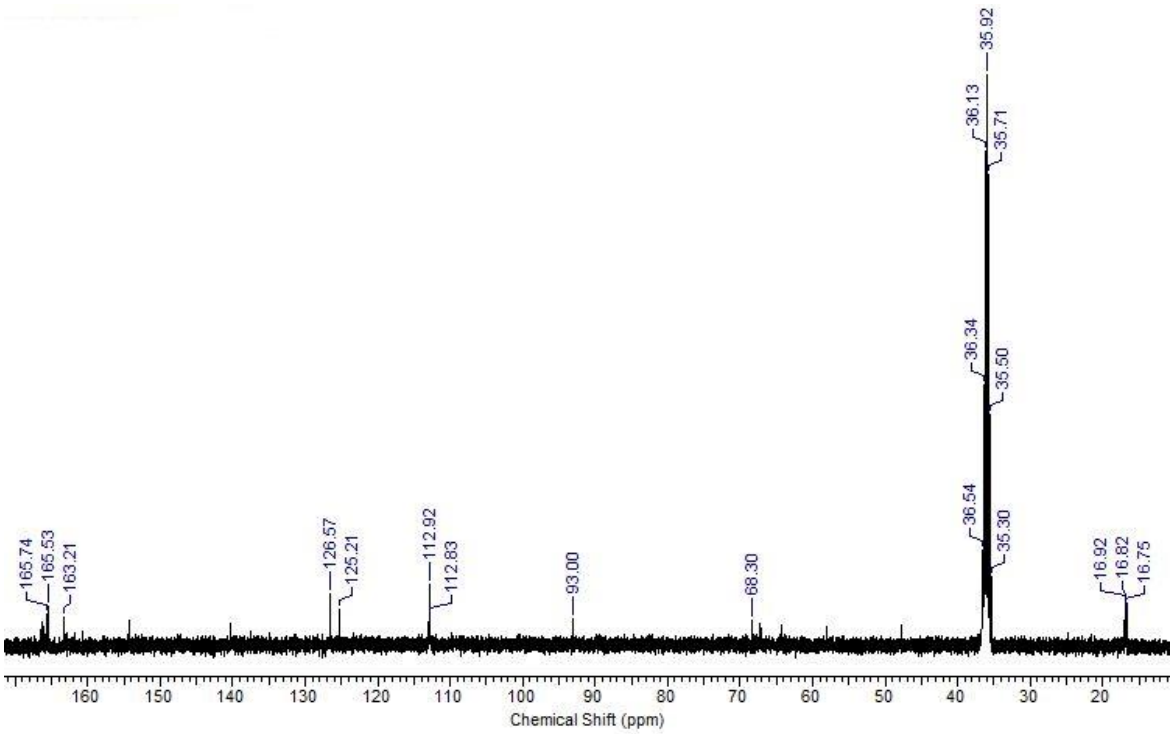

Figure 5.6: *1H and 13C NMR spectra of 4-O-[Tetra-O-acetyl-β-D-gluco]-methyl p-coumarate.*

Synthesis of *p*-glucocoumaryl alcohol (5)[6969]: 4 (188 mg, 0.39 mmol) was dissolved in anhydrous toluene (13 ml), and was reduced by dropwise addition of diisobutylaluminum hydride (4.9 ml, 0.39 mmol) via a dropping funnel over 20 min at 0 ℃ under argon. After additional 1 h the reaction was complete and carefully quenched by slow addition of ethanol (4 ml). The solvents were removed under vacuum. Water (10 ml) was added, the residual toluene separated on the water layer was removed under vacuum at 50 ℃. Then the aqueous solution was heated in hot water bath and filtered. The extraction with hot water (25 ml*2) for solid was repeated twice. Water was partially removed under vacuum at 50 ℃ for combined aqueous solution until white crystals presented (yield 52%): ^{1}H NMR (D_2O), 7.43 (d, 2H, H2 and H6), 7.07 (d, 2H, H3 and H5), 6.58 (d, 1H, Hα), 6.30 (d, 1H, Hβ), 5.07 (d,

1H, H1'), 5.21 (d, 2H, Hγ and Hγ'), 3.89 (dd, 1H, H6a'), 3.70 (dd, 1H, H6b'), 3.60-3.46 (m, 4H, H4',H3',H2' and H5') ppm; ^{13}C NMR (D_2O), 156.29 (C4), 131.93 (C1), 130.46 (Cβ), 127.99 (C2 and C6), 127.16 (Cα), 116.85 (C3 and C5), 100.20 (C1'), 76.23 (C3'), 75.65 (C5'), 73.02 (C2'), 69.53 (C4'), 62.42 (Cγ), 60.64 (C6) ppm.

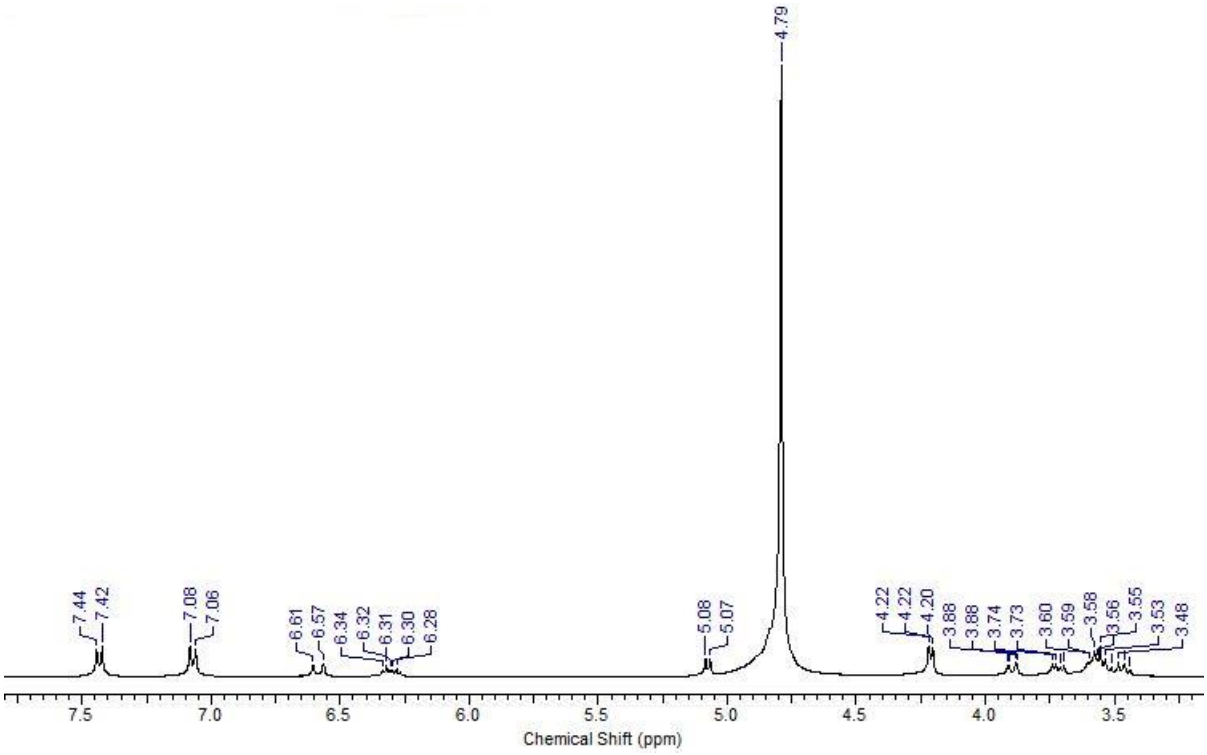

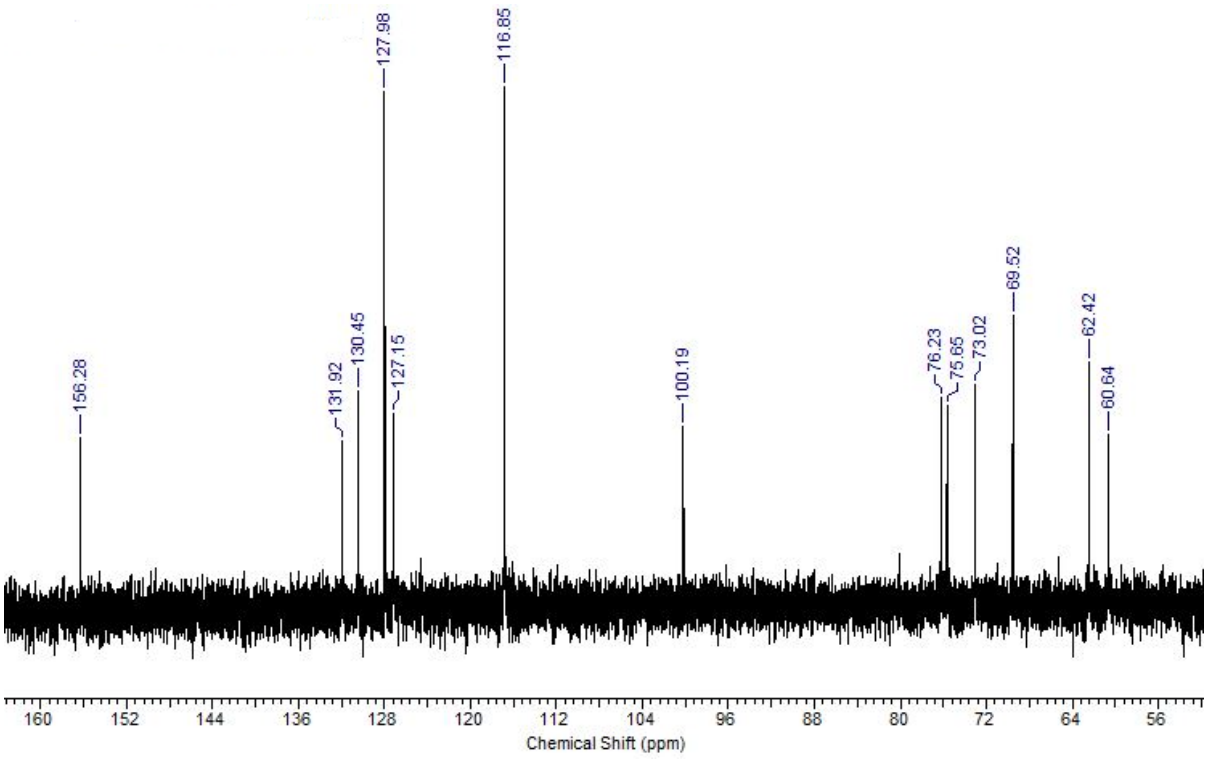

Figure 5.7: *1H and 13C NMR spectra of p-glucocoumaryl alcohol.*

5.3 Immobilization of *β*-glucosidase on Affi-Gel 10

2 ml Affi-Gel 10 was transferred to a small buchner funnel and the gel was washed with 3 bed volumes of cold water at 4 ℃. This step was finished in 20 min to avoid the gel going dry. The moist gel cake was added to cold enzyme solution (60 mg *β*-glucosidase dissolved in 3 ml MPOS buffer, pH=7.5) at 4 ℃, agitated sufficiently to make a uniform suspension. The suspension was kept under gentle agitation on a shaker for 4h at 4 ℃. To block the excess of active sites of gel, 0.1 ml 1 M glycine ethyl ester (dissolved in MOPS, pH= 8.0) was added and stirred for 1 h. Gel was separated from solution, washed with phosphate buffer and stored in phosphate buffer at 4 ℃. The coupling efficiency of *β*-

glucosidase was estimated spectroscopically at 278 nm from *β*-glucosidase solution prior to and after the immobilization.

5.4 Deglucosidation of monolignol glucoside at 48 ℃

A suspension of immobilized *β*-glucosidase (2 ml) was loaded in a modified syringe barrel which was exposed to a lab heater to maintain the temperature of immobilized *β*-glucosidase at 48 ℃. 2 mM *p*-glucocoumaryl alcohol solution was prepared in pH=5.5 phosphate buffer and flushed through the immobilized *β*-glucosidase in 0.3 ml/min flow rate. The solution passed through immobilized *β*-glucosidase was collected and analyzed by HPLC on a C4 10μ 300A 250 X 10 mm reversed-phase column (Phenomenex). The solvent gradient was 80% methanol with 0.1% trifluoroacetic acid (TFA) over 35 min, followed by 10% methanol with 0.1% TFA over final 7 minutes with a flow rate of 4 mL/minute. In Figure 5.8, *p*-coumaryl alcohol deglucosidated from *p*-glucocoumaryl alcohol eluted at approximately 17 min with approximate 52% deglucosidation efficiency.

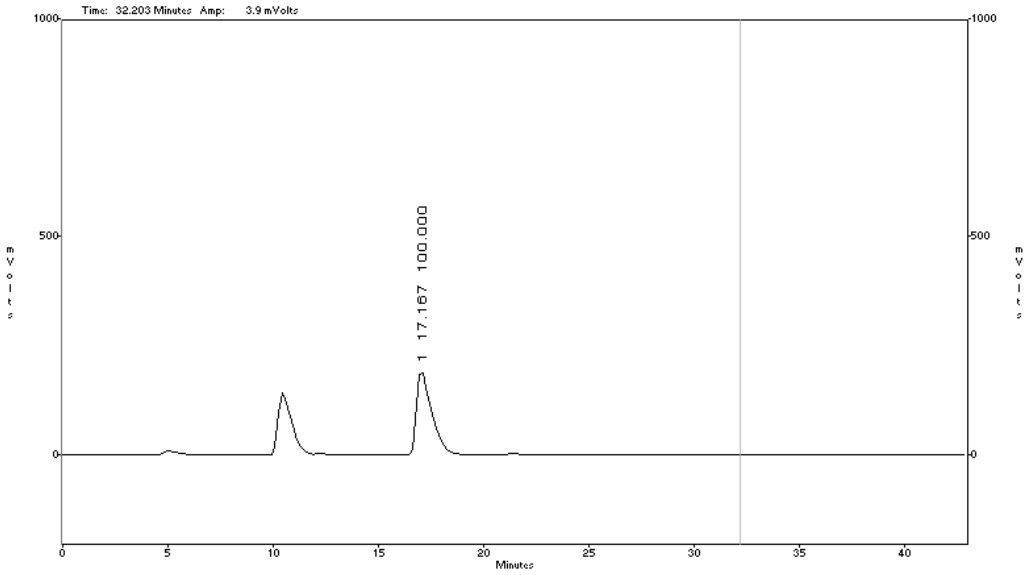

Figure 5.8: *Determination of p-coumaryl alcohol deglucosidated from p-glucocoumaryl alcohol by the function of immobilized β-glucosidase.*

5.5 *p*-Glucocoumaryl alcohol deglucosidation and oxidative dehydrogenation using *β*-glucosidase and HRP/H_2O_2

As shown in Figure 5.2, a suspension of immobilized *β*-glucosidase (2 ml) was loaded in a modified syringe barrel. Using a needle and teflon tape the syringe barrel was connected with a quartz capillary (1.1*1.6 mm) loaded with 16 ul immobilized HRP. 2 mM *p*-glucocoumaryl alcohol solution was prepared in pH=5.5 phosphate buffer and flushed with 1 mM H_2O_2 first through the immobilized *β*-glucosidase and then immobilized HRP. The radicals generated in the range of immobilized HRP were monitored by EPR spectroscopy. The temperature of EPR cavity was maintained at 48 ℃ by using a variable temperature accessory ER4113VT and a heater/ thermocouple cable BVT3000.

5.6 CW EPR spectroscopy and temperature-control set-up

Room temperature CW EPR measurements were conducted using Bruker ELEXSYS E500 spectrometer at microwave frequencies, v approximately 9.5 GHz (X-band) and magnetic strength, B =3365 G. The modulation amplitude was 0.8 G and the modulation frequency was 100 kHz. The time constant was set at 81.92 ms with a 41.09 ms conversion time and a 42.08 s sweep time. 1024 point spectra were collected over a 60 G range. Cryostat and transfer line were assembled to the cavity. A glass tube, wrapped with styrofoam sheets, was connected to transfer line at one site and thermocouple at the other site. Room-temperature nitrogen gas inlet allowed for the nitrogen gas heat-up before transferring to the cavity.

5.7 Results and discussion

A broad single line was observed from the EPR detection at the region of immobilized HRP during the flushing of *p*-glucocoumaryl alcohol solution through immobilized β-glucosidase and HRP. The sequential spectrum collected at different time points shows an increase of the signal intensity (Figure 5.9). From the results of spectral simulation, signal intensity was found to grow (slope ≈ 0.02) linearly as a function of time, while the line shape remained unchanged (~ 6.10 G). The phenomenon corresponds to that of oxidizing *p*-coumaryl alcohol by immobilized HRP in Chapter 3 where the broad line is proven to be attributed to the production and accumulation of polymeric radical. Differently,

the rate of accumulation of polymeric radical in here is much slower, which is probably caused by lowered *p*-coumaryl alcohol concentration and higher reaction temperature.

Overall, we designed a method combing continuous-flow system and surface immobilization of two types of enzyme to generate monolignol radicals using consecutive enzymatic deglucosidation and oxidative dehydrogenation of monolignol glucoside. This approach could potentially be used to study monolignol radicals from monolignols with limited solubility in water, especially for monolignol hydroxycinnamate conjugate compounds whose isotropic hyperfine component have not been studied yet. Through glucosylation and subsequent deglucosidation, the process occurred in nature, the effective reaction with enzyme could be obtained without the use of any biological-unrelated reagent.

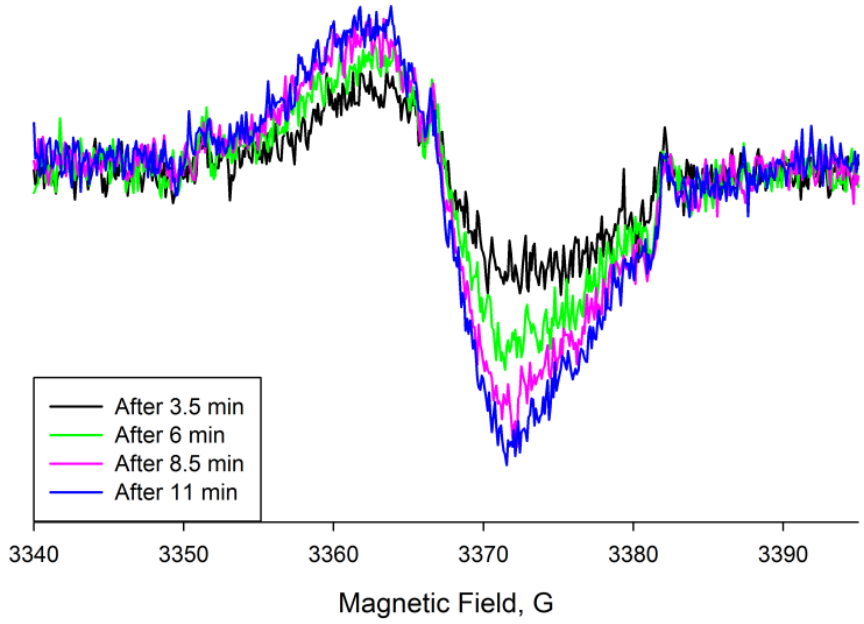

Figure 5.9: *Room temperature CW EPR spectra obtained from the detection at the region of immobilized HRP during the flushing of mixture of p-glucocoumaryl alcohol solution and* H_2O_2 *through immobilized β-glucosidase and HRP.*

REFERENCES

1. Novaes, E.; Kirst, M.; Chiang, V.; Winter-Sederoff, H.; Sederoff, R., Lignin and biomass: a negative correlation for wood formation and lignin content in trees. *Plant Physiology* **2010,** *154* (2), 555-561.

2. Hu, T. Q., *Chemical modification, properties, and usage of lignin*. Springer: **2002**.

3. Chen, F.; Dai, H.; Dong, X.; Yang, J.; Zhong, M., Physical properties of lignin-based polypropylene blends. *Polymer Composites* **201**1, *32* (7), 1019-1025.

4. Siqueira, G.; Milagres, A. M.; Carvalho, W.; Koch, G.; Ferraz, A., Topochemical distribution of lignin and hydroxycinnamic acids in sugar-cane cell walls and its correlation with the enzymatic hydrolysis of polysaccharides. *Biotechnology for biofuels* **2011**, *4* (1), 1.

5. *http://www.psb.ugent.be/bio-energy/313-lignin*

6. (a) Vanholme, R.; Demedts, B.; Morreel, K.; Ralph, J.; Boerjan, W., Lignin biosynthesis and structure. *Plant physiology* **2010,** *153* (3), 895-905; (b) Hatfield, R.; Vermerris, W., Lignin formation in plants. The dilemma of linkage specificity. *Plant Physiology* **2001,** *126* (4), 1351-1357.

7. Liu, C.-J., Deciphering the enigma of lignification: precursor transport, oxidation, and the topochemistry of lignin assembly. *Molecular plant* **2012,** *5* (2), 304-317.

8. Wang, Y.; Chantreau, M.; Sibout, R.; Hawkins, S., Plant cell wall lignification and monolignol metabolism. *Front Plant Sci* **2013,** *4*, 220.

9. Boerjan, W.; Ralph, J.; Baucher, M., Lignin biosynthesis. *Annual review of plant biology* **2003,** *54* (1), 519-546.

10. Achyuthan, K. E.; Achyuthan, A. M.; Adams, P. D.; Dirk, S. M.; Harper, J. C.; Simmons, B. A.; Singh, A. K., Supramolecular self-assembled chaos: polyphenolic lignin's barrier to cost-effective lignocellulosic biofuels. *Molecules* **2010,** *15* (12), 8641-8688.

11. Lin, S. Y.; Dence, C. W., *Methods in lignin chemistry*. Springer Science & Business Media: **2012**.

12. Kim, H.; Ralph, J.; Lu, F.; Ralph, S. A.; Boudet, A.-M.; MacKay, J. J.; Sederoff, R. R.; Ito, T.; Kawai, S.; Ohashi, H., NMR analysis of lignins in CAD-deficient plants. Part 1. Incorporation of hydroxycinnamaldehydes and hydroxybenzaldehydes into lignins. *Organic & biomolecular chemistry* **2003,** *1* (2), 268-281.

13. Hatfield, R.; Ralph, J.; Grabber, J. H., A potential role for sinapyl p-coumarate as a radical transfer mechanism in grass lignin formation. *Planta* **2008,** *228* (6), 919-28.

14. Lu, F.; Ralph, J., Preliminary evidence for sinapyl acetate as a lignin monomer in kenaf. *Chemical Communications* **2002,** (1), 90-91.

15. (a) Scalbert, A.; Monties, B.; Guittet, E.; Lallemand, J., Comparison of wheat straw lignin preparations-I. Chemical and spectroscopic characterizations. *Holzforschung-International Journal of the Biology, Chemistry, Physics and Technology of Wood* **1986,** *40* (2), 119-127; (b) Sharma, U.; Brillouet, J.-M.; Scalbert, A.; Monties, B., Studies on a brittle stem mutant of rice, Oryza sativa L.; characterization of lignin fractions, associated phenolic acids and polysaccharides from rice stem. *Agronomie* **1986,** *6* (3), 265-271.

16. Iiyama, K.; Lam, T. B. T.; Stone, B. A., Phenolic acid bridges between polysaccharides and lignin in wheat internodes. *Phytochemistry* **1990,** *29* (3), 733-737.

17. Lam, T. B. T.; Iiyama, K.; Stone, B. A., Determination of etherified hydroxycinnamic acids in cell walls of grasses. *Phytochemistry* **1994,** *36* (3), 773-775.

18. (a) Jung, H.; Buxton, D.; Hatfield, R.; Ralph, J., *Forage cell wall structure and digestibility*. American Society of Agronomy, Inc.: **1993**; (b) Ralph, J.; Lundquist, K.; Brunow, G.; Lu, F.; Kim, H.; Schatz, P. F.; Marita, J. M.; Hatfield, R. D.; Ralph, S. A.; Christensen, J. H., Lignins: natural polymers from oxidative coupling of 4-hydroxyphenyl-propanoids. *Phytochemistry Reviews* **2004,** *3* (1-2), 29-60; (c) Ralph, J., Hydroxycinnamates in lignification. *Phytochemistry Reviews* **2010,** *9* (1), 65-83.

19. Ralph, J.; Bunzel, M.; Marita, J. M.; Hatfield, R. D.; Lu, F.; Kim, H.; Schatz, P. F.; Grabber, J. H.; Steinhart, H., Peroxidase-dependent cross-linking reactions of p-hydroxycinnamates in plant cell walls. *Phytochemistry Reviews* **2004,** *3* (1-2), 79-96.

20. (a) Ralph, J., An unusual lignin from kenaf. *Journal of natural products* **1996,** *59* (4), 341-342; (b) Sarkanen, K.; Chang, H.-M.; Allan, G., Species variation in lignins. 3. Hardwood lignins. *Tappi* **1967,** *50* (12), 587-&; (c) Del R ó, J. C.; Marques, G.; Rencoret, J.; Mart ínez, Á. T.; Guti érrez, A., Occurrence of naturally acetylated lignin units. *Journal of Agricultural and Food Chemistry* **2007,** *55* (14), 5461-5468.

21. (a) Battistuzzi, G.; Bellei, M.; Bortolotti, C. A.; Sola, M., Redox properties of heme peroxidases. *Archives of biochemistry and biophysics* **2010,** *500* (1), 21-36; (b) Takahama, U., Oxidation of hydroxycinnamic acid and hydroxycinnamyl alcohol derivatives by laccase and peroxidase. Interactions among p-hydroxyphenyl, guaiacyl and syringyl groups during the oxidation reactions. *Physiologia Plantarum* **1995,** *93* (1), 61-68.

22. (a) Veitch, N. C., Horseradish peroxidase: a modern view of a classic enzyme. *Phytochemistry* **2004,** *65* (3), 249-259; (b) Azevedo, A. M.; Martins, V. C.; Prazeres, D. M.;

Vojinović, V.; Cabral, J. M.; Fonseca, L. P., Horseradish peroxidase: a valuable tool in biotechnology. *Biotechnology annual review* **2003,** *9*, 199-247.

23. Huang, L.; Colas, C.; Ortiz de Montellano, P. R., Oxidation of carboxylic acids by horseradish peroxidase results in prosthetic heme modification and inactivation. *Journal of the American Chemical Society* **2004,** *126* (40), 12865-12873.

24. Santhanam, N.; Vivanco, J. M.; Decker, S. R.; Reardon, K. F., Expression of industrially relevant laccases: prokaryotic style. *Trends in biotechnology* **2011,** *29* (10), 480-489.

25. (a) Kersten, P. J.; Kalyanaraman, B.; Hammel, K. E.; Reinhammar, B.; Kirk, T. K., Comparison of lignin peroxidase, horseradish peroxidase and laccase in the oxidation of methoxybenzenes. *Biochem. J* **1990,** *268*, 475-480; (b) Gavnholt, B.; Larsen, K., Molecular biology of plant laccases in relation to lignin formation. *Physiologia plantarum* **2002,** *116* (3), 273-280.

26. Durán, N.; Rosa, M. A.; D'Annibale, A.; Gianfreda, L., Applications of laccases and tyrosinases (phenoloxidases) immobilized on different supports: a review. *Enzyme and Microbial Technology* **2002,** *31* (7), 907-931.

27. Hatfield, R.; Ralph, J.; Grabber, J. H., A potential role for sinapyl p-coumarate as a radical transfer mechanism in grass lignin formation. *Planta* **2008,** *228* (6), 919-928.

28. Önnerud, H.; Zhang, L.; Gellerstedt, G.; Henriksson, G., Polymerization of Monolignols by Redox Shuttle–Mediated Enzymatic Oxidation A New Model in Lignin Biosynthesis I. *The Plant Cell* **2002,** *14* (8), 1953-1962.

29. Higuchi, T., Lignin biochemistry: biosynthesis and biodegradation. *Wood Science and Technology* **1990,** *24* (1), 23-63.

30. Adler, E., Lignin chemistry—past, present and future. *Wood Science and Technology* **1977,** *11* (3), 169-218.

31. Touzel, J.-P.; Chabbert, B.; Monties, B.; Debeire, P.; Cathala, B., Synthesis and characterization of dehydrogenation polymers in Gluconacetobacter xylinus cellulose and cellulose/pectin composite. *Journal of agricultural and food chemistry* **2003,** *51* (4), 981-986.

32. (a) Mattinen, M.-L.; Suortti, T.; Gosselink, R.; Argyropoulos, D. S.; Evtuguin, D.; Suurnäkki, A.; de Jong, E.; Tamminen, T., Polymerization of different lignins by laccase. *BioResources* **2008,** *3* (2), 549-565; (b) Yabuta, G.; Koizumi, Y.; Namiki, K.; Hida, M.; Namiki, M., Structure of green pigment formed by the reaction of caffeic acid esters (or chlorogenic acid) with a primary amino compound. *Bioscience, biotechnology, and biochemistry* **2001,** *65* (10), 2121-2130; (c) Barsberg, S.; Matousek, P.; Towrie, M.; Jørgensen, H.; Felby, C., Lignin radicals in the plant cell wall probed by Kerr-gated

resonance Raman spectroscopy. *Biophysical journal* **2006,** *90* (8), 2978-2986; (d) Russell, W. R.; Burkitt, M. J.; Scobbie, L.; Chesson, A., Radical formation and coupling of hydroxycinnamic acids containing 1, 2-dihydroxy substituents. *Bioorganic chemistry* **2003,** *31* (3), 206-215.

33. (a) Steelink, C., Free radical studies of lignin, lignin degradation products and soil humic acids. *Geochimica et Cosmochimica Acta* **1964,** *28* (10), 1615-1622; (b) Steelink, C., Stable Phenoxy Radicals Derived from Phenols Related to Lignin1. *Journal of the American Chemical Society* **1965,** *87* (9), 2056-2057; (c) Fitzpatrick, J.; Steelink, C., Benzosemiquinone radicals in alkaline solutions of hardwood lignins. *Tetrahedron letters* **1969,** *10* (57), 5041-5044.

34. (a) Taboada-Puig, R.; Lú-Chau, T.; Moreira, M.; Feijoo, G.; Lema, J., Activation of Kraft lignin by an enzymatic treatment with a versatile peroxidase from Bjerkandera sp. R1. *Applied biochemistry and biotechnology* **2013,** *169* (4), 1262-1278; (b) Crestini, C.; Crucianelli, M.; Orlandi, M.; Saladino, R., Oxidative strategies in lignin chemistry: A new environmental friendly approach for the functionalisation of lignin and lignocellulosic fibers. *Catalysis today* **2010,** *156* (1), 8-22.

35. Bährle, C.; Nick, T. U.; Bennati, M.; Jeschke, G.; Vogel, F., High-Field Electron Paramagnetic Resonance and Density Functional Theory Study of Stable Organic Radicals in Lignin: Influence of the Extraction Process, Botanical Origin, and Protonation Reactions on the Radical g Tensor. *The Journal of Physical Chemistry A* **2015,** *119* (24), 6475-6482.

36. Russell, W. R.; Forrester, A. R.; Chesson, A.; Burkitt, M. J., Oxidative coupling during lignin polymerization is determined by unpaired electron delocalization within parent phenylpropanoid radicals. *Archives of biochemistry and biophysics* **1996,** *332* (2), 357-366.

37. (a) Russell, W. R.; Burkitt, M. J.; Scobbie, L.; Chesson, A., EPR investigation into the effects of substrate structure on peroxidase-catalyzed phenylpropanoid oxidation. *Biomacromolecules* **2006,** *7* (1), 268-273; (b) Russell, W. R.; Provan, G. J.; Burkitt, M. J.; Chesson, A., Extent of incorporation of hydroxycinnamaldehydes into lignin in cinnamyl alcohol dehydrogenase-downregulated plants. *Journal of biotechnology* **2000,** *79* (1), 73-85.

38. Bors, W.; Kazazic, S. P.; Michel, C.; Kortenska, V. D.; Stettmaier, K.; Klasinc, L., Methoxyphenols—antioxidant principles in food plants and spices: Pulse radiolysis, EPR spectroscopy, and density functional theory calculations. *International journal of quantum chemistry* **2002,** *90* (2), 969-979.

39. *http://www.sb.fsu.edu/~fajer/Fajerlab/LinkedDocuments/Primer.pdf*

40. Schweiger, A., Pulsed Electron Spin Resonance Spectroscopy: Basic Principles, Techniques, and Examples of Applications [New Analytical Methods (43)]. *Angewandte Chemie International Edition in English* **1991,** *30* (3), 265-292.

41. (a) Grönqvist, S.; Viikari, L.; Niku-Paavola, M.-L.; Orlandi, M.; Canevali, C.; Buchert, J., Oxidation of milled wood lignin with laccase, tyrosinase and horseradish peroxidase. *Applied microbiology and biotechnology* **2005,** *67* (4), 489-494; (b) Canevali, C.; Orlandi, M.; Zoia, L.; Scotti, R.; Tolppa, E.-L.; Sipila, J.; Agnoli, F.; Morazzoni, F., Radicalization of lignocellulosic fibers, related structural and morphological changes. *Biomacromolecules* **2005,** *6* (3), 1592-1601.

42. Zoia, L.; Argyropoulos, D. S., Phenoxy radical detection using 31P NMR spin trapping. *Journal of Physical Organic Chemistry* **2009,** *22* (11), 1070-1077.

43. McConnell, H. M.; Chesnut, D. B., Theory of Isotropic Hyperfine Interactions in π-Electron Radicals. *The Journal of Chemical Physics* **1958,** *28* (1), 107-117.

44. Makino, K.; Hagiwara, T.; Murakami, A., A mini review: fundamental aspects of spin trapping with DMPO. *International Journal of Radiation Applications and Instrumentation. Part C. Radiation Physics and Chemistry* **1991,** *37* (5), 657-665.

45. Duling, D. R., Simulation of multiple isotropic spin-trap EPR spectra. *Journal of Magnetic Resonance, Series B* **1994,** *104* (2), 105-110.

46. *http://tools.niehs.nih.gov/stdb/index.cfm*

47. Buettner, G. R., Spin trapping: ESR parameters of spin adducts 1474 1528V. *Free Radical Biology and Medicine* **1987,** *3* (4), 259-303.

48. Haber, F.; Weiss, J. In *The catalytic decomposition of hydrogen peroxide by iron salts*, Proceedings of the Royal Society of London A: Mathematical, Physical and Engineering Sciences, The Royal Society: **1934**, 332-351.

49. Ionita, P.; Gilbert, B.; Whitwood, A., Generation of oxygen-, sulfur, carbon-, nitrogen-and phosphorus-centred short-lived radicals via one-electron oxidation with stable hydrazyl radical. *Letters in Organic Chemistry* **2004,** *1* (1), 70-74.

50. Barker, P.; Beckwith, A. L.; Cherry, W. R.; Huie, R., Characterization of spin adducts obtained with hydrophobic nitrone spin traps. *Journal of the Chemical Society, Perkin Transactions 2* **1985,** (8), 1147-1150.

51. Sturgeon, B. E.; Chen, Y.-R.; Mason, R. P., Immobilized enzyme electron spin resonance: a method for detecting enzymatically generated transient radicals. *Analytical chemistry* **2003,** *75* (19), 5006-5011.

52. Sturgeon, B. E.; Glover, R. E.; Chen, Y.-R.; Burka, L. T.; Mason, R. P., Tyrosine iminoxyl radical formation from tyrosyl radical/nitric oxide and nitrosotyrosine. *Journal of Biological Chemistry* **2001,** *276* (49), 45516-45521.

53. Vassão, D. G.; Gang, D. R.; Koeduka, T.; Jackson, B.; Pichersky, E.; Davin, L. B.; Lewis, N. G., Chavicol formation in sweet basil (Ocimum basilicum): cleavage of an esterified C9 hydroxyl group with NAD (P) H-dependent reduction. *Organic & biomolecular chemistry* **2006,** *4* (14), 2733-2744.

54. Wertz, J., *Electron spin resonance: elementary theory and practical applications*. Springer Science & Business Media: **2012**.

55. Russell, W. R.; Burkitt, M. J.; Provan, G. J.; Chesson, A., Structure-specific functionality of plant cell wall hydroxycinnamates. *Journal of the Science of Food and Agriculture* **1999,** *79* (3), 408-410.

56. Russell, W. R.; Scobbie, L.; Chesson, A., Structural modification of phenylpropanoid-derived compounds and the effects on their participation in redox processes. *Bioorganic & medicinal chemistry* **2005,** *13* (7), 2537-2546.

57. (a) McLachlan, A., Hyperconjugation in the electron resonance spectra of free radicals. *Molecular Physics* **1958,** *1* (3), 233-240; (b) Heller, C.; McConnell, H. M., Radiation Damage in Organic Crystals. II. Electron Spin Resonance of (CO2H) CH2CH (CO2H) in β-Succinic Acid. *The Journal of Chemical Physics* **1960,** *32* (5), 1535-1539.

58. (a) Barry, B.; El-Deeb, M.; Sandusky, P.; Babcock, G., Tyrosine radicals in photosystem II and related model compounds. Characterization by isotopic labeling and EPR spectroscopy. *Journal of Biological Chemistry* **1990,** *265* (33), 20139-20143; (b) Vänngård, T., *Biophysical Chemistry of Dioxygen Reactions in Respiration and Photosynthesis: Proceedings of the Nobel Conference Held at Fiskebäckskil, Sweden, 1-4 July 1987*. Cambridge University Press: **1988**.

59. Dikanov, S. A.; Tyryshkin, A. M.; Bowman, M. K., Intensity of cross-peaks in HYSCORE spectra of S= 1/2, I= 1/2 spin systems. *Journal of Magnetic Resonance* **2000,** *144* (2), 228-242.

60. Chatterjee, R.; Milikisiyants, S.; Coates, C. S.; Lakshmi, K., High-resolution two-dimensional 1H and 14N hyperfine sublevel correlation spectroscopy of the primary quinone of photosystem II. *Biochemistry* **2010,** *50* (4), 491-501.

61. Höfer, P.; Grupp, A.; Nebenführ, H.; Mehring, M., Hyperfine sublevel correlation (HYSCORE) spectroscopy: A 2D ESR investigation of the squaric acid radical. *Chemical physics letters* **1986,** *132* (3), 279-282.

62. Dikanov, S. A.; Bowman, M. K., Cross-Peak Lineshape of Two-Dimensional ESEEM Spectra in Disordered S= 1 2, I= 1 2 Spin Systems. *Journal of Magnetic Resonance, Series A* **1995,** *116* (1), 125-128.

63. Nakazawa, S.; Ishii, A.; Minagawa, J.; Ono, T.-a., Application of 2D-HYSCORE spectroscopy to tyrosine radicals in photosystem II for evaluation of spin density distributions. *Chemical physics letters* **2005,** *405* (4), 318-322.

64. Liu, C.-J.; Miao, Y.-C.; Zhang, K.-W., Sequestration and transport of lignin monomeric precursors. *Molecules* **2011,** *16* (1), 710-727.

65. Cairns, J. R. K.; Esen, A., β-Glucosidases. *Cellular and Molecular Life Sciences* **2010,** *67* (20), 3389-3405.

66. Terashima, N.; Atalla, R.; Ralph, S.; Landucci, L. L.; Lapierre, C.; Monties, B., New preparations of lignin polymer models under conditions that approximate cell wall lignification. I. Synthesis of novel lignin polymer models and their structural characterization by 13 C NMR. *Holzforschung-International Journal of the Biology, Chemistry, Physics and Technology of Wood* **1995,** *49* (6), 521-527.

67. Ito, H.; Kamachi, T.; Yashima, E., Specific surface modification of the acetylene-linked glycolipid vesicle by click chemistry. *Chemical Communications* **2012,** *48* (45), 5650-5652.

68. Al-Ghanimi, H. A.; AL kaa'by, H. N., JOURNAL OF THE UNIVERSITY OF KARBALA. *Journal of Kerbala Universitv. Vol* **2011,** *9* (1).

69. Terashima, N.; Ralph, S. A.; Landucci, L. L., New facile syntheses of monolignol glucosides; p-glucocoumaryl alcohol, coniferin and syringin. *Holzforschung* **1996,** *50* (2), 151-155.